Titre: Title:	Étude expérimentale et modélisation de l'impact entre une bulle et une structure
Auteur: Author:	Étienne Pelletier
Date:	2014
Type:	Mémoire ou thèse / Dissertation or Thesis
Référence: Citation:	Pelletier, É. (2014). Étude expérimentale et modélisation de l'impact entre une bulle et une structure [Master's thesis, École Polytechnique de Montréal]. PolyPublie. https://publications.polymtl.ca/1595/

UNIVERSITÉ DE MONTRÉAL

ÉTUDE EXPÉRIMENTALE ET MODÉLISATION DE L'IMPACT ENTRE UNE BULLE ET UNE STRUCTURE

ÉTIENNE PELLETIER
DÉPARTEMENT DE GÉNIE MÉCANIQUE
ÉCOLE POLYTECHNIQUE DE MONTRÉAL

MÉMOIRE PRÉSENTÉ EN VUE DE L'OBTENTION
DU DIPLÔME DE MAÎTRISE ÈS SCIENCES APPLIQUÉES
(GÉNIE MÉCANIQUE)
OCTOBRE 2014

UNIVERSITÉ DE MONTRÉAL

ÉCOLE POLYTECHNIQUE DE MONTRÉAL

Ce mémoire intitulé :

ÉTUDE EXPÉRIMENTALE ET MODÉLISATION DE L'IMPACT ENTRE UNE BULLE ET UNE STRUCTURE

présenté par : PELLETIER Étienne
en vue de l'obtention du diplôme de : Maîtrise ès sciences appliquées
a été dûment accepté par le jury d'examen constitué de :

M. GARON André, Ph.D., président
M. ÉTIENNE Stéphane, Doct., membre et directeur de recherche
M. VIRGILIO Nick, Ph.D., membre

REMERCIEMENTS

Je veux premièrement remercier mon directeur de recherche, Stéphane Étienne, pour m'avoir donné l'opportunité de réaliser cette maîtrise. Sa disponibilité et son optimisme ont su me motiver à mener à bien cette recherche.

Également, je veux remercier mon mentor quotidien, Cédric Béguin. Voisin de bureau, il était toujours disponible pour répondre à mes questions, m'en poser davantage et voir plus loin que j'en étais capable.

Bien sûr, tous les membres de la chaire d'interaction fluide-structure avec qui nous avons eu plusieurs discussions fort intéressantes. Et plus particulièrement Constant, qui m'a accompagné de l'autre côté de la cloison pour ces deux dernières années. Toutes ces présences étaient des motivations supplémentaires pour se lever le matin et venir parler de bulle !

Finalement, ma copine Véronique. Celle qui m'a incité à revenir à l'école pour accomplir cette maîtrise. Celle qui m'a poussé à faire ce que je n'osais faire.

RÉSUMÉ

Les écoulements diphasiques sont présents dans plusieurs applications industrielles. Notamment, ils sont d'une grande importance dans les générateurs de vapeur des centrales nucléaires. À l'intérieur de ces générateurs, des écoulements à bulles traversent des faisceaux de tubes et engendrent des vibrations substantielles sur ces derniers. Dans le but de prévoir le spectre des forces agissant sur ces tubes, un modèle numérique a été développé au sein de la chaire de recherche industrielle en interaction fluide-structure CRSNG/BWC/EACL. Bien que le modèle soit prometteur, certains éléments pourraient être affinés.

Le but de ce mémoire est d'apporter par des méthodes expérimentales et théoriques des améliorations aux hypothèses à la base du modèle élaboré. Plus particulièrement, de développer des relations de fermeture pour la masse ajoutée de bulles dans un nuage de bulles. Également, de créer un modèle d'impact entre une bulle et une structure afin de connaître les efforts sur la bulle et sur la structure.

Dans un premier temps, le problème de masse ajoutée est traité. Sous l'hypothèse d'un écoulement potentiel, une méthode de résolution d'écoulement à l'intérieur d'un nuage de bulle est développée. Les bulles sont considérées comme des sphères rigides de taille identique avec des conditions de glissement imposées à leur surface. Une relation permettant de prédire la force de masse ajoutée sur une bulle au centre d'un nuage est développée. Elle prend en compte un effet individuel, un effet de confinement et un effet induit par les autres bulles. Il est ainsi possible, à partir de la géométrie d'un nuage de bulle, de déterminer quelle sera la force de masse ajoutée subie par n'importe quelle de ces bulles.

Ensuite, l'approche précédente est étendue pour le cas d'une bulle ellipsoïdale et déformable approchant d'un mur. Des relations de masse ajoutée sont développées tant pour le mode de translation que pour le mode de compression. La notion de force de jet est également discutée et son utilité pour la conservation de l'énergie est mise en évidence. Ces forces sont ensuite mises ensemble afin de créer un modèle d'impact sur un mur. Ce modèle peut non seulement servir à prédire les forces sur la bulle, mais également les forces sur le mur.

Afin de valider ce modèle, plusieurs expériences ont été réalisées. Le premier montage permet de réaliser des impacts de bulles sur une mur fixe. De ces expériences, des relations de restitutions sont extraites. Elles permettent de prédire l'état de la bulle après collision à partir de ses caractéristiques initiales. Il devient évident que la catégorie de bulle (lente ou rapide) a un effet significatif sur la dynamique de la collision. Plus encore, l'élément clé qui dicte le comportement au rebond semble être le rapport d'aspect de la bulle.

Un deuxième montage expérimental permet de réaliser des impacts de bulles millimé-

triques sur une structure flottante. Les résultats expérimentaux révèlent que la structure flottante subie une force répulsive en provenance des bulles. Cette force est observée à partir d'une distance bulle-mur d'environ 5 rayons de bulle. Bien que l'analyse effectuée ne soit que partielle, le modèle prédit une force à distance qui est du bon ordre de grandeur. Les forces en jeux sont de l'ordre du microNewton.

Finalement, différents mécanismes à la base de la fragmentation d'une bulle sont observés. Contrairement à nos attentes, les éclatements ne sont pas causés par un contact avec une structure, mais davantage par des déchirements. Ces déchirements sont causés par des vortex stationnaires et des zones d'accélération subite dans l'écoulement.

Bien que les sujets explorés soient tous différents, ils ont tous leur part d'importance. Non seulement apportent-ils des connaissances générales sur le comportement des bulles, mais également des pistes à suivre pour le développement de modèles numériques représentant des écoulements à bulles.

ABSTRACT

Two-phase flows are present in many industrial applications. In particular, they are of interest in the steam generators of nuclear power plants. In these equipment, bubbly flows go through tube bundles and produce substantial vibration on the constitutive tubes. In order to model the force spectrum acting on the tubes, a numerical model was developed by the Industrial Research Chair in fluid-structure interaction NSERC/BWC/AECL. Although promising, some elements of the model could be refined.

The purpose of this paper is to provide theoretical and experimental methods to improve the developed code. In particular, to develop added mass closure relations for bubbles in a cloud of bubbles. Also, to create a bubble-structure collision model. This model should allow the prediction of the forces acting on the bubble as well as the forces acting on the structure.

To begin, the problem of added mass is treated. Under the potential flow theory, a method for solving the flow inside a cloud of bubbles is developed. The bubbles are considered as rigid spheres of the same size with a slip condition prescribed on their surface. From these flows, an expression to predict the added mass force on any given bubble is developed. It takes into account an individual effect, a confinement effect and an induced effect caused by other bubble accelerations. It is therefore possible, from a known geometry of bubbles, to determine what will be the added mass force exerted on any of these bubbles.

Then, the above approach is extended to the case of an ellipsoidal and deformable bubble approaching a wall. Added mass relations are developed for both the translation mode for the compression modes. The concept of jet force is also discussed and its usefulness for energy conservation is highlighted. These forces are then put together to create an impact model on a wall. This model is used to predict the forces on the bubble and on the wall.

To validate this model, several experiments were conducted. The first one is the impact of rising bubbles with a rigid horizontal wall. Restitution relations are extracted from the experimental results. These relations allow to predict the state of a bubble after impact from the characteristics before impact. It becomes clear that the category of bubble (slow or fast) has a significant effect on the collision behavior. Moreover, the key element that drives the rebound behavior seems to be the aspect ratio of the bubble.

As a second experimental part, the impact of rising bubbles on a floating structure was performed. Experiments shows that the floating structure experiences a repulsive from the bubble. This force is becomes significant for bubble-wall distances of approximately 5 bubble radius. Although the analysis is preliminar, the model predicts the right order of magnitude for this repulsive force. These forces are of the order of micronewton.

Finally, bubble fragmentation was observed. Contrary to our expectations, the fragmentations were not caused by contact with a structure, but by tearing. Tearing were observed in a stationary vortex and in an area of sudden acceleration in the flow.

Although the topics explored are all different, they all have their share of importance. Not only do they provide a general understanding of the behavior of bubbles, they also suggests avenues for the development of numerical model representing bubbly flows.

TABLE DES MATIÈRES

LISTE DES TABLEAUX

LISTE DES FIGURES

LISTE DES SIGLES ET ABRÉVIATIONS

a	Petit axe d'une bulle éllipsoïdale
A_b	Aire de la section transversale d'une bulle sphérique de rayon r_b
C_M	Coefficient de masse ajoutée
C_D	Coefficient de trainée
C_J	Coefficient de la force de jet
C_{PD}	Coefficient de la force de pression dynamique
ε	Taux de vide
g	Accélération gravitationnelle
ρ_ℓ	Densité de la phase liquide
ρ_g	Densité de la phase gazeuse
μ	Viscosité de la phase liquide
σ	Tension de surface
r_b	Rayon équivalent d'une bulle
Re	Nombre de reynolds
V_b	Volume d'une bulle
We	Nombre de Weber
χ	Rapport d'aspect d'une bulle

CHAPITRE 1

INTRODUCTION

Les générateurs de vapeur sont des composants essentiels au fonctionnement des centrales nucléaires. À l'intérieur de ces générateurs, un important débit d'eau circule au travers d'un faisceau de tubes caloporteurs. Durant le contact, la température de l'eau augmente jusqu'au point où la phase vapeur commence à être générée. Le fluide diphasique ainsi créé interagit avec le faisceau en retour et induit des vibrations substantielles aux tubes. Afin de limiter l'amplitude de déplacement des tubes, des supports antivibrations (AVB) sont insérés au travers du faisceau. La figure 1.1 illustre un générateur de vapeur, les faisceaux de tubes ainsi que les AVB.

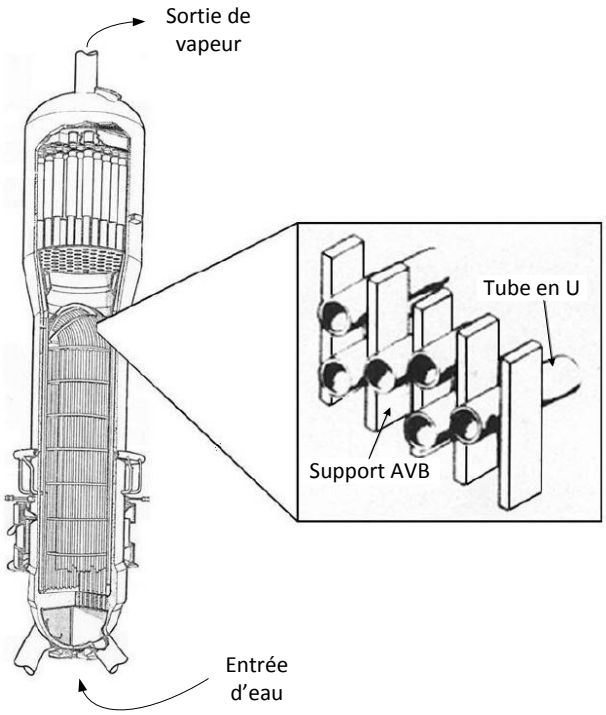

Figure 1.1 Illustration d'un générateur de vapeur

Bien que les supports soient efficaces pour le contrôle des vibrations, les points de contact entre les tubes et les AVB sont sujets à une détérioration prématurée due au frottement. Cette usure diminue significativement la durée de vie des générateurs de vapeur et entraîne des coûts majeurs pour la réparation et la restauration de ces composants.

Afin de pouvoir prévoir ces défaillances, les forces agissants sur des faisceaux de tubes ont été étudiées. Pour des faisceaux soumis à des écoulements transverses, on peut nommer différents mécanismes d'excitation des tubes :

- La turbulence ;
- Le détachement tourbillonnaire (vortex shedding) ;
- Les instabilités fluide-élastiques ;
- Les forces quasi-périodiques (pseudo-turbulence) ;
- La résonance acoustique ;

Si l'écoulement est monophasique liquide, les trois premiers mécanismes d'excitation peuvent être observés. Les contributions de chacun de ces mécanismes sont indiquées sur la figure 1.2 (Gorman, 1976). La figure 1.2 présente l'amplitude de vibration d'un tube dans un faisceau en fonction de la vitesse interstitielle de l'écoulement. La turbulence crée une augmentation de l'amplitude de vibration qui est proportionnelle à la vitesse du fluide. Un premier pic dans l'amplitude de vibration apparaît lorsque la fréquence des détachements tourbillonnaires s'approche de la fréquence naturelle des tubes. Puis, à partir d'une certaine vitesse critique, l'instabilité fluide-élastique se développe. La vibration devient alors hors de contrôle.

Toutefois, lorsque l'écoulement devient diphasique, il y a une modification dans les modes d'excitation. Bien que l'instabilité fluide-élastique persiste, les lâchés tourbillonnaires disparaissent et la nature des forces turbulentes change. Lance et Bataille (1991) ont démontré qu'à partir de faibles taux de vide ($\varepsilon > 1\%$), la turbulence classique causée par le cisaillement cède place à une pseudo-turbulence créée par le déplacement des bulles.

Les effets de la pseudo-turbulence sur un faisceau de tubes ont été étudiés par plusieurs anciens étudiants de la chaire de recherche industrielle d'interaction fluide structure BWC/EACL/CRSNG (Zhang, 2007; Senez, 2010; Perrot, 2011). Il a été montré que cette pseudo-turbulence génère des forces quasi-périodiques. Ces forces quasi-périodiques sont caractérisées par une distribution fréquentielle relativement bien définie avec un maximum spectral augmentant avec de la vitesse du fluide (Up) tant en amplitude qu'en fréquence (Fig. 1.3). L'hypothèse actuellement acceptée au sein du groupe de recherche est que cette force quasi-périodique est causée par l'impact régulier d'amas de bulles sur les tubes. Dans cette optique, Senez et Étienne (2011) ont développé un modèle numérique ayant pour but de recréer ces spectres de force sous l'hypothèse d'un écoulement à bulle.

La figure 1.4 illustre l'essence du modèle. Il s'agit d'une vue en coupe d'un faisceau de tubes soumis à un écoulement a bulle. Les portions grises correspondent aux tubes et les cercles blancs correspondent à des bulles. Les bulles sont traitées comme des sphères rigides

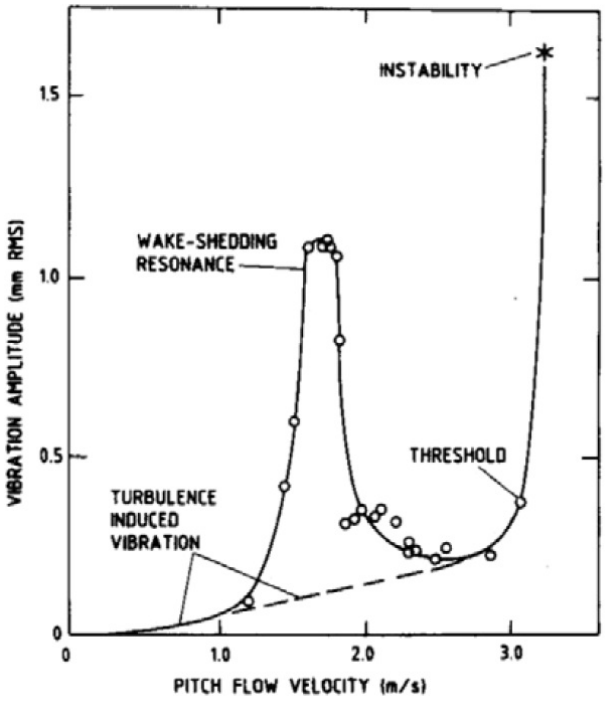

Figure 1.2 Réponse vibratoire d'un tube à l'intérieur d'un faisceau soumis à un écoulement transverse monophasique (Gorman, 1976).

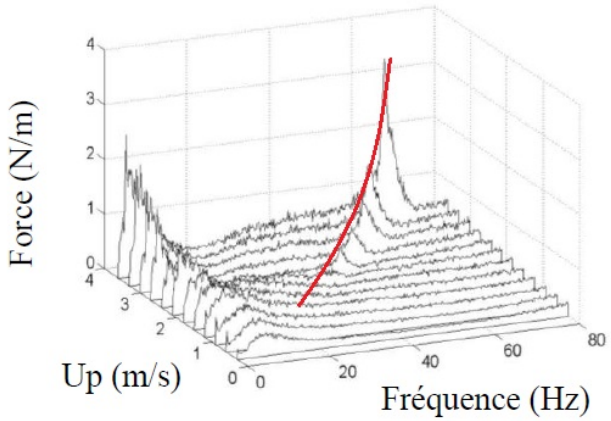

Figure 1.3 Spectre du couple agissant en traînée sur un tube compris dans un faisceau. (ε = 50%). Le trait rouge indique la force quasi-periodique (Perrot (2011))

subissant l'écoulement de la phase liquide (en bleu). Chacune est traitée individuellement dans un formalisme Lagragien. Les forces appliquées sur une bulle sont la poussée d'Archimède ainsi qu'une traînée induite par l'écoulement local de la phase liquide autour de la bulle.

Durant l'évolution de ce système, les bulles peuvent rencontrer deux situations de contact : bulle-bulle et bulle-tube. Il pourra alors y avoir trois comportements : coalescence des bulles

(bulle-bulle), éclatement (bulle-tube) ou rebond élastique (bulle-bulle / bulle-tube). Entre ces évènements, les bulles évoluent indépendamment les unes des autres jusqu'à ce qu'un nouveau contact soit détecté. De plus, l'écoulement est considéré indépendant de la distribution des bulles. Il s'agit donc d'un couplage unidirectionnel de l'écoulement sur les bulles.

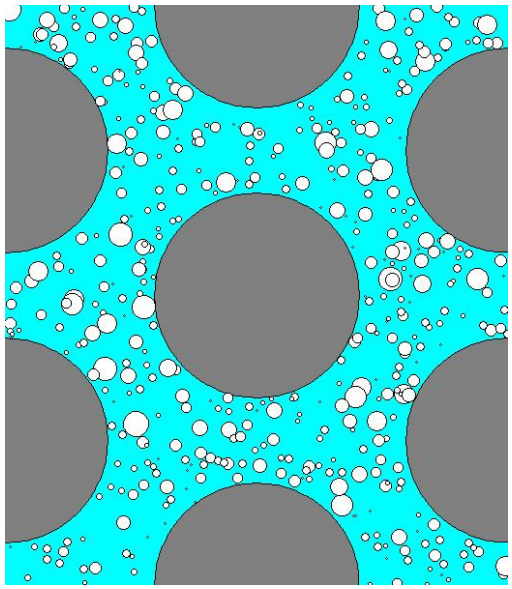

Figure 1.4 Illustration du modèle développé par Senez et Étienne (2011)

Bien que ce modèle a réussi à recréer une certaine périodicité dans les forces, son accord avec les spectres expérimentaux laisse place à amélioration.

1.1 Objectifs de recherche

Les objectifs de la recherche sont d'apporter des améliorations aux hypothèses utilisées dans le modèle présenté par Senez et Étienne (2011) par des méthodes théoriques et expérimentales. Plus spécifiquement :

- Développer les expressions de force de masse ajoutée pour des bulles seules, à proximité d'une structure et dans un nuage de bulles ;
- Développer un modèle d'impact entre une bulle et une structure afin de
  - Prédire le comportement d'une bulle lors d'une collision avec un mur ;
  - Prédire les forces transmises aux murs durant l'impact.

Notez que les impacts traités dans ce document ont lieu entre une bulle est un mur plan. Il n'y aura pas de traitement explicite des collisions bulle-tube. On considère, en première approximation, que le tube se comportera comme un mur plan dû aux différences de rayons

entre la bulle et le tube ($r_{bulle} << r_{tube}$).

1.2 Plan du mémoire

Le corps de ce mémoire est divisé en quatre chapitres. Le premier traite des forces de masse ajoutée agissant sur des bulles sphériques et rigides pour différentes configurations géométriques. Les deux chapitres suivants traitent de collisions bulle-structure au point de vue expérimental et théorique respectivement. Pour ces deux sections, l'hypothèse sphérique de la bulle est délaissée pour faire place à des bulles partiellement déformables. Finalement, le dernier chapitre traite de sujets connexes qui ont été étudiés dans le cadre de cette maîtrise, mais qui n'ont pas été présentés dans les trois premiers chapitres soit : les forces à distance, l'éclatement des bulles et une note concernant la conservation de l'énergie dans les systèmes comportant un corps à masse variable.

Les trois premiers chapitres sont composés d'articles soumis pour publication dans des journaux. Le dernier chapitre ajoute à ce qui n'a pas été inclus dans ces articles. Ces quatre chapitres de développement sont précédés d'une revue de littérature et suivis d'une conclusion.

CHAPITRE 2

REVUE DE LITTÉRATURE

Cette revue de littérature se divise en trois parties. La première décrit de manière générale le comportement des bulles dans un milieu infini et stagnant. La deuxième discute des forces de masse ajoutée et de traînée sur une bulle dans différentes situations. La troisième traite du cas particulier où une bulle entre en collision avec un mur.

2.1 Comportement d'une bulle

Une bulle est constituée par un fluide interne séparé d'un fluide externe par une interface de forme variable. Les vitesses tangentielles des fluides de part et d'autre de l'interface sont égales afin de respecter la continuité des vitesses. Si la viscosité du fluide interne tend vers l'infini, la vitesse interne du fluide sera nulle. La vitesse tangentielle sur la surface sera donc nulle et il y aura **adhérence** du fluide externe. Ceci est l'équivalent d'un corps solide. À l'opposé, pour une viscosité nulle du fluide interne, il n'y aura aucune contrainte sur la vitesse tangentielle à l'interface. On dit alors qu'il y a **glissement** à l'interface. Cette hypothèse de glissement est considérée comme respectée pour une bulle d'air dans de l'eau pure, car l'air est beaucoup moins visqueux que l'eau.

Toutefois si l'eau contient des contaminants, lorsqu'une bulle d'air s'y déplace, des surfactants sont réputés venir se coller à l'interface. Sur ces surfactants, la condition de glissement n'est pas respectée et ils sont poussés vers l'arrière de la bulle. Ce faisant, la condition à l'interface de la bulle est en glissement vers l'avant où l'interface est *propre* et en adhérence à l'arrière où elle est *contaminée* (Tomiyama *et al.*, 2002). La proportion glissement-adhérence est variable selon la quantité de surfactant. Dès lors, il est difficile d'établir une règle universelle pour prédire la condition frontière de l'écoulement à la surface de la bulle.

Certains auteurs ont choisi des conditions de glissement (Moore, 1965; Kushch *et al.*, 2002; Van Wijngaarden, 1976; Kok, 1993) tandis que d'autres ont préféré la condition d'adhérence (Canot *et al.*, 2003; Podvin *et al.*, 2008). Cette différence de mobilité à la surface à longtemps été prise pour cause de la disparité dans les vitesses terminales observées expérimentalement. Les travaux de Wu et Gharib (2002) et plus récement de Peters et Els (2012) ont permis de démontrer que cette interprétation était fausse. La dispersion dans ces valeurs provient des différents modes stables de translation des bulles. Dans les faits, deux modes sont observés. Les bulles du premier mode présentent des formes plutôt aplaties et possèdent des vitesses

d'ascension rapides. À l'opposé, les bulles du deuxième mode ont des formes plus sphériques et des vitesses d'ascension plus faibles. Ces bulles sont donc nommées respectivement des bulles rapides et des bulles lentes (Peters et Els, 2012). La figure 2.2 illustre les résultats de Wu et Gharib (2002) à cet effet. χ représente le rapport d'aspect, i.e. le rapport entre le grand et le petit axe de la bulle.

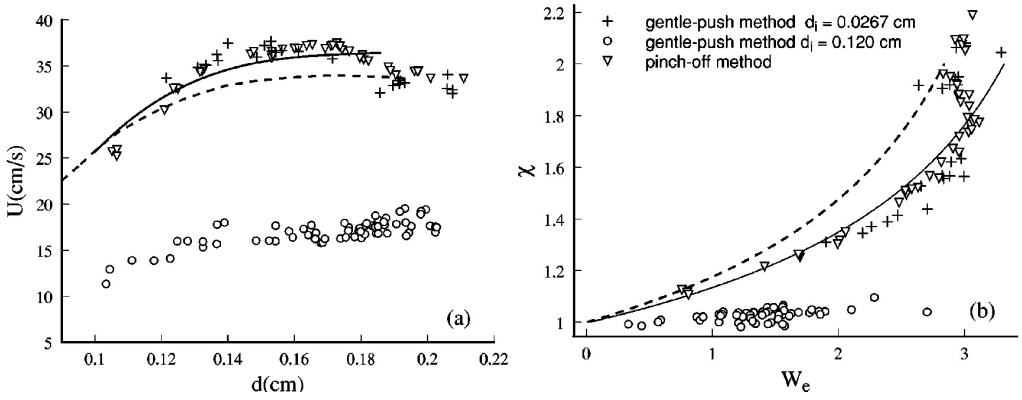

(a) Vitesse terminale (b) Rapport d'aspect

Figure 2.1 Données obtenues par Wu et Gharib (2002) pour dans bulles dans de l'eau purifié. (▽) et (+) sont des bulles rapides. (∘) sont des bulles lentes.

Il faut noter que ces bulles ont été créées dans le même liquide et donc dans les même concentrations de surfactant. Leur conclusion est que la déformation initiale des bulles conduit aux deux comportements observés. Cette conclusion est en accord avec celle de Tomiyama *et al.* (2002) et Peters et Els (2012). Une forte perturbation initiale mène à des bulles rapides et l'inverse mène à la génération de bulles lentes.

Bien que la différenciation entre les bulles rapides et lentes a été faite au point de vue expérimental, il n'y a toujours pas de cadre théorique pour décrire les deux comportements (Peters et Els, 2012). En fait, seul le comportement des bulles rapides semblent pouvoir être expliqué théoriquement (Wu et Gharib, 2002).

L'unique dérivation analytique de la forme des bulles provient de Moore (1965). Sa première approche était d'équilibrer la force créée par la pression dynamique avec la force de tension de surface pour une bulle sphérique. La force liée à la pression est obtenue en intégrant la pression dynamique ($P_{dynamique}$) sur la surface d'une bulle sphérique.

$$P_{dynamique} = -\frac{1}{2}\rho \mathbf{u}^2 \tag{2.1}$$

La force de tension de surface est associée à l'énergie emmagasinée dans la déformation de la bulle. En effet, lorsque la bulle est sphérique, l'énergie de surface est minimale. Dès que

la bulle change de forme, l'aire de l'interface (S) augmente et l'énergie de déformation (E_σ) augmente proportionnellement. Mathématiquement, $E_\sigma = \sigma S$. Puisqu'il s'agit d'une énergie potentielle, une force conservatrice y est associée. Dans l'approche de Moore, cette force sera projetée sur la coordonée χ et sera calculée comme

$$F_\sigma^\chi = -\frac{\partial}{\partial \chi} E_\sigma(\chi) \tag{2.2}$$

En équilibrant ces deux forces, Moore obtient une première expression liant χ au nombre de Weber ($We = 2r_b\rho_\ell v_b^2/\sigma$). Cette relation est valide pour $\chi \approx 1$.

$$\chi = 1 + \frac{9}{64} We \tag{2.3}$$

Il étend ensuite cette relation à des bulles de plus grands rapports d'aspect. Il exige encore l'équilibre de la pression dynamique à la tension de surface, mais cette fois sur une bulle ellipsoïdale. L'exigence n'est toutefois imposée qu'aux points de stagnation et à l'équateur. La relation obtenue est

$$We = 4\chi^{4/3}(\chi^3 + \chi - 2)[\chi^2 sec^{-1}\chi - (\chi^2 - 1)^{1/2}]^2(\chi^2 - 1)^3 \tag{2.4}$$

Cette relation surestime légèrement l'aplatissement des bulles lorsqu'elle est comparée à des χ expérimentaux. Elle est tracée en trait tireté sur la figure 2.2(b). Afin de rendre compte des observations exprérimentales, Legendre *et al.* (2012) proposent la relation empirique

$$\chi = \frac{1}{1 - \frac{9}{64} We} \tag{2.5}$$

qui décrit le comportement des bulles rapides. Aucune relation de ce type n'est présente dans la littérature pour les bulles lentes.

Comme dernier point de description du mouvement des bulles : leur trajectoire. Il a été montré que les bulles rapides peuvent se déplacer selon trois types de trajectoires : rectilinéaire, zig-zag et hélicoïdale. Ellingsen et Risso (2001) ont montré que ces trois trajectoires se succèdent dans l'ordre. À partir d'un mode rectilinéaire, le mode zig-zag se développe. Ce mode se caractérise par une oscillation spatiale comprise dans un seul plan. Une fois l'amplitude de ce mode saturée, le mode hélocoïdal apparaît. Ce mode se caractérise par un mouvement circulaire dans le plan perpendiculaire à la gravité.

Il faut noter que si des perturbations significatives sont apportées au système, une bulle peut se retrouver dans le mode hélicoïdal sans passer par les autres modes. Pour les bulles lentes, seul le mode zig-zag a été observé (Tomiyama *et al.*, 2002).

2.2 Force sur la bulle

Outre les forces qui mènent aux oscillations dans la trajectoire des bulles et la force d'Archimède, on note deux autres types de force : masse ajoutée (F_M) et traînée (F_D). La force de masse ajoutée est une force proportionnelle à l'accélération d'une bulle et de sens inverse. Il s'agit d'une force résultant de l'accélération du fluide autour de la bulle engendrée par l'accélération de la bulle. Cette force peut s'interpréter comme l'inertie ajoutée par l'accélération du fluide environnant la bulle. La force de traînée est quant à elle dépendante de la vitesse et agit dans la direction inverse. Elle a une composante de pression et de viscosité.

(a) Trainée. (b) Masse ajoutée.

Figure 2.2 Illustration des forces de traînée et de masse ajoutée.

Pour de grandes valeurs du nombre de Reynolds ($Re = 2r_b v_b \rho_\ell / \mu$), la composante de pression est dominante. Au contraire, pour de faibles valeurs, la composante visqueuse est plus imporante. Cependant la force visqueuse influence le détachement de la couche limite et par la meme occasion la traînée de pression

2.2.1 Masse ajoutée

La force de masse ajoutée agissant selon z sur une bulle de volume V_b se définit mathématiquement comme :

$$F_{M_z} = -\rho_\ell V_b C_M \ddot{z} \tag{2.6}$$

où C_M est le coefficient de masse ajoutée

Mouvement dans un milieu infini

Le cas le plus simple qui peut être étudié est la translation d'une bulle sphérique et rigide dans un fluide infini et stagnant. Dans ce cas, sous l'hypothèse d'un écoulement potentiel, Milne-Thomson (1968) a montré par un raisonnement énergétique que

$$C_M = 0.5 \tag{2.7}$$

La forme sphérique d'une bulle est respectée pour des faibles nombres de Weber (Legendre

et al., 2005) mais une forme ellipsoïdale est plus appropriée pour décrire des bulles d'air millimétriques dans de l'eau (Clift et Weber, 1978). Lamb (1932) a également utilisé une approche à écoulement potentiel pour démontrer que le coefficient de masse ajoutée d'une telle bulle en translation s'exprime comme

$$C_M = \frac{\alpha}{2-\alpha} \quad \text{où} \quad \alpha = \frac{2\chi^2}{\chi^2-1}\left[1-(\chi^2-1)^{-1}\text{acos}(\chi^{-1})\right] \tag{2.8}$$

avec χ est le rapport entre le grand (b) et le petit axe (a) de la bulle (voir fig. 2.3) . Une linéarisation de cette relation est donnée par Klaseboer *et al.* (2001) (Eq. 2.9).

$$C_M = 0.62\chi - 0.12 \tag{2.9}$$

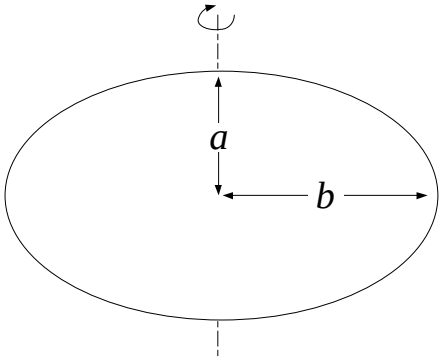

Figure 2.3 Hypothèse de forme ellipsoïdale de la bulle

Kushch *et al.* (2002), par une technique similaire à Milne-Thomson (1968), ont obtenu la force de masse ajoutée s'exerçant sur le degré de liberté de compression de la bulle. Dans leur approche, le volume de la bulle est considéré constant et la forme de la bulle est un ellipsoïde de révolution (fig. 2.3). La compression correspond alors à une diminution de a et une augmentation de b conservant le volume. En exprimant ce mouvement en fonction du petit axe a, on obtient pour le coefficient de masse ajouté :

$$C_M = 0.2\chi^{1.17} \tag{2.10}$$

Mouvement à proximité d'un mur

Les équations précédentes sont valables dans un milieu infini, mais lorsqu'une bulle s'approche d'un mur, un effet de confinement apparaît. Ce confinement augmente le coefficient de masse ajoutée. La correction equivalente peut être exprimée sous la forme d'une série.

Milne-Thomson (1968) avait obtenu le premier terme de cette série. Une approche plus générale par Kok (1993) permet de calculer les termes de la série par des relations de récurrence. Les premiers termes sont :

$$C_M(h) = 0.5\left(1 + \frac{3}{8}\left(\frac{r_b}{h}\right)^3 + \frac{3}{64}\left(\frac{r_b}{h}\right)^6 + \frac{9}{256}\left(\frac{r_b}{h}\right)^8 + \frac{3}{512}\left(\frac{r_b}{h}\right)^9 + ...\right) \tag{2.11}$$

où h représente la distance entre le centre de la bulle. Aucune relation équivalente n'a été trouvée dans la littérature pour une bulle ellipsoïdale s'approchant d'un mur où oscillant près d'un mur.

Mouvement dans un nuage de bulles

Dans la situation où une bulle est entourée de bulles, plusieurs facteurs viennent en compte dans le calcul de la masse ajoutée. Le principal est la distribution géométrique du nuage de bulles. Toutefois, il est bien plus simple de parler de taux de vide que de configuration d'un nuage de bulles. Le taux de vide correspond au rapport volumique du gaz sur le liquide. Relativement à ce taux de vide, différents auteurs ont calculé des relations de masse ajoutée distinctes (Tableau 2.1). Ces relations sont majoritairement des approximations au premier ordre.

Tableau 2.1 Relation de masse ajoutée en fonction du taux de vide

Van Wijngaarden (1976)	$C_M(\varepsilon) \approx \frac{1}{2} + \frac{2.78}{2}\varepsilon$
Niemann et Laurien (1991)	$C_M(\varepsilon) \approx \frac{1}{2} + \frac{3.26}{2}\varepsilon + \frac{7.7}{2}\varepsilon^2$
Biesheuvel et Spoelstra (1989)	$C_M(\varepsilon) \approx \frac{1}{2} + \frac{3.32}{2}\varepsilon$
Mokeyev (1977)	$C_M(\varepsilon) \approx \frac{1}{2} + \frac{4.2}{2}\varepsilon$
Zuber et Hench (1962)	$C_M(\varepsilon) \approx \frac{1}{2} + \frac{3}{2}\varepsilon$
Wallis (1989)	$C_M(\varepsilon, \lambda) = \frac{1}{2}\frac{(2-2\varepsilon)+\lambda(1+2\varepsilon)}{(2+\varepsilon)+\lambda(1-\varepsilon)}$

Malgré que les 5 premiers auteurs ont tous une approche différente, leurs résultats sont similaires avec une dépendance positive en ε. La seule relation nettement différente provient de Wallis (1989). Avec son paramètre λ vallant 0 à $+\infty$, sa relation peut avoir une dépendance soit positive soit négative en ε. Le paramètre λ est lié à l'impédance du milieu et ne peut être explicitement associé à une configuration géométrique d'un nuage de bulles.

2.2.2 Traînée

Le second type de force est la force de traînée. Elle est proportionnelle au carré de la vitesse et s'exprime traditionnellement par l'entremise du coefficient de traînée C_D.

$$F_D = -\frac{1}{2}\rho_\ell A_b C_D v_b^2 \tag{2.12}$$

Milieu infini

Plusieurs relations pour déterminer ce coefficient existent dans la littérature. Les principales sont identifiées dans le tableau 2.2 avec une brève description. Stokes/Potentiel fait référence au type d'écoulement considéré. Glissement/Adhérence fait référence à la condition limite sur l'interface bulle-liquide. χ indique l'hypothèse d'une bulle ellipsoïdale. La dernière relation a été calculé à partir d'un écoulement potentiel partout sauf à proximité de la bulle où un écoulement à couche limite à été considéré.

Les deux premières relations du tableau sont des cas particuliers du développement théorique de Taylor et Acrivos (1964). En effet, Φ_μ représente le rapport des viscosités entre les fluides interne et externe à la bulle. On retrouve la condition de glissement pour $\Phi_\mu \to 0$ et la condition d'adhérence pour $\Phi_\mu \to \infty$. Dans le cas d'une bulle d'air dans de l'eau, $\Phi_\mu \approx 0.02$. On considère toutefois que les écoulements de stokes sont valables pour Re<1.

Tableau 2.2 Relations de traînée

Clift et Weber (1978)	$C_D = \frac{24}{Re}$	Stokes Adhérence
Michaelides (2006)	$C_D = \frac{16}{Re}$	Stokes Glissement
Taylor et Acrivos (1964)	$C_D = \frac{24}{Re}\left(\frac{2+3\Phi_\mu}{3+3\Phi_\mu}\right)[1 + \mathrm{O}(Re)]$	Stokes
Batchelor (2010)	$C_D = \frac{48}{Re}$	Potentiel Glissement
Moore (1959)	$C_D = \frac{48}{Re}G(\chi)$	Potentiel Glissement χ
Moore (1965)	$C_D = \frac{48}{Re}G(\chi)(1 + \frac{H(\chi)}{\sqrt{Re}} + ...)$	Potentiel Glissement χ Couche limite

Les relations $G(\chi)$ et $H(\chi)$ sont données par :

$$G(\chi) = \frac{\chi^{4/3}}{3}(\chi^2-1)^{3/2}\frac{[(\chi^2-1)^{1/2}-(2-\chi^2)\sec^{-1}(\chi)]}{[\chi^2\sec^{-1}(\chi)-(\chi^2-1)^{1/2}]^2} \tag{2.13}$$

$$H(\chi) = 0.0195\chi^4 - 0.2134\chi^3 + 1.7026\chi^2 - 2.1461\chi - 1.5732 \tag{2.14}$$

De plus, un coefficient de traînée pour un mouvement de compression peut également être défini. Kushch *et al.* (2002) ont utilisé un écoulement potentiel et la technique de dissipation visqueuse (Batchelor, 2010) pour obtenir la relation 2.15.

$$C_D = \frac{128}{3}\frac{1}{Re_a}\chi^{1.25} \tag{2.15}$$

avec $Re_a = 2r_b\rho_\ell\dot{a}/\mu$.

Proximité d'un mur

Lorsqu'une bulle approche d'un mur, le confinement génère une augmentation de la traînée. Sous l'hypothèse d'un écoulement potentiel, Kok (1993) a décrit sous la forme d'une série cette correction. Les premiers termes de la série sont :

$$C_D(h) = \frac{48}{Re}\left(1+\left(\frac{r_b}{2h}\right)^3+\frac{3}{4}\left(\frac{r_b}{2h}\right)^6+\frac{11}{3}\left(\frac{r_b}{2h}\right)^8+\frac{1}{2}\left(\frac{r_b}{2h}\right)^9+\frac{39}{4}\left(\frac{r_b}{2h}\right)^{10}+...\right) \tag{2.16}$$

Aucune relation n'est présente dans la littérature pour la trainée d'une bulle ellipsoïdale en translation ou en compression à proximité d'un mur.

2.3 Impact sur un mur

Pour traiter de l'impact d'une bulle sur un mur, différentes approches ont été utilisées dans la littérature. La plus simple a été développée par Legendre *et al.* (2005). Ils considèrent une goutte liquide dans un milieu liquide comme un oscillateur harmonique amorti. À partir de cette hypothèse, ils extraient une dépendance fonctionnelle du coefficient de restitution. Leur travail a été adapté pour des bulles d'air par Zenit et Legendre (2009). Cette approche est toutefois limitée par son impossibilité à prédire ce qui se passe avant et apres l'impact. Elle ne décrit que le moment où il y a contact entre la bulle et le mur. Toute la dynamique d'impact est résumée en un coefficient de restitution. De plus, elle ne permet pas de déterminer les forces sur le mur.

Un modèle plus complet a été développé par Klaseboer *et al.* (2001). Dans leur modèle, la bulle est considérée comme complètement déformable et tout le mouvement hors contact est pris en compte. Le drainage du film entre la bulle et le mur est résolu. Ainsi, en couplant l'écoulement dans le film avec la déformation de la bulle et la position du centre de masse, le système est complet. Cette approche a été étendue à un mur incliné par Moraga et R.T. Lahey (2005) et Podvin *et al.* (2008). Les prédictions du modèle sont comparables à l'expérience. Toutefois, au-delà d'une inclinaison de 60°, le modèle n'est plus valide. Il faut aussi noter qu'à chaque itération temporelle du modèle s'accompagne d'une résolution spatiale de l'écoulement, de la forme de l'interface et du mouvement de la bulle. Ce dernier aspect en fait une approche coûteuse en calcul.

Finalement, certains autres auteurs ont résolu l'écoulement complet autour de la bulle. Canot *et al.* (2003) a résolu l'écoulement en 2 dimensions autour d'une bulle complètement déformable via une simulation par éléments frontières (BEM). L'écoulement est considéré comme irrotationnel et la condition d'adhérence à la surface a été choisie. Kushch *et al.* (2002) ont quant à eux résolu l'écoulement irrotationnel autour de bulle ellipsoïdale et compressible avec une condition de glissement aux interfaces. La force du mur est intégrée via la théorie de la lubrification dans le film entre la bulle et le mur.

CHAPITRE 3

ARTICLE 1 : VOID FRACTION INFLUENCE ON ADDED MASS IN A BUBBLY FLOW

En première approximation, une bulle peut être considérée comme une sphère rigide avec des conditions de glissement imposées sur sa surface. Basé sur cet hypothèse et sur la théorie des écoulements potentiels, l'article suivant développe un formalisme pour déterminer la force de masse ajoutée agissant sur une bulle.

Soumis pour publication dans : *European Journal of Mechanics - B/Fluids*

C. BÉGUIN, É. PELLETIER & S. ÉTIENNE
BWC/AECL/NSERC Chair of Fluid-Structure Interaction
Department of Mechanical Engineering, École Polytechnique,
P.O.Box 6079, succ. Centre-Ville, Montréal (Québec), Canada, H3C 3A7
* cedric.beguin@polymtl.ca

Abstract

This paper proposes a relation for the added mass coefficient of spherical bubbles depending on void fraction based on results obtained by a semi-analytical method.

This information is essential to completely characterize finely dispersed bubbly flows, where small spherical gas bubbles are present in a continuous liquid phase. Most of the closure relations for Euler-Euler or Euler-Lagrange models are obtained from experiments involving single bubbles. Their applicability to systems with high void fraction is therefore questionable.

This paper uses solid harmonics to solve 3D potential flow around bubbles. Several configurations were calculated for different numbers of particles and spatial configurations. Our results are compared with previous studies. Depending on the model proposed by previous authors, added mass forces could increase or decrease with void fraction. This paper solves these discrepancies by underlining the effect of induced added mass.

The main purpose of this work is to develop simple formulas fitting our semi-analytical results. These simple formulas are suitable for further use, particularly as added mass models for multiphase flow averaged equations.

Nomenclature

Variables :		**Subscripts :**(see Figure below)
a :	bubble radius (m)	r, θ, φ : Spherical coordinates
$\mathbf{F}$:	force (N)	x, y, z : Cartesian coordinates
P :	fluid pressure (Pa)	**Dimensionless numbers :**
$\mathbf{U}$:	velocity (m/s)	ε : Void fraction
ρ :	mass density (kg/m^3)	C_M : Added mass coefficient

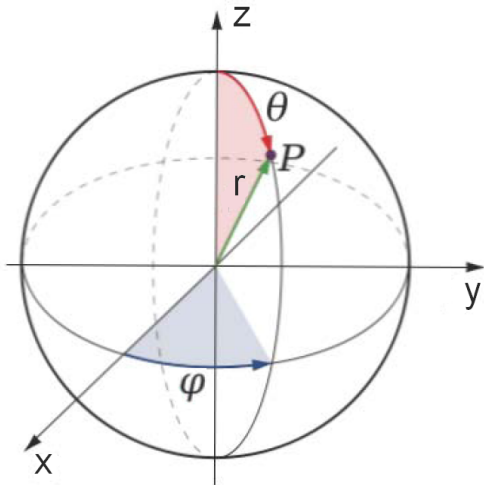

Spherical coordinates are :
r, the radial distance
$\theta \in [0\ \pi]$, the polar angle
$\varphi \in [0\ 2\pi]$, the azimuthal angle.

Cartesian coordinates are :
$x = r\cos\varphi\sin\theta$,
$y = r\sin\varphi\sin\theta$ and
$z = r\cos\theta$

Other symbols are defined in the text.

3.1 Introduction

We are concerned with the motion of a body surrounded by a fluid. The fluid mass displaced by the body increases its inertia which defines the added mass. The added mass force acting on a body is defined as :

$$\mathbf{F_M} = -\rho V \hat{\mathbf{C}} \frac{\mathbf{dU}}{\mathbf{dt}}, \tag{3.1}$$

V stands for the volume of the body and ρ for the fluid density surrounding the body. Its velocity $\mathbf{U}$ is expressed in the six degrees of freedom (translation and rotation). Including rotation requires inclusion of torques in $\mathbf{F_M}$, which is therefore a 6 components vector. $\hat{\mathbf{C}}$ is a tensor with 6×6 components. If we only consider translation, $\mathbf{F_M}$ becomes a 3 component

vector and $\hat{\mathbf{C}}$ a 3×3 component tensor. $\hat{\mathbf{C}}$ is called induced inertia tensor by Batchelor (2010).

As a consequence of $\hat{\mathbf{C}}$, $\mathbf{F_M}$ and $\mathbf{dU/dt}$ are generally misaligned depending on the body shape and the presence of other bodies or walls. This paper will only focus on the added mass coefficient of spherical bodies (bubbles).

This information is essential to completely characterize finely dispersed bubbly flows, where small spherical gas bubbles are present in a continuous liquid phase. Using either Porous Medium, Euler-Euler or Euler-Lagrange models, some authors use the widely accepted closure correlations [a.o. closure relations proposed by Tomiyama *et al.* (1995, 2002)]. As underlined by Darmana *et al.* (2009), since most of the closures are empirically obtained from experiments involving single bubble, their applicability to systems with high void fraction is questionable. Moreover, even if some correlations available in the literature take into account the effect of the local void fraction on added mass, very few numerical models use them. Ishii and Hibiki (2006) propose the use of correlation depending on void fraction proposed by Zuber (1964) but Tomiyama *et al.* (1995, 2002) propose the use of the added mass of a single bubble.

In particular, the effect of induced added mass on surrounding bubbles should be more appropriately emphasized. The induced added mass is the force exerted by one accelerating body to another through the fluid. When literature results are available, comparison with our results will be made. This paper uses solid harmonics to solve 3D potential flow around bubbles with various configurations.

A sphere in an infinite fluid medium experiences an added mass force collinear to its acceleration and the tensor $\hat{\mathbf{C}}$ is reduced to $\hat{\mathbf{C}} = 0.5\mathbf{I}$. $\mathbf{I}$ stands for the identity tensor [e.g., Milne-Thomson (1968), Brennen (2005)]. This means that a sphere displaces a volume of surrounding fluid equivalent to half of its volume. For the sake of brevity, we will study the added mass of spherical bodies which we will designate as bubbles.

Added mass forces are of interest in naval research (inertia forces of underwater or floating objects), for the chemical industry (bubble chamber), for the energy industry (oil and nuclear) and any application involving multiphase fluid dynamics. These industrial applications are particularly affected by two factors that can strongly modify inertia forces on dispersed bubbles or particles : presence of walls and other bubbles. A simple formula for $\hat{\mathbf{C}}$, depending only on these two factors, is needed to construct a good estimation of forces acting within a multiphase mixture.

Some of the simplest situations have already been solved analytically from the perspective of potential flow theory [Milne-Thomson (1968), Zuber (1964), Van Wijngaarden (1976), Sangani *et al.* (1991), Van Wijngaarden (1991),Wallis (1989), Cai and Wallis (1994)]. First authors until Van Wijngaarden (1991) accordingly with the first formulation of Zuber (1964) found an increase of added mass with void fraction. Wallis (1989) however found that the

added mass force decreases with the void fraction. Cai and Wallis (1994) proposed a more general description of added mass with two limiting cases as the one suggested by Zuber (1964) corresponding to an upper bound and the one suggested by Wallis (1989) corresponding to the lower bound, with an unknown parameter λ related to the external impedance of the cell around the bubble. The external impedance depends on the boundary conditions of the cell related to the bubble configuration. But as this value remains unknown, the authors concluded that there "may not exist a universal definition of added mass for an array of particles that can be applied to all the situations". Our paper solves this issue and proposes a model that can be applied for any array of identical spherical particles assuming a potential flow.

Some researchers have extended the first formulation of Zuber (1964). For example, Spelt and Sangani (1997) include velocity fluctuation effects or Kushch *et al.* (2002) ellipsoidal bubble shape effects. Some researchers have conducted DNS simulations [Niemann and Laurien (1991); Legendre *et al.* (2003); Simcik *et al.* (2008)] and finally few others have conducted experiments (Mokeyev (1977), Kendoush *et al.* (2007)). In the case of two bubbles, the numerical results of Legendre *et al.* (2003) show no influence of the Reynolds number (0.1 - 300) or of the acceleration parameter (0.1-1000) on the added mass force and a very good agreement between DNS and potential flow theory.

It is clear that the added mass force is a key parameter in the description of multiphase systems. It is particularly important in situations where the density ratio is large and the motion is unsteady. Thus, in this paper, we use a semi analytical method to explore the possibility of determining the added mass force in a variety of important situations.

Following the introduction, the paper includes four sections. In the first section, we expose a method to calculate the unsteady potential flow for a cloud of bubbles. The second section presents the procedure to deduce added mass force. The third section presents results for two bubbles. The fourth section presents a new formulation for the added mass forces. This formula is compared to results with a bubble close to a wall, a row and a column of bubbles. The fifth section presents results for regular and random clouds of bubbles and shows that the new model is able to accurately predict the added mass forces inside a cloud of bubbles. Finally, the main results are summarized in the conclusion section. Appendices are dedicated to readers wishing to have more information on the methodology.

3.2 Potential Flow

3.2.1 Solid Harmonics

If Φ is the velocity potential, it is the solution of Laplace's equation $\nabla^2\Phi = 0$ and can therefore be expressed as :

$$\Phi(\mathbf{r}) = \sum_{\ell=0}^{\infty} \sum_{m=-\ell}^{\ell} f_\ell^m \tilde{R}_\ell^m(\mathbf{r}) + g_\ell^m \tilde{S}_\ell^m(\mathbf{r}), \tag{3.2}$$

where f_ℓ^m and g_ℓ^m are constants and $\tilde{R}_\ell^m$ and $\tilde{S}_\ell^m$ are respectively the normalized regular and irregular solid harmonics, solutions of Laplace's equation :

$$\tilde{R}_\ell^m(\mathbf{r}) = \tilde{R}_\ell^m(r,\theta,\varphi) = (-1)^{\frac{|m|+m}{2}} r^\ell \tilde{Y}_\ell^m(\theta,\varphi) \qquad -\ell \le m \le \ell.$$

$$\tilde{S}_\ell^m(\mathbf{r}) = \tilde{S}_\ell^m(r,\theta,\varphi) = (-1)^{\frac{|m|+m}{2}} \frac{\tilde{Y}_\ell^m(\theta,\varphi)}{r^{\ell+1}} \qquad -\ell \le m \le \ell. \tag{3.3}$$

$\tilde{Y}_\ell^m(\theta,\varphi)$ are normalized spherical harmonics generally defined as

$$\tilde{Y}_\ell^m(\theta,\phi) = \sqrt{\frac{(\ell-|m|)!}{(\ell+|m|)!}}\ P_\ell^{|m|}(\cos\theta)\ e^{im\varphi} \qquad -\ell \le m \le \ell. \tag{3.4}$$

where P_ℓ^m are the associated Legendre polynomials. Note that the fully normalized associated Legendre polynomials are normalized such that

$$\int_{-1}^{1} \left(\tilde{P}_\ell^m\right)^2 dx = 1 \qquad 0 \le m \le \ell. \tag{3.5}$$

and are related to the unnormalized associated Legendre polynomials by

$$\tilde{P}_\ell^m(x) = (-1)^m \sqrt{\frac{(2\ell+1)(\ell-m)!}{2(\ell+m)!}} P_\ell^m(x) \qquad 0 \le m \le \ell. \tag{3.6}$$

Therefore, we can also define $\tilde{Y}_\ell^m(\theta,\varphi)$ as :

$$\tilde{Y}_\ell^m(\theta,\phi) = (-1)^m\sqrt{\frac{2}{2\ell+1}}\tilde{P}_\ell^{|m|}(\cos\theta)\; e^{im\varphi} \qquad -\ell \le m \le \ell. \tag{3.7}$$

For an isolated sphere of radius a_n and velocity $(U_n, \theta_n = 0, \varphi_n = 0)$ expressed in spherical coordinates, the velocity potential is well known [see Milne-Thomson (1968)] and defined as :

$$\phi_n = -\frac{U_n a_n^3}{2}\frac{\cos\theta}{r^2} = -\frac{U_n a_n^3}{2}\frac{z}{r^3}. \tag{3.8}$$

Applying a rotation of angle θ_n around the y-axis and angle φ_n around the z-axis, the general expression for the potential with the velocity expressed in spherical coordinates $(U_n, \theta_n, \varphi_n)$ is deduced :

$$\phi_n(\mathbf{r}) = -\frac{U_n a_n^3}{2r^2}\left[\cos\theta_n\cos\theta + \sin\theta_n\sin\theta\left(\sin\varphi_n\sin\varphi + \cos\varphi_n\cos\varphi\right)\right], \tag{3.9}$$

Introducing $\dot{x}_n$,$\dot{y}_n$,$\dot{z}_n$ we have :

$$\phi_n(\mathbf{r}) = -\frac{a_n^3}{2r^2}\left(\dot{z}_n\cos\theta + \dot{x}_n\sin\theta\sin\varphi + \dot{y}_n\sin\theta\cos\varphi\right). \tag{3.10}$$

or as a function of normalized spherical harmonics :

$$\phi_n(\mathbf{r}) = \frac{a_n^3}{2r^2}\left\{-\dot{z}_n\tilde{Y}_1^0(\theta,\varphi) + \frac{\sqrt{2}}{2}\left[(\dot{x}_n + \imath\dot{y}_n)\tilde{Y}_1^{-1}(\theta,\varphi) + (\dot{x}_n - \imath\dot{y}_n)\tilde{Y}_1^1(\theta,\varphi)\right]\right\}. \tag{3.11}$$

3.2.2 Potential flow around N_b bubbles

To calculate the potential flow around N_b bubbles, the radius and velocity of the n^{th} bubble are respectively denoted as a_n and $(\dot{x}_n, \dot{y}_n, \dot{z}_n)$. The potential is defined as :

$$\Phi = \sum_{n=1}^{N_b}\sum_{\ell=0}^{\infty}\sum_{m=-\ell}^{\ell} f_{\ell,n}^m\tilde{R}_\ell^m(\mathbf{r_n}) + g_{\ell,n}^m\tilde{S}_\ell^m(\mathbf{r_n}), \tag{3.12}$$

$\mathbf{r_n}$ is the position vector expressed in the frame of the n^{th} bubble. $f_{\ell,n}^m$ and $g_{\ell,n}^m$ are constants to be determined. However, as the velocity should converge to zero when $r \to \infty$, we must have $f_{\ell,n}^m = 0, \forall m, \ell, n$ in equation (3.12) above [see solid harmonics definition (3.2)]. $g_{\ell,n}^m$ constants will be determined by the no penetration condition which compels the normal velocity at the surface of the n^{th} bubble ($\mathbf{a_n}$) to be equal to the normal velocity of an isolated bubble. Thus,

the potential derivative is :

$$\frac{\mathrm{d}\Phi}{\mathrm{d}r_n}(\mathbf{a_n}) = \frac{\mathrm{d}\phi_n}{\mathrm{d}r_n}(\mathbf{a_n}) = \dot{z}_n\tilde{Y}_1^0(\theta,\varphi) - \frac{\sqrt{2}}{2}\left((\dot{x}_n + \imath\dot{y}_n)\tilde{Y}_1^{-1}(\theta,\varphi) + (\dot{x}_n - \imath\dot{y}_n)\tilde{Y}_1^1(\theta,\varphi)\right). \quad (3.13)$$

where ϕ_n is the potential for a sphere moving in an infinite medium defined in equation (3.11).

Therefore, we need to express ϕ_n and Φ in terms of $\mathbf{r_k}$. Yet the expression of S_ℓ^m expressed in the frame attached to the center of the n^{th} bubble is (cf. Van Gelderen (1998)) :[1]

$$\begin{aligned}
&\text{if } \|\mathbf{r_k}\| < \|\mathbf{c_{nk}}\| \\
&\tilde{S}_\ell^m(\mathbf{r_n}) = \tilde{S}_\ell^m(\mathbf{c_{nk}} + \mathbf{r_k}) = \sum_{\lambda=0}^{\infty}\sum_{\mu=-\lambda}^{\lambda} D_{\ell,\lambda}^{m,\mu}\tilde{S}_{\lambda+\ell}^{m-\mu}(\mathbf{c_{nk}})\tilde{R}_\lambda^\mu(\mathbf{r_k}) \\
&\text{with} \\
&D_{\ell,\lambda}^{m,\mu} = (-1)^{\lambda+\mu}\sqrt{\binom{\lambda+\ell+m-\mu}{\ell+m}\binom{\lambda+\ell-m+\mu}{\ell-m}}.
\end{aligned} \quad (3.14)$$

where $\mathbf{c_{nk}}$ is the center of the k^{th} bubble expressed in the frame attached to the center of the n^{th} bubble [see Figure 3.1 ($\mathbf{r_n} = \mathbf{c_{nk}} + \mathbf{r_k}$)]. We deduce from Eq. (3.12) :

$$\Phi = \sum_{\ell=0}^{\infty}\sum_{m=-\ell}^{\ell}\left[\sum_{\substack{n=1\\n\neq k}}^{N_b}\left(g_{\ell,n}^m\sum_{\lambda=0}^{\infty}\sum_{\mu=-\lambda}^{\lambda} D_{\ell,\lambda}^{m,\mu}\tilde{R}_\lambda^\mu(\mathbf{r_k})\tilde{S}_{\lambda+\ell}^{m-\mu}(\mathbf{c_{nk}})\right) + g_{\ell,k}^m\tilde{S}_\ell^m(\mathbf{r_k})\right], \quad (3.15)$$

with the definition of $\tilde{R}_\lambda^\mu$ and $\tilde{S}_\lambda^\mu$ (3.3), we have :

$$\frac{\mathrm{d}\Phi}{\mathrm{d}r_k}(\mathbf{a_k}) = \sum_{\ell=0}^{\infty}\sum_{m=-\ell}^{\ell}\left(\sum_{\substack{n=1\\n\neq k}}^{N_b} G_{\ell,n}^m(\mathbf{a_k}) - g_{\ell,k}^m(-1)^{\frac{|m|+m}{2}}\frac{\ell+1}{a_k^{\ell+2}}\tilde{Y}_\ell^m(\theta_k,\varphi_k)\right), \quad (3.16)$$

where

$$G_{\ell,n}^m(\mathbf{a_k}) = g_{\ell,n}^m\sum_{\lambda=0}^{\infty}\sum_{\mu=-\lambda}^{\lambda}(-1)^{\frac{\mu+|\mu|}{2}} D_{\ell,\lambda}^{m,\mu}\lambda a_k^{\lambda-1}\tilde{S}_{\lambda+\ell}^{m-\mu}(\mathbf{c_{nk}})\tilde{Y}_\lambda^\mu(\theta_k,\varphi_k). \quad (3.17)$$

As the $\tilde{Y}_\lambda^\mu$ constitute an orthogonal basis, the no penetration condition (3.13) is equivalent to :

1. Note that the translation formula contains a typographical error as the sum on μ should be between $-\lambda$ and λ.

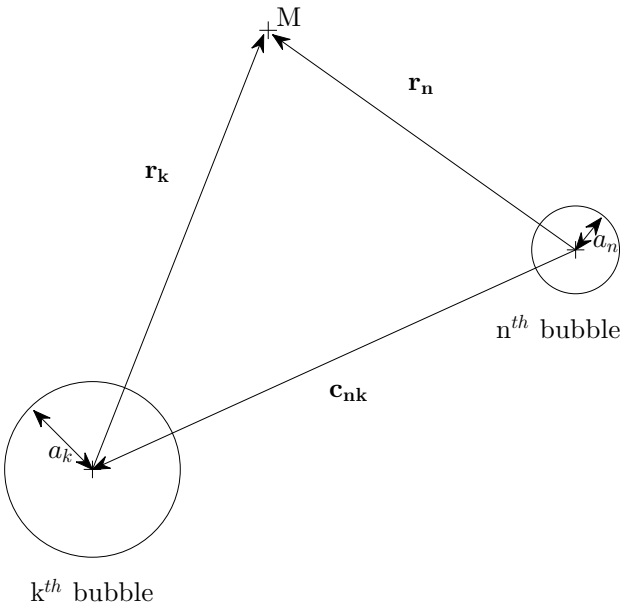

Figure 3.1 Illustration of the change of reference frame. $\mathbf{c_{nk}}$ is the center of the k^{th} bubble expressed in the frame attached to the center of the n^{th} bubble. a_k is the radius of the k^{th} bubble.

$\forall k \in \mathbb{N}, k \leq N_b, \forall \lambda \in \mathbb{N}, \forall \mu \in \mathbb{Z}, |\mu| \leq \lambda$

$$\sum_{\substack{n=1 \\ n \neq k}}^{N_b} \left(\sum_{\ell=0}^{\infty} \sum_{m=-\ell}^{\ell} g_{\ell,n}^{m} (-1)^{\frac{\mu+|\mu|}{2}} D_{\ell,\lambda}^{m,\mu} \lambda a_k^{\lambda-1} \tilde{S}_{\lambda+\ell}^{m-\mu}(\mathbf{c_{nk}}) \right) - g_{\lambda,k}^{\mu} (-1)^{\frac{|\mu|+\mu}{2}} \frac{\lambda+1}{a_k^{\lambda+2}} = \delta_{\lambda,1} L_k^{\mu}$$

with :

$$L_k^{\mu} = \begin{cases} -\dfrac{\sqrt{2}}{2}(\dot{x}_k + \imath \dot{y}_k) & \text{if } \mu = -1 \\ \dot{z}_k & \text{if } \mu = 0 \\ -\dfrac{\sqrt{2}}{2}(\dot{x}_k - \imath \dot{y}_k) & \text{if } \mu = 1 \end{cases} \tag{3.18}$$

By limiting $l \leq L$, this becomes a system of $N_b(L+1)^2$ linear equations to solve (see Appendix 3.8.A for the numerical approach description).

3.3 Added mass forces

3.3.1 Added and Induced added Mass Theory

The unsteady Bernoulli equation for a constant density is :

$$P = \underbrace{-\rho\frac{\partial\Phi}{\partial t}}_{\text{unsteady term}} \underbrace{-\frac{1}{2}\rho U^2 - \rho g z + P_0}_{\text{steady terms}}, \tag{3.19}$$

where Φ is the velocity potential. In the case of the flow around N_b bubbles, with arbitrary location, velocity and acceleration we denote :

$$\frac{\partial\Phi}{\partial\mathbf{U_n}} = \begin{pmatrix} \dfrac{\partial\Phi}{\partial\dot{x}_n} \\ \dfrac{\partial\Phi}{\partial\dot{y}_n} \\ \dfrac{\partial\Phi}{\partial\dot{z}_n} \end{pmatrix}, \frac{\mathbf{dU_n}}{\mathbf{dt}} = \begin{pmatrix} \ddot{x}_n \\ \ddot{y}_n \\ \ddot{z}_n \end{pmatrix}, \frac{\partial\Phi}{\partial\mathbf{r_n}} = \begin{pmatrix} \dfrac{\partial\Phi}{\partial x_n} \\ \dfrac{\partial\Phi}{\partial y_n} \\ \dfrac{\partial\Phi}{\partial z_n} \end{pmatrix} \text{ and } \mathbf{U_n} = \begin{pmatrix} \dot{x}_n \\ \dot{y}_n \\ \dot{z}_n \end{pmatrix} \tag{3.20}$$

where (x_n, y_n, z_n) denotes the n^{th} bubble location. We then have on the k^{th} sphere surface [see Kumaran and Koch (1993)] :

$$\frac{\partial\Phi}{\partial t} = \sum_{n=1}^{N_b} \frac{\partial\Phi}{\partial\mathbf{U_n}} \cdot \frac{\mathbf{dU_n}}{\mathbf{dt}} + \sum_{n=1}^{N_b} \frac{\partial\Phi}{\partial\mathbf{r_n}} \cdot \mathbf{U_n} - \nabla\Phi \cdot \mathbf{U_k}. \tag{3.21}$$

This generalizes the single body problem by Batchelor (2010). Batchelor divides the potential flow as the scalar product of the vector $\mathbf{\Phi}$ and body velocity such as

$$\Phi = \mathbf{\Phi} \cdot \mathbf{U} \tag{3.22}$$

As the velocity potential is linear with each bubble velocity, $\mathbf{\Phi}$ is in fact equal to $\partial\Phi/\partial\mathbf{U_n}$ and depend on the bubble locations only and not on their velocity. We deduce the active force on a body as the prime integration of the pressure on its boundary. The added mass force corresponds to the acceleration dependent term. All terms, except the first sum, in equation (3.21) above are velocity dependent and therefore not related to the added mass

force. Consequently, for the k^{th} bubble of radius a, the total added mass force is :

$$\mathbf{F_{M_k}} = \underbrace{\int_{\theta=0}^{\pi}\int_{\varphi=0}^{2\pi}\rho\frac{\partial\Phi}{\partial\mathbf{U_k}}\frac{\mathbf{dU_k}}{\mathbf{dt}}\mathbf{dS_k}}_{\text{added mass}} + \underbrace{\int_{\theta=0}^{\pi}\int_{\varphi=0}^{2\pi}\rho\sum_{\substack{n=1\\n\neq k}}^{N_b}\frac{\partial\Phi}{\partial\mathbf{U_n}}\frac{\mathbf{dU_n}}{\mathbf{dt}}\mathbf{dS_k}}_{\text{induced added mass}}. \tag{3.23}$$

Thus, we can write

$$\mathbf{F_{M_k}} = -\rho\frac{4\pi a_k^3}{3}\sum_{n=1}^{N_b}\hat{\mathbf{C}}_{\mathbf{nk}}\frac{\mathbf{dU_n}}{\mathbf{dt}} \tag{3.24}$$

where $\hat{\mathbf{C}}_{\mathbf{nk}}$ is the added mass tensor when $n = k$ and the induced added mass tensor otherwise. We have :

$$\begin{aligned}\hat{\mathbf{C}}_{\mathbf{nk}} &= -\frac{3}{4\pi a_k^3}\int_{\theta=0}^{\pi}\int_{\varphi=0}^{2\pi}\frac{\partial\Phi}{\partial\mathbf{U_n}}\mathbf{dS_k}\\ &= -\frac{3}{4\pi a_k}\int_{\theta=0}^{\pi}\int_{\varphi=0}^{2\pi}\begin{pmatrix}\frac{\partial\Phi}{\partial\dot{x}_n}\sin^2\theta\cos\varphi & \frac{\partial\Phi}{\partial\dot{y}_n}\sin^2\theta\cos\varphi & \frac{\partial\Phi}{\partial\dot{z}_n}\sin^2\theta\cos\varphi\\ \frac{\partial\Phi}{\partial\dot{x}_n}\sin^2\theta\sin\varphi & \frac{\partial\Phi}{\partial\dot{y}_n}\sin^2\theta\sin\varphi & \frac{\partial\Phi}{\partial\dot{z}_n}\sin^2\theta\sin\varphi\\ \frac{\partial\Phi}{\partial\dot{x}_n}\sin\theta\cos\theta & \frac{\partial\Phi}{\partial\dot{y}_n}\sin\theta\cos\theta & \frac{\partial\Phi}{\partial\dot{z}_n}\sin\theta\cos\theta\end{pmatrix}d\theta d\varphi.\end{aligned} \tag{3.25}$$

This notation will be used in what follows.

3.3.2 Added and Induced added Mass Calculus

As shown in the previous section we are able to solve the potential flow for any cloud of bubbles. This section shows how to deduce the associated added mass tensor and forces. According to equation (3.25), for the k^{th} bubble of radius a_k, denoting generically $\partial\Phi/\partial\dot{\bullet}_n = \Phi_{,\dot{\bullet}_n}$ we have :we have :

$$\begin{pmatrix}C_{\bullet x}\\ C_{\bullet y}\\ C_{\bullet z}\end{pmatrix}_{nk} = -\frac{3}{4\pi a_k}\int_{\theta=0}^{\pi}\int_{\varphi=0}^{2\pi}\Phi_{,\dot{\bullet}_n}\begin{pmatrix}\sin^2\theta\cos\varphi\\ \sin^2\theta\sin\varphi\\ \sin\theta\cos\theta\end{pmatrix}d\theta d\varphi. \tag{3.26}$$

Yet, according to equations (3.12) and (3.18) the velocity potential is linear with each bubble velocity. Consequently $\partial\Phi/\partial\dot{x}_n = \Phi_{,\dot{x}_n}$ is equivalent to the potential flow with $\forall k \neq n, \dot{x}_k = \dot{y}_k = \dot{z}_k = 0$, $\dot{y}_n = \dot{z}_n = 0$ and $\dot{x}_n = 1$. Therefore, three calculations ($\dot{x}_n = 1$, $\dot{y}_n = 1$ and $\dot{z}_n = 1$) will allow us to construct the complete added mass tensor. From the definition of solid harmonics (3.3) and equation (3.15), we have on the k^{th} bubble surface :

$$\begin{aligned}\Phi_{,\dot{\bullet}_n} &= \sum_{\ell=0}^{\infty}\sum_{m=-\ell}^{\ell}\sum_{\substack{n=1\\n\neq k}}^{N_b}\left(g_{\ell,n}^{m}\sum_{\lambda=0}^{\infty}\sum_{\mu=-\lambda}^{\lambda}D_{\ell,\lambda}^{m,\mu}Q_{\lambda}^{\mu}a_k^{\lambda}P_{\lambda}^{|\mu|}(\cos\theta)e^{\imath\mu\varphi}\tilde{S}_{\lambda+\ell}^{m-\mu}(\mathbf{c_{nk}})\right)+\ldots \\ &\quad \sum_{\ell=0}^{\infty}\sum_{m=-\ell}^{\ell}g_{\ell,k}^{m}\frac{Q_{\ell}^{m}}{a_k^{\ell+1}}P_{\ell}^{|m|}(\cos\theta)e^{\imath m\varphi}\end{aligned} \tag{3.27}$$

with

$$Q_{\ell}^{m} = (-1)^{\frac{m+|m|}{2}}\sqrt{\frac{(\ell-|m|)!}{(\ell+|m|)!}} \tag{3.28}$$

Consequently, we obtain :

$$\begin{aligned}\begin{pmatrix} C_{\bullet x}\\ C_{\bullet y}\\ C_{\bullet z}\end{pmatrix}_{nk} &= -\frac{3}{4\pi a_k}\int_{\theta=0}^{\pi}\int_{\varphi=0}^{2\pi}\Phi_{,\bullet_n}\begin{pmatrix}\sin^2\theta\cos\varphi\\ \sin^2\theta\sin\varphi\\ \sin\theta\cos\theta\end{pmatrix}d\theta d\varphi. \\ &= -\sum_{\ell=0}^{\infty}\sum_{m=-\ell}^{\ell}\sum_{\substack{n=1\\n\neq k}}^{N_b}\left(g_{\ell,n}^{m}\sum_{\lambda=0}^{\infty}\sum_{\mu=-\lambda}^{\lambda}D_{\ell,\lambda}^{m,\mu}Q_{\lambda}^{\mu}a_k^{\lambda-1}\tilde{S}_{\lambda+\ell}^{m-\mu}(\mathbf{c_{nk}})\mathbf{I}_{\lambda}^{\mu}\right)+\ldots \\ &\quad \sum_{\ell=0}^{\infty}\sum_{m=-\ell}^{\ell}\frac{g_{\ell,k}^{m}}{a_k^{\ell+2}}\mathbf{I}_{\ell}^{m}\end{aligned} \tag{3.29}$$

with

$$\mathbf{I}_{\lambda}^{\mu} = -\frac{3}{4\pi}\int_{\theta=0}^{\pi}\int_{\varphi=0}^{2\pi}Q_{\lambda}^{\mu}P_{\lambda}^{|\mu|}(\cos\theta)e^{\imath\mu\varphi}\begin{pmatrix}\sin^2\theta\cos\varphi\\ \sin^2\theta\sin\varphi\\ \sin\theta\cos\theta\end{pmatrix}d\theta d\varphi. \tag{3.30}$$

Thanks to the orthogonality of associated Legendre polynomials, we conclude that we have $\mathbf{I}_\lambda^\mu = 0$ except for :

$$\mathbf{I}_1^{-1} = \frac{1}{\sqrt{2}}\begin{pmatrix} 1 \\ -\imath \\ 0 \end{pmatrix}, \mathbf{I}_1^0 = \frac{1}{\sqrt{2}}\begin{pmatrix} 0 \\ 0 \\ -\sqrt{2} \end{pmatrix} \text{ and } \mathbf{I}_1^1 = -\frac{1}{\sqrt{2}}\begin{pmatrix} 1 \\ \imath \\ 0 \end{pmatrix}. \tag{3.31}$$

Finally, we obtain :

$$\begin{aligned}\begin{pmatrix} C_{\bullet x} \\ C_{\bullet y} \\ C_{\bullet z} \end{pmatrix}_{nk} = & \sum_{\ell=0}^{\infty}\sum_{m=-\ell}^{\ell}\sum_{\substack{n=1 \\ n\neq k}}^{N_b} \frac{g_{\ell,n}^m}{\sqrt{2}} \begin{pmatrix} D_{\ell,1}^{m,-1}\tilde{S}_{\ell+1}^{m+1}(\mathbf{c_{nk}}) - D_{\ell,1}^{m,1}\tilde{S}_{\ell+1}^{m-1}(\mathbf{c_{nk}}) \\ -\imath(D_{\ell,1}^{m,-1}\tilde{S}_{\ell+1}^{m+1}(\mathbf{c_{nk}}) + D_{\ell,1}^{m,1}\tilde{S}_{\ell+1}^{m-1}(\mathbf{c_{nk}})) \\ -\sqrt{2}D_{\ell,1}^{m,0}\tilde{S}_{\ell+1}^{m}(\mathbf{c_{nk}}) \end{pmatrix} + \dots \\ & \frac{1}{\sqrt{2}a_k^3}\begin{pmatrix} g_{1,k}^{-1} - g_{1,k}^1 \\ -\imath(g_{1,k}^{-1} + g_{1,k}^1) \\ -\sqrt{2}g_{1,k}^0 \end{pmatrix}.\end{aligned} \tag{3.32}$$

Appendix 3.8.B details the numerical implementation of this equation.

3.3.3 Convergence study of the Added mass coefficient computation

In the case of one bubble of radius a moving at a constant velocity U_b, the added mass coefficient can also be evaluated through the total kinetic energy in the fluid as [see Milne-Thomson (1968)] :

$$T = \frac{1}{2}\iiint \rho(\nabla\Phi)^2 dV = \frac{1}{2}\rho\left(\frac{4}{3}\pi a^3\right)C_M U_b^2. \tag{3.33}$$

where Φ is the velocity potential around one bubble of radius a moving at a constant velocity U_b. As $(\nabla\Phi)^2 = \nabla\cdot(\Phi\nabla\Phi) + \Delta^2\Phi$, the divergence theorem allows us to write :

$$C_M = \frac{2T}{\rho\left(\frac{4}{3}\pi a^3\right)U_b^2} = \frac{3}{4\pi a U_b^2}\int_{\theta=0}^{\pi}\int_{\varphi=0}^{2\pi}\Phi(a)\frac{\partial\Phi}{\partial r}(a)\sin\theta d\theta d\varphi. \tag{3.34}$$

In the case of two identical bubbles moving toward one another with the same velocity, the plane between the two bubbles is a plane of symmetry which is equivalent to an infinite rigid

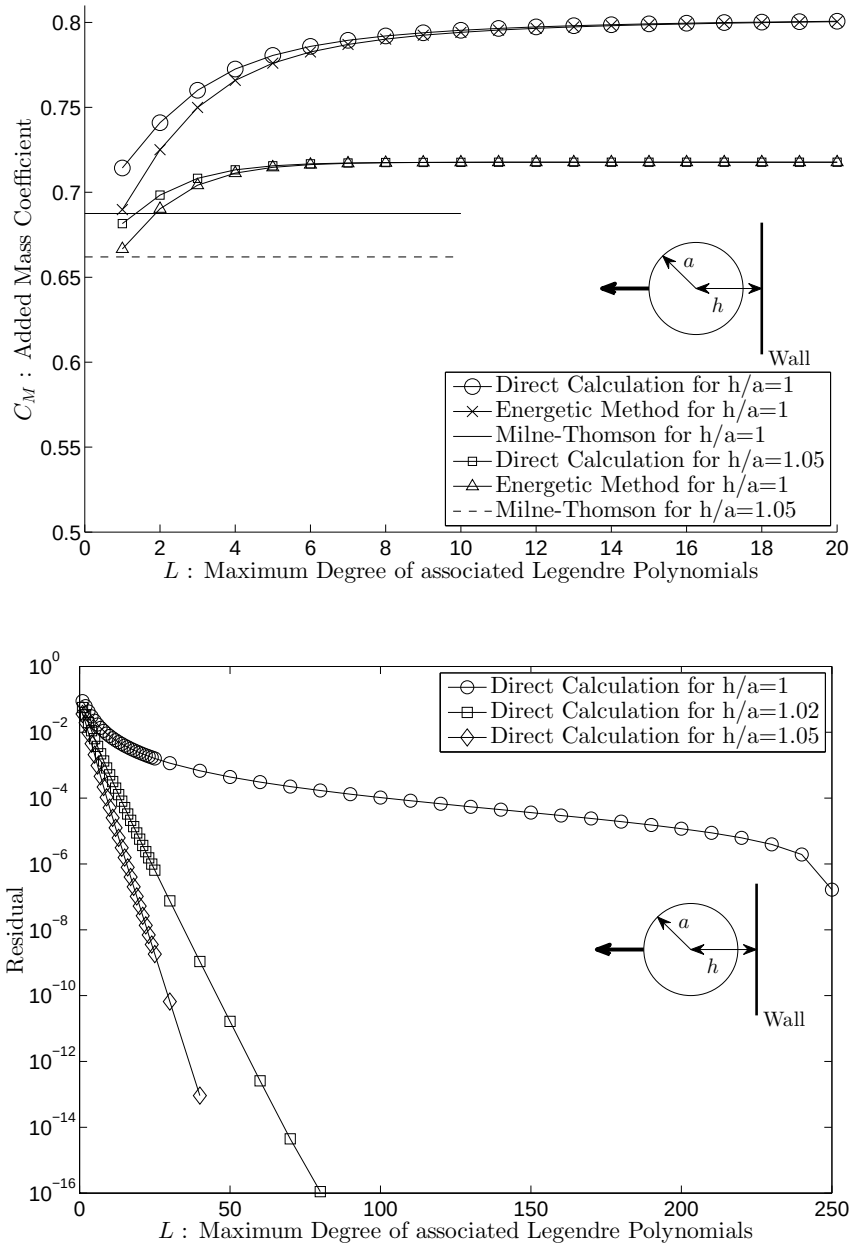

Figure 3.2 Convergence study.

wall. Consequently the added mass of a bubble approaching a wall is :

$$C_M = \frac{T}{\rho\left(\frac{4}{3}\pi a^3\right)U_b^2} = \frac{3}{8\pi a U_b^2}\sum_{n=1}^{2}\int_{\theta_n=0}^{\pi}\int_{\varphi_n=0}^{2\pi}\Phi(a_n)\frac{\partial\Phi}{\partial r}(a_n)\sin\theta d\theta d\varphi. \tag{3.35}$$

The energy approach leads to the same added mass as our direct approach as long as the non penetration condition is satisfied $\partial\Phi/\partial r(a_n) = \partial\phi_n/\partial r(a_n)$ (3.13).

Consequently, the added mass coefficient calculated directly (3.32) becomes closer to that obtained with the energy approach (3.35) as the no penetration condition becomes more accurate. This fact is used as an additional convergence proof presented in Figure 3.2.

The convergence study was performed in order to evaluate the required number of Associated Legendre polynomials for a desired accuracy, previously denoted as L (see Appendix 3.8.A). The case chosen for the convergence study is that of one bubble moving perpendicularly to a wall at a distance of 1.1 radius of its center. Figure 3.2 also presents the residual for direct approaches ($|C_M(L) - C_M(L = 251)|$).

As shown in table 3.1, using the direct approach and limiting to L =10 the maximum degree of Associated Legendre polynomials allows to already have four significant digits.

3.4 Results : two Bubbles

3.4.1 Added mass and induced mass of two side by side and in-line bubbles

This section focuses on the case of two identical bubbles where only one accelerates. If we number "1" the accelerating bubble and "2" the second one, according to the previous notation, $\mathbf{c_{12}}$ is the vector going from the center of the first bubble to the center of the second bubble. For the sake of brevity, we will denote the distance separating the two bubbles c where $c = \|\mathbf{c_{12}}\|$.

Figure 3.3 presents the scalar components of added mass and induced added mass tensor for two bubbles. In Figure 3.3 (a) one bubble is accelerating perpendicular to the line joining the two bubbles centers. The added and induced added mass forces are parallel and opposed to the acceleration. In Figure 3.3 (b) one bubble is accelerating parallel to the line joining the two bubbles centers. The added and induced added mass forces are again parallel to the acceleration. However, the induced added mass force is in the same direction as that of the acceleration ; scalar component of the induced added mass tensor is negative [see definition of added mass forces (3.1)]. Taylor expansions of these two cases can be calculated using Kok (1993) approach (see Appendix 3.8.C and 3.8.D). If the two bubbles centers belong to the $z-$axis, added mass and induced added mass tensors are defined by the four following new relations :

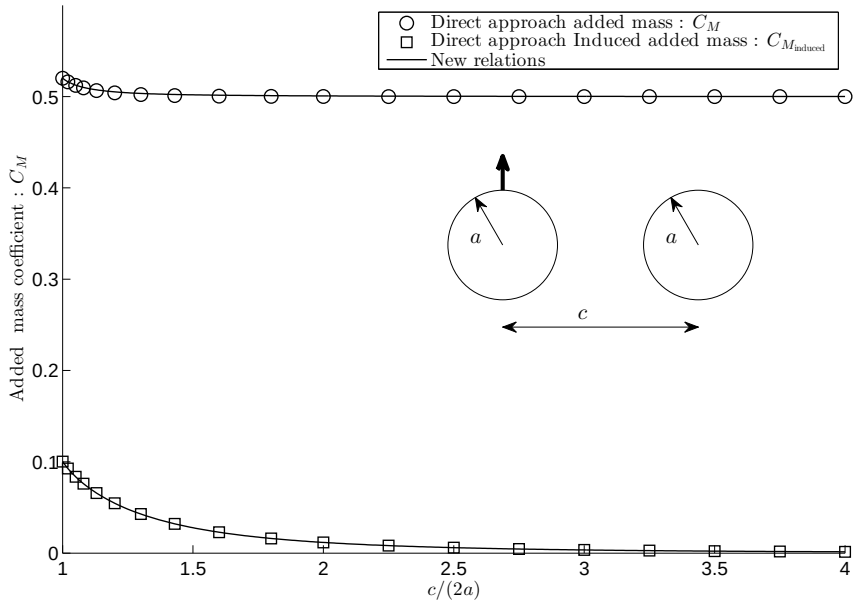

(a) side by side bubbles.

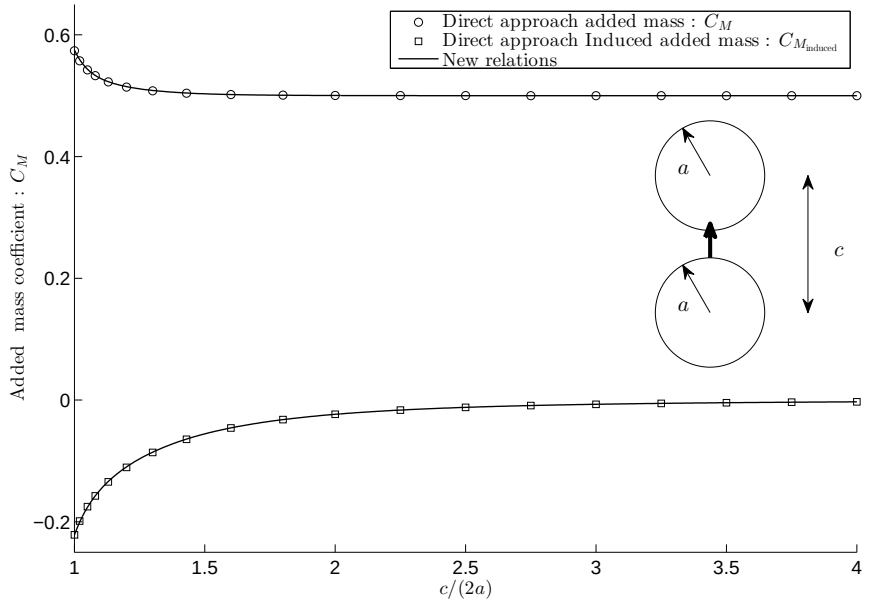

(b) in-line bubbles

Figure 3.3 Added mass (on bubble "1") and induced added mass coefficient (on bubble "2") of two identical bubbles (the accelerating bubble is numbered "1" and the second "2").

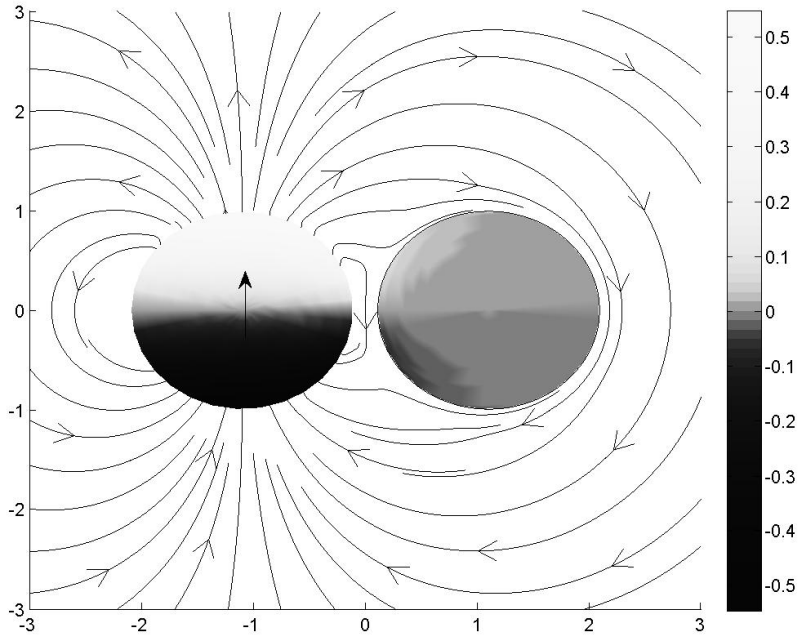

(a) side by side bubbles.

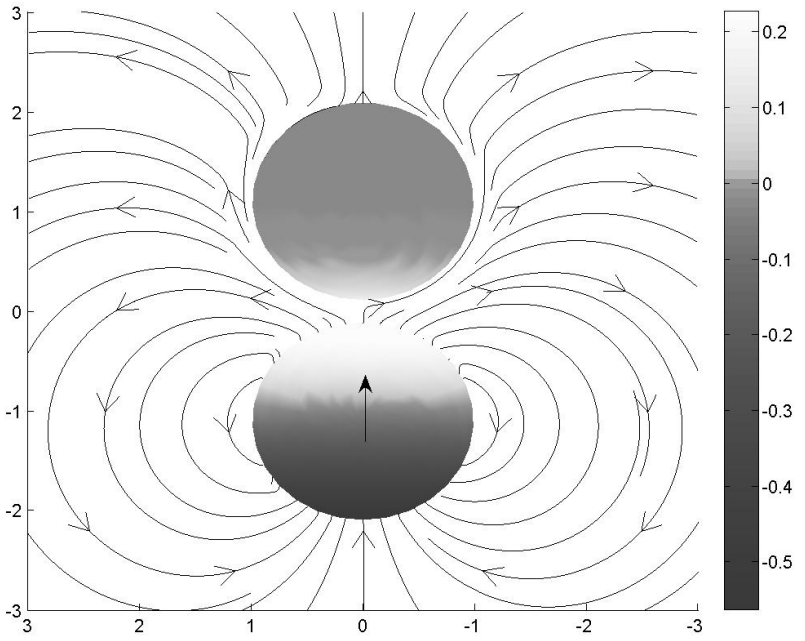

(b) in-line bubbles.

Figure 3.4 Pressure on surface and acceleration streamlines of two identical bubbles where only one accelerates.

Tableau 3.1 Convergence study results.

L	C_M	L	C_M
0	0.5939143	8	0.6755721
1	0.6554726	9	0.6755879
2	0.6663727	**10**	**0.6755937**
3	0.6718499	11	0.6755958
4	0.6741711	12	0.6755966
5	0.6750725	13	0.6755969
6	0.6754069	14	0.6755970
7	0.6755283	15	0.6755971

Added mass tensor $\mathbf{C_{11}}$

- Side by side bubbles

$$C_{xx} = \frac{1}{2}\left[1 + \frac{3}{256}\left(\frac{2a}{c}\right)^6 + \frac{3}{256}\left(\frac{2a}{c}\right)^8 + \frac{27}{4096}\left(\frac{2a}{c}\right)^{10} + \sum_{n=12}^{\infty} e_n \left(\frac{2a}{c}\right)^n\right]$$
$$C_{yy} = C_{xx}, \tag{3.36}$$

- In-line bubbles

$$C_{zz} = \frac{1}{2}\left[1 + \frac{3}{64}\left(\frac{2a}{c}\right)^6 + \frac{9}{256}\left(\frac{2a}{c}\right)^8 + \frac{9}{512}\left(\frac{2a}{c}\right)^{10} + \sum_{n=12}^{\infty} d_n \left(\frac{2a}{c}\right)^n\right]$$

Induced Added mass tensor $\mathbf{C_{12}}$

- Side by side bubbles

$$\begin{aligned} C_{xx\ \mathrm{ind}} &= \frac{1}{2}\left[\frac{3}{16}\left(\frac{2a}{c}\right)^3 + \frac{3}{4096}\left(\frac{2a}{c}\right)^9 + \frac{3}{2048}\left(\frac{2a}{c}\right)^{11} + \sum_{n=12}^{\infty} e_n^{ind}\left(\frac{2a}{c}\right)^n\right] \\ C_{yy\ \mathrm{ind}} &= C_{xx\ \mathrm{ind}}, \end{aligned} \tag{3.37}$$

- In-line bubbles

$$C_{zz\ \mathrm{ind}} = \frac{1}{2}\left[-\frac{3}{8}\left(\frac{2a}{c}\right)^3 - \frac{3}{512}\left(\frac{2a}{c}\right)^9 - \frac{9}{1024}\left(\frac{2a}{c}\right)^{11} + \sum_{n=12}^{\infty} d_n^{ind}\left(\frac{2a}{c}\right)^n\right].$$

with exact values of d_n and d_n^{ind} are presented in tables 3.2 and 3.3 for $n < 70$ and $n < 66$ respectively. Exact values of e_n and e_n^{ind} are presented in tables 3.4 and 3.5 for $n < 42$.

Note that in this basis, both tensors are diagonal. As no forces are observed in the direction perpendicular to the acceleration.

As shown by previous equations (3.36) and (3.37), the side by side case leads to smaller added and induced added mass forces than the in-line case. Figures 3.4 (a) and (b) provide a good explanation. Figure 3.4 (a) presents side by side bubbles, the left bubble accelerates upwards; Figure 3.4 (b) presents in-line bubbles, the downside bubble accelerates upward. In both cases the second bubble is at rest. Pressure on its surface represents the induced added mass effect. *Note that the color chart is not linear with pressure in order to magnify the pressure profile on the bubble.* For the in-line case, the accelerating bubble creates a larger gap between the bubbles than for the side by side case. Consequently, this creates a larger depression behind the accelerating bubble thus resulting in a loop of acceleration streamlines. Finally, in-line and side by side cases are completely different, both in terms of magnitude and direction of the induced added mass. This leads to completely different added mass forces for accelerating bubble columns and rows.

3.4.2 Convergence study of the analytical Added mass coefficient calculation

In equation (3.36) and (3.37) the maximum admissible value of $2a/c$ is unity. The evolution of coefficients d_n, d_n^{ind}, e_n, e_n^{ind} gives raise an error estimate. As presented in Figure 3.5 we can conjecture that the coefficient d_n and e_n follow respectively $1.5/n^2$ and $1/n^{2.4}$ laws for

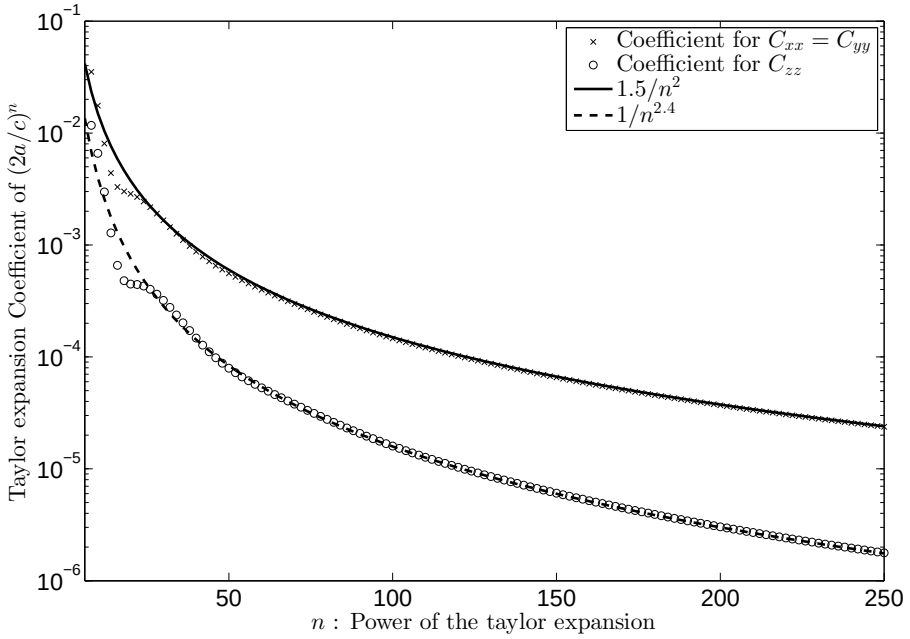

(a) component of Added mass tensor.

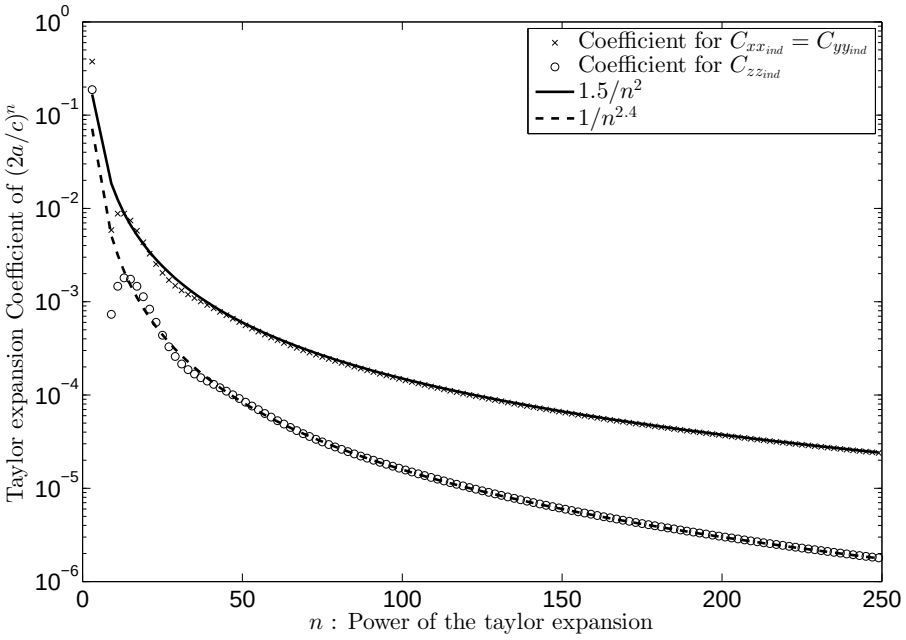

(b) component of Induced Added mass tensor.

Figure 3.5 Coefficient of the Taylor expansion of the component of added mass and induced added mass tensor.

$n > 250$. Indeed, we verify :

$$\begin{aligned}
\frac{1.45}{n^2} < \quad d_n \quad < \frac{1.55}{n^2} \qquad & \text{for n is even and } n \in [68\text{-}250] \\
-\frac{1.55}{n^2} < \quad d_n^{ind} \quad < -\frac{1.45}{n^2} \qquad & \text{for n is odd and } n \in [71\text{-}250] \\
\frac{0.95}{n^{2.4}} < \quad e_n \quad < \frac{1.05}{n^{2.4}} \qquad & \text{for n is even and } n \in [42\text{-}250] \\
\frac{0.95}{n^{2.4}} < \quad e_n^{ind} \quad < \frac{1.05}{n^{2.4}} \qquad & \text{for n is odd and } n \in [43\text{-}250]
\end{aligned} \tag{3.38}$$

The maximum power of the Taylor expansion is equal to the maximum Legendre polynomial considered. The numerical method truncation to $L = 250$ is equivalent to the analytical Taylor expansion truncation to N=250. Consequently, we neglect the following terms

$$\begin{aligned}
&\text{For } \frac{c}{2a} = 1 && \text{For } \frac{c}{2a} = 1.1 \\
&\sum_{n=250}^{\infty} d_n < \int_{250}^{\infty} \frac{1.5}{x^2} dx \leq 0.006 && \sum_{n=250}^{\infty} \frac{d_n}{1.1^n} < 1.1\ 10^{-14} \\
&\text{and} \\
&\sum_{n=250}^{\infty} e_n < \int_{250}^{\infty} \frac{1}{x^{2.4}} dx \leq 0.0032 && \sum_{n=250}^{\infty} \frac{e_n}{1.1^n} < 8\ 10^{-16}
\end{aligned} \tag{3.39}$$

Choosing $L = 250$, we reach for the added mass coefficient a 2 digit accuracy for $c/(2a) = 1$ and 13-digit accuracy for $c/(2a) = 1.1$. This proves that the accuracy increases significantly as $c/(2a)$ becomes greater than unity as shown by the residuals convergence (see Figure 3.2).

3.4.3 Added mass and induced mass of two bubbles with an angle

When the acceleration is at an angle relative to the line joining the two bubbles centers, there are two components of the added mass force that can be deduced from the tensor described previously in Eq. (3.36) and (3.37). In order to define a basis, we define the vector $\mathbf{N_{12}}$ as the unit vector in the direction $\mathbf{c_{12}}$. The vector $\mathbf{T_{12}}$ completes the basis in the plane containing $\mathbf{c_{12}}$ and $\mathbf{dU_1/dt}$. The angle α_{12} is the angle between $\mathbf{N_{12}}$ and $\mathbf{dU_1/dt}$ or, written differently the angle between the line joining the two bubbles centers and the acceleration vector. The angle α_{12} is equal to 0 when $\mathbf{dU_1/dt}$ and $\mathbf{N_{12}}$ are collinear and to $\pi/2$ when

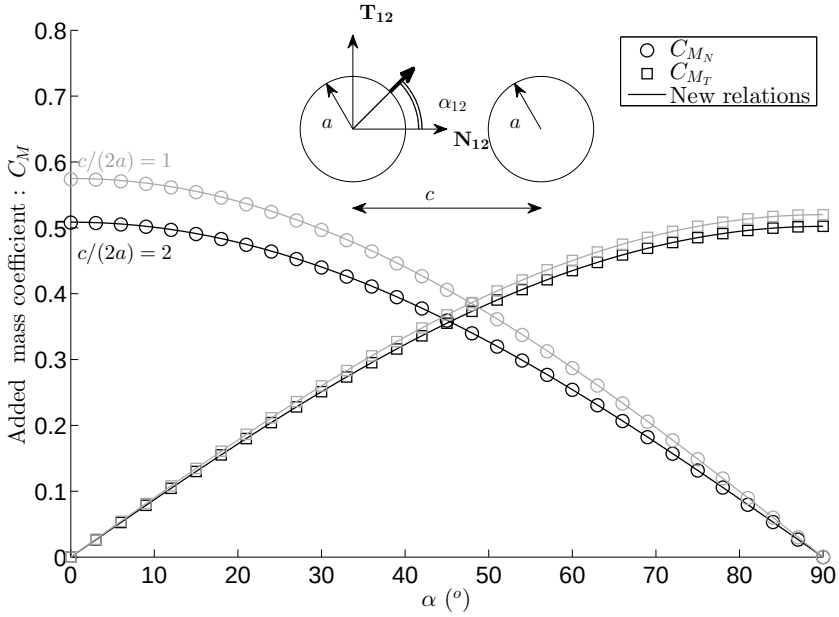

(a) Added Mass (Force on bubble "1").

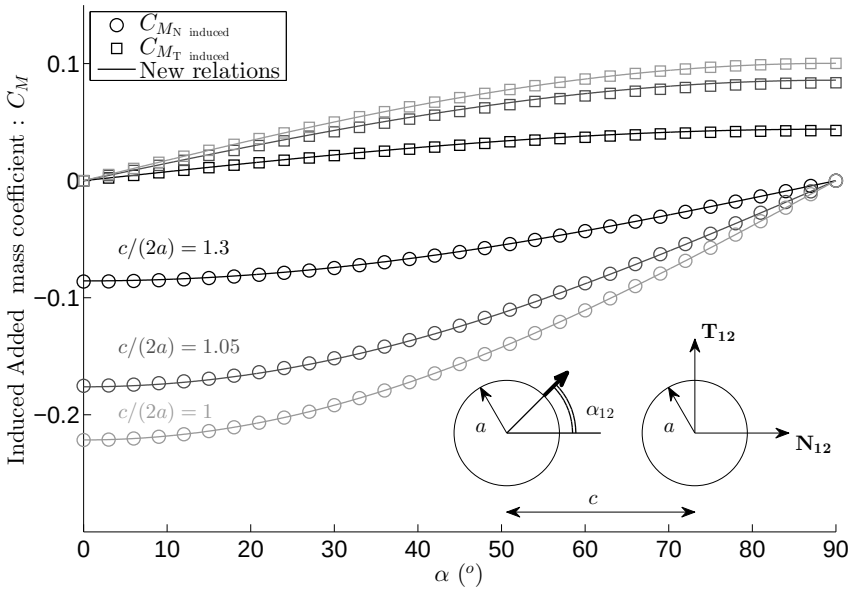

(b) Induced Added Mass (Force on bubble "2").

Figure 3.6 Added mass and induced mass coefficient of two identical bubbles (the accelerating bubble is numbered "1" and the second "2").

$\mathbf{dU_1/dt}$ and $\mathbf{T_{12}}$ are collinear. The angle α_{12} and vectors $\mathbf{N_{12}}$, $\mathbf{T_{12}}$ are shown in Figure 3.6. They can actually be deduced from :

$$\mathbf{N_{12}} = \frac{\mathbf{c_{12}}}{c} \ ,$$

$$\frac{dU_1}{dt}\cos\alpha_{12}\mathbf{N_{12}} = \left(\frac{\mathbf{dU_1}}{\mathbf{dt}} \cdot \mathbf{N_{12}}\right)\mathbf{N_{12}}, \tag{3.40}$$

$$\frac{dU_1}{dt}\sin\alpha_{12}\mathbf{T_{12}} = \frac{\mathbf{dU_1}}{\mathbf{dt}} - \left(\frac{\mathbf{dU_1}}{\mathbf{dt}} \cdot \mathbf{N_{12}}\right)\mathbf{N_{12}}.$$

For $\alpha_{12} = 0$ or π, $\mathbf{T_{12}}$ is not defined. This is without consequence since the added force is along the vector $\mathbf{N_{12}}$ solely.

Ultimately, because the bubble configuration is no longer symmetrical, the force is not aligned with the acceleration. The results are presented in Figure 3.6. The new relations presented are :

- Added Mass : $\mathbf{C_{11}}$

$$C_{M_T} = C_{xx}\sin\alpha,$$

$$C_{M_N} = C_{zz}\cos\alpha,$$

- Induced Added Mass : $\mathbf{C_{12}}$

$$C_{M_T\ \mathrm{ind}} = C_{xx\ \mathrm{ind}}\sin\alpha,$$

$$C_{M_N\ \mathrm{ind}} = C_{zz\ \mathrm{ind}}\cos\alpha.$$

(3.41)

Note that the energy approach is unable to capture this fact, as it only calculates the total force value and not its direction.

3.5 New Formulation of Added mass force for a bubble inside a cloud

In order to simply evaluate the added mass of a bubble inside a cloud of identical bubbles (all bubbles radii are a), we propose the following formulation of the added mass forces acting on the k^{th} bubble inside a cloud of N_b bubbles :

$$\mathbf{F}_k = -\rho\frac{4\pi a^3}{3}\left(\frac{1}{2}\frac{\mathbf{dU_k}}{\mathbf{dt}} + \sum_{\substack{n=1 \\ n\neq k}}^{N_b}\mathbf{f_{kn}} + \mathbf{f_{nk_{\mathrm{induced}}}}\right), \tag{3.42}$$

where

• $\frac{1}{2}\mathbf{dU_k/dt}$ is the added mass of a single bubble in an infinite medium.

• $\mathbf{f_{kn}}$ is the added mass force correction due to the presence of the n^{th} bubble (depending on the acceleration of the k^{th} bubble).

• $\mathbf{f_{nk_{induced}}}$ is the induced added mass force correction due to the n^{th} bubble (depending on the acceleration of the n^{th} bubble).

$\mathbf{f_{kn}}$ and $\mathbf{f_{nk_{induced}}}$ are deduced from equation (3.41) :

$$\begin{aligned}
\mathbf{f_{kn}} &= \left(C_{xx}(c_{kn}) - \frac{1}{2}\right)\left\|\frac{\mathbf{dU_k}}{\mathbf{dt}}\right\|\sin\alpha_{kn}\mathbf{T_{kn}} + \left(C_{zz}(c_{kn}) - \frac{1}{2}\right)\left\|\frac{\mathbf{dU_k}}{\mathbf{dt}}\right\|\cos\alpha_{kn}\mathbf{N_{kn}},\\
\mathbf{f_{nk_{induced}}} &= C_{xx\ \mathrm{ind}}(c_{kn})\left\|\frac{\mathbf{dU_n}}{\mathbf{dt}}\right\|\sin\alpha_{nk}\mathbf{T_{nk}} + C_{zz\ \mathrm{ind}}(c_{kn})\left\|\frac{\mathbf{dU_n}}{\mathbf{dt}}\right\|\cos\alpha_{nk}\mathbf{N_{nk}},\\
&\text{with } c_{kn} = \|\mathbf{c_{kn}}\|
\end{aligned} \tag{3.43}$$

and similarly to equation (3.40),

$$\begin{aligned}
\left\|\frac{\mathbf{dU_k}}{\mathbf{dt}}\right\|\cos\alpha_{kn}\mathbf{N_{kn}} &= \left(\frac{\mathbf{dU_k}}{\mathbf{dt}}\cdot\frac{\mathbf{c_{kn}}}{\|\mathbf{c_{kn}}\|}\right)\frac{\mathbf{c_{kn}}}{\|\mathbf{c_{kn}}\|}\\
&\text{and}\\
\left\|\frac{\mathbf{dU_k}}{\mathbf{dt}}\right\|\sin\alpha_{kn}\mathbf{T_{kn}} &= \frac{\mathbf{dU_k}}{\mathbf{dt}} - \left(\frac{\mathbf{dU_k}}{\mathbf{dt}}\cdot\frac{\mathbf{c_{kn}}}{\|\mathbf{c_{kn}}\|}\right)\frac{\mathbf{c_{kn}}}{\|\mathbf{c_{kn}}\|}.
\end{aligned} \tag{3.44}$$

The Taylor expansions of C_{zz}, $C_{zz\ \mathrm{ind}}$ are presented in tables 3.2 and 3.3. The Taylor expansion of $C_{xx} = C_{yy}$, $C_{xx\ \mathrm{ind}} = C_{yy\ \mathrm{ind}}$ are presented in tables 3.4 and 3.5.

This formulation assumes, that the effect of one bubble to another is not affected by the presence of other bubbles. As underlined in the introduction Cai and Wallis (1994) concluded that it "may not exist a universal definition of added mass for an array of particles that can be applied to all the situations". The formulation proposed above applies for any array of identical spherical particles assuming a potential flow. The following section shows that this formulation accurately predicts the added mass force and is an universal definition of added mass for an array of identical particles.

3.5.1 Added Mass force of one bubble close to a wall

In the case of two identical bubbles accelerating toward one another with identical acceleration magnitude, the plane between the two bubbles is a plane of symmetry which can be replaced by an infinite rigid wall. Milne-Thomson (1968) proposed three formulas in this case and calculated the added mass coefficient with the energy approach using a truncation

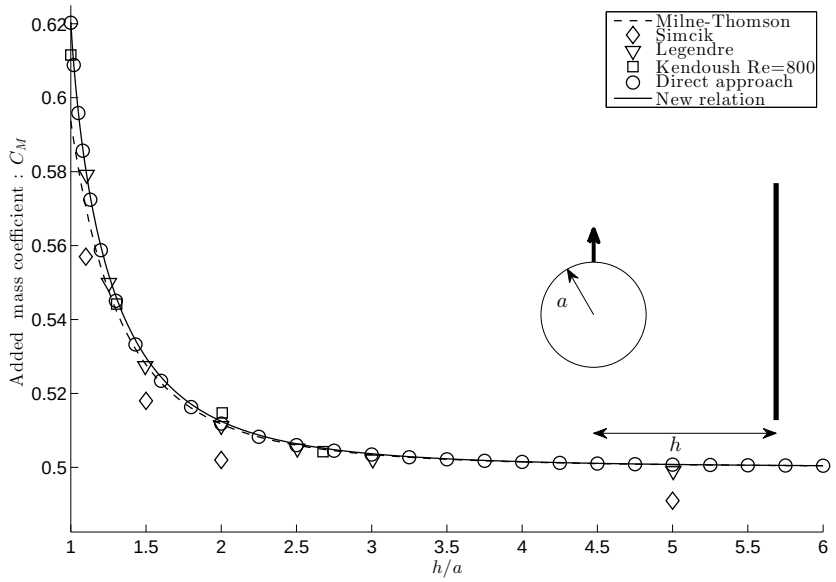

(a) Motion parallel to the wall.

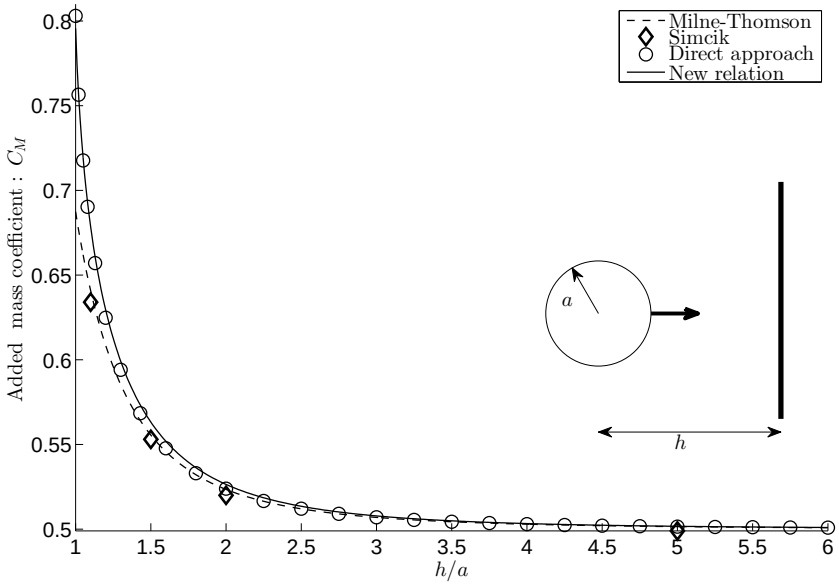

(b) Motion perpendicular to the wall.

Figure 3.7 Added mass of a bubble moving close to the wall.

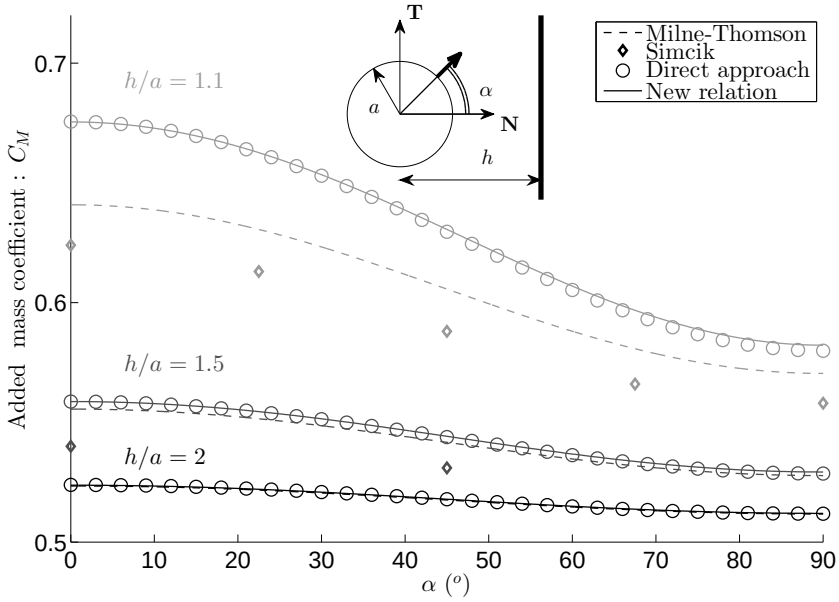

(a) Total added mass for $h/a = 1, 1.2$ and 2.

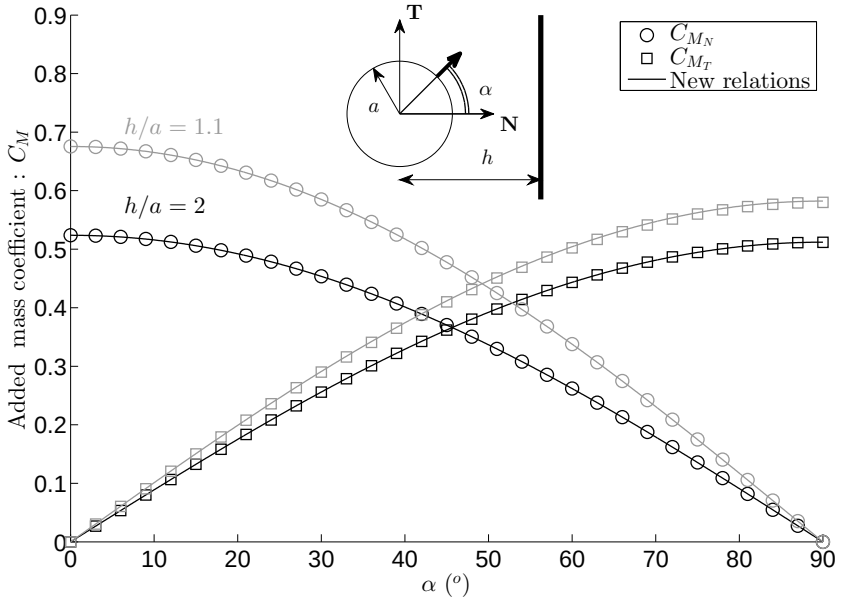

(b) Normal and tangential added mass for $h/a = 1$ and 2.

Figure 3.8 Added mass of a bubble moving close to the wall with an angle.

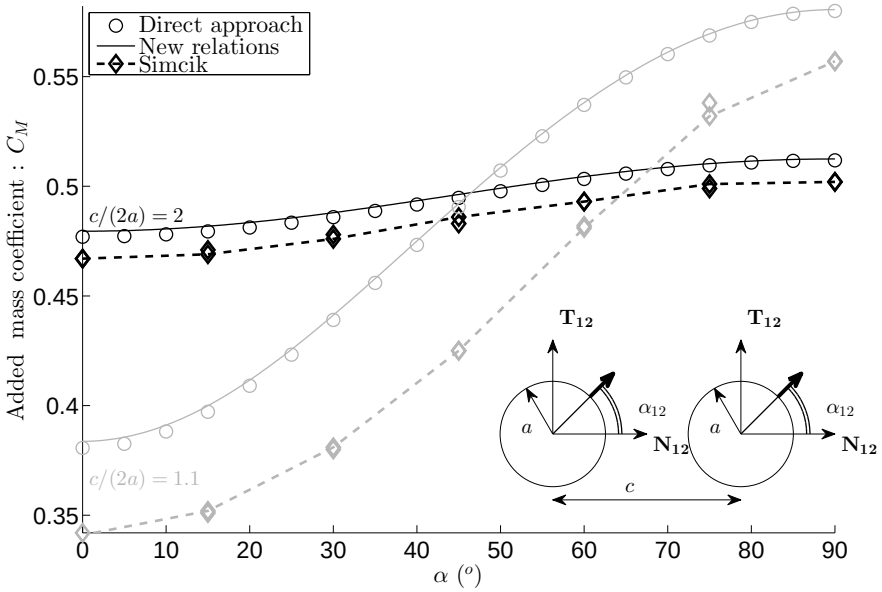

Figure 3.9 Added mass of two bubbles with a parallel acceleration.

of Legendre polynomials up to $L = 1$ for both the integration of the kinetic energy and the velocity potential calculation. As shown in Figure 3.2, the energy approach using a truncation of Legendre polynomials up to $L = 1$ is very close to Milne Thomson's formula. The difference is explained by the fact that the integration of the kinetic energy is done numerically without any truncation in our case. As shown in Figure 3.7(a) and 3.7(b), Milne-Thomson's formulas (3.45) are very good approximations up to a bubble-wall distance of one bubble diameter. For smaller distances, Milne Thomson's approximation underestimates the added mass force. Results compare well with other numerical results [Legendre *et al.* (2003); Simcik *et al.* (2008)] or empirical results [Kendoush *et al.* (2007)].

- Parallel motion

$$C_M = \frac{1}{2}\left(1 + \frac{3}{16}\left(\frac{a}{h}\right)^3\right),$$

- Perpendicular motion

$$C_M = \frac{1}{2}\left(1 + \frac{3}{8}\left(\frac{a}{h}\right)^3\right), \tag{3.45}$$

- Angle motion

$$C_M = \frac{1}{2}\left(1 + \frac{3}{16}\left(\frac{a}{h}\right)^3 (1 + \cos^2\alpha)\right).$$

With $2h = c$, for these three cases, equation (3.42) leads to :

- Parallel motion

$$C_M = \frac{1}{2}\left[1 + \frac{3}{16}\left(\frac{a}{h}\right)^3 + \frac{3}{256}\left(\frac{a}{h}\right)^6 + \frac{3}{256}\left(\frac{a}{h}\right)^8 + \frac{3}{4096}\left(\frac{a}{h}\right)^9 + \sum_{n=10}^{\infty}\left(e_n + e_n^{ind}\right)\left(\frac{a}{h}\right)^n\right],$$

- Perpendicular motion

$$C_M = \frac{1}{2}\left[1 + \frac{3}{8}\left(\frac{a}{h}\right)^3 + \frac{3}{64}\left(\frac{a}{h}\right)^6 + \frac{9}{256}\left(\frac{a}{h}\right)^8 + \frac{3}{512}\left(\frac{a}{h}\right)^9 + \sum_{n=10}^{\infty}\left(d_n - d_n^{ind}\right)\left(\frac{a}{h}\right)^n\right], \tag{3.46}$$

- Angle motion

$$C_{M_N} = \frac{1}{2}\left[1 + \frac{3}{8}\left(\frac{a}{h}\right)^3 + \frac{3}{64}\left(\frac{a}{h}\right)^6 + \frac{9}{256}\left(\frac{a}{h}\right)^8 + \sum_{n=9}^{\infty}\left(d_n - d_n^{ind}\right)\left(\frac{a}{h}\right)^n\right]\cos\alpha,$$
$$C_{M_T} = \frac{1}{2}\left[1 + \frac{3}{16}\left(\frac{a}{h}\right)^3 + \frac{3}{256}\left(\frac{a}{h}\right)^6 + \frac{3}{256}\left(\frac{a}{h}\right)^8 + \sum_{n=9}^{\infty}\left(e_n + e_n^{ind}\right)\left(\frac{a}{h}\right)^n\right]\sin\alpha.$$

These equations were obtained by summing the added mass and induced added mass of the mirror bubble. These equations are equal to those obtained by Kok (1993). This result is in fact the sum of the added mass and induced added mass of the mirror bubble. In case of a bubble acceleration toward the wall, as Spence's function has an exact solution for $h/a = 1$, ($\sum 1/k^2 = \pi^2/6$), using values from table 3.2,3.3 and assuming inequalities (3.38) remains true when $n \to \infty$, we can deduce $C_M(h/a = 1) = 0.8033 \pm 0.0004$.

Similarly to the case of two bubbles with an angle, because the bubble configuration is no longer symmetrical, the force is not aligned with acceleration. Figure 3.8(b) shows that for an angle close to 50^o at $h/a = 1.1$ the force is at an angle of 45^o ($C_{M_N} = C_{M_T}$). As previously underlined by Milne-Thomson (1968), the added mass increases has a consequence : as bubbles come closer to each other or closer to a wall, added mass force act as a repelling force. Indeed, if a bubble is moving toward a wall or another bubble without extraneous forces, the total

energy must remain constant. Since its added mass increases, its velocity must decrease. The bubble is therefore repelled from the wall and from other bubbles. This phenomenon minimizes the occurrence of impact between bubbles or between bubbles and walls. However, this conclusion needs to be refined in the case of in line bubbles or accelerating bubbles columns as shown in the next section.

3.5.2 Added Mass of two accelerating bubbles

In this section, the case of two identical bubbles having identical accelerations is considered. The acceleration makes an angle α with the line joining the two centers. $\alpha = 90^o$ corresponds to the parallel motion of one bubble close to a wall. As previously noted, the added mass force is not collinear with the acceleration, but in order to compare our results with those of other authors [Simcik *et al.* (2008); Kendoush *et al.* (2007)], Figure 3.9 presents only the added mass coefficient corresponding to the total force. In agreement with the conclusion of Kendoush *et al.* (2007), two identical bubbles accelerating side by side lead to $C_M > 0.5$. However, two identical bubbles accelerating in line lead to $C_M < 0.5$. In both cases, as the distance between bubbles increases, C_M approaches monotonically to the value of 0.5.

3.5.3 Added Mass of a bubble column, a bubble row and bubble plane

This section explores the case of N_b aligned bubbles accelerating in the same direction. Figure 3.10 (a) and (b) present respectively the added mass coefficient of the central bubble in an accelerating bubble column (in-line) and in an accelerating bubble row (side by side). *Note : In case of $N_b = 2$, the central bubble has no meaning. However both bubbles have the same added masses.* The simple formula (3.42) assumes, that the effect of one bubble to another is not affected by the presence of other bubbles. It leads to a very good approximation within ± 0.03 of the total value of the added mass coefficient. As expected and already shown by previous authors [Simcik *et al.* (2008); Kendoush *et al.* (2007)], when bubbles located in-line with the acceleration (bubble column) come closer, the added mass force decreases. However, when bubbles located perpendicularly with the acceleration (bubble row) come closer, the added mass force increases. This fact explains the main difficulty to propose a valid added mass coefficient when the location of the bubbles are not known. We will explore more carefully this fact in the next section dedicated to clouds of bubbles.

The spatial distribution of bubbles is usually determined by dynamic simulations. The case of buoyant rise of bubbles by dynamic simulations was also examined by Sangani and Didwania (1993) and Smereka (1993). The dynamic simulations of bubbly flow by Sangani and Didwania (1993) show that bubbles tend to position themselves in planes. Consequently,

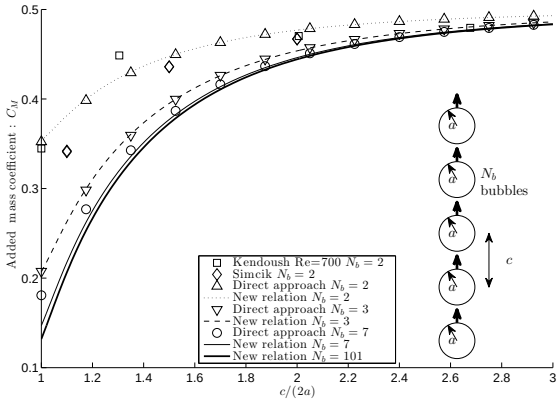

(a) Accelerating bubble column.

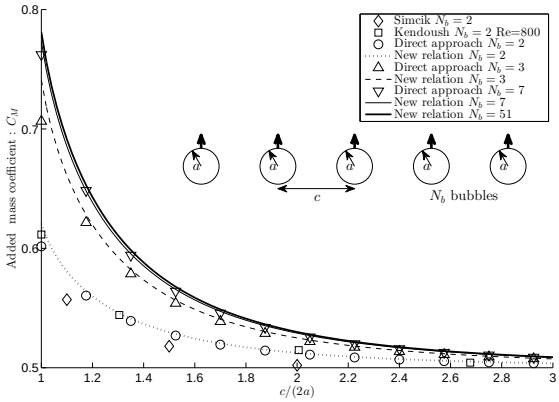

(b) Accelerating bubble row.

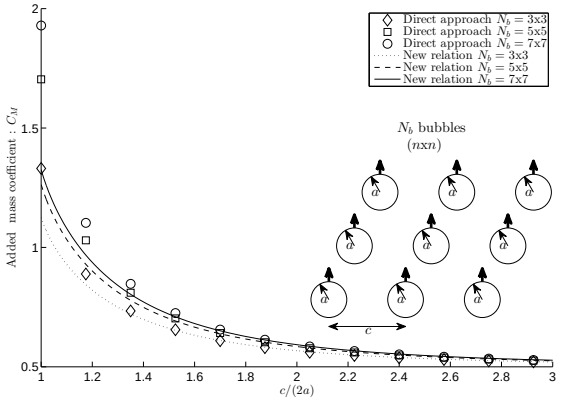

(c) Accelerating bubble plane.

Figure 3.10 Added mass of the central bubble in an accelerating bubble line or plane.

they observed an increase of their added mass up to $C_M = 1.5$ which is the typical value we obtain for close bubbles aggregates in a planes, see Figure 3.10 (c). Smereka (1993) concludes also that the most stable bubble cloud corresponds to higher added mass. The tendency for the formation of these plane clusters is explained by potential interactions among bubbles. Pairs of bubbles aligned within about 55^o to the direction of mean bubble motion are repelled by each other, while those aligned in a plane perpendicular to that are attracted toward each other [Biesheuvel and Van Wijngaarden (1982)].

This should lead to an increased probability of finding bubble horizontally aligned. However, all these simulations were purely irrotational for all forces (including drag). The authors conclude that random vorticity is probably the mechanism that prevents the bubbles to aggregate. In other word, the tendency to form plane aggregates decreases as velocity fluctuations in the bubbly flows increase. As two-phase flow is known to be highly turbulent, random configuration of bubbles is more often encountered.

3.6 Added Mass of a bubble inside a cloud

In order to propose an effective model for bubbly flows, it is crucial to understand how the added mass force depends on void fraction and bubbles configuration. For the sake of conciseness, we focus on identical bubbles. Some results have been obtained for simple geometric configurations. Zuber (1964) proposes to use the classical result of a spherical body inside a spherical domain [cf. Milne-Thomson (1968)]. Noting void fraction as the ratio of the spherical body over the volume of the spherical domain leads to :

$$C_M = \frac{1}{2}\frac{1+2\varepsilon}{1-\varepsilon} \sim \frac{1}{2} + \frac{3}{2}\varepsilon. \tag{3.47}$$

Other results have been obtained and usually take the form :

$$C_M = \frac{1}{2} + \frac{k}{2}\varepsilon + o(\varepsilon^2), \tag{3.48}$$

with k taking the value of 2.78 [Van Wijngaarden (1976)], $1 + (1 - 2/Z)$ [Van Wijngaarden (1991)] 3.26 [Niemann and Laurien (1991)], 3.32 [Biesheuvel and Spoelstra (1989)], or 4.2 [Mokeyev (1977)] with Z the sphericity correction factor which takes into account the effect of ellipticity of the bubble. All these results lead to an increase of the added mass with the void fraction. However, in some cases such as bubble columns, the added mass force could decrease as bubbles come closer. Wallis (1989) proposed to allow the motion of the spherical domain rather than to fix it [Zuber (1964) assumption]. This boundary condition is called an

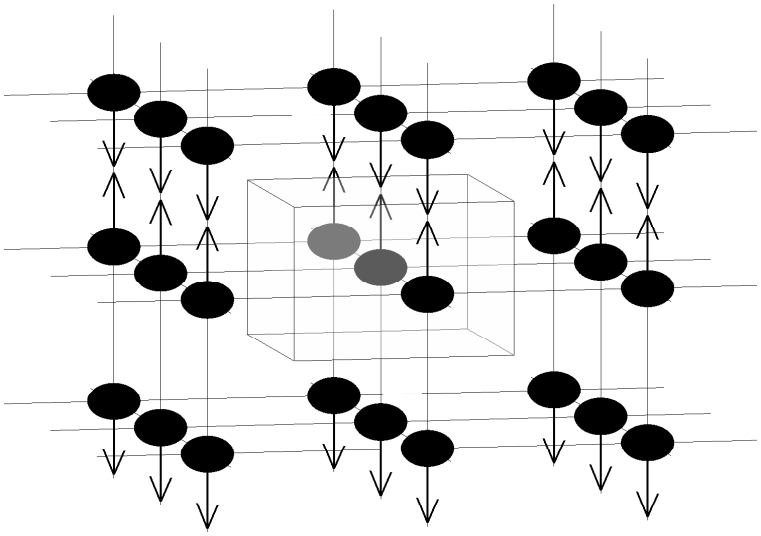

(a) Array of bubble equivalent to a bubble in a box.

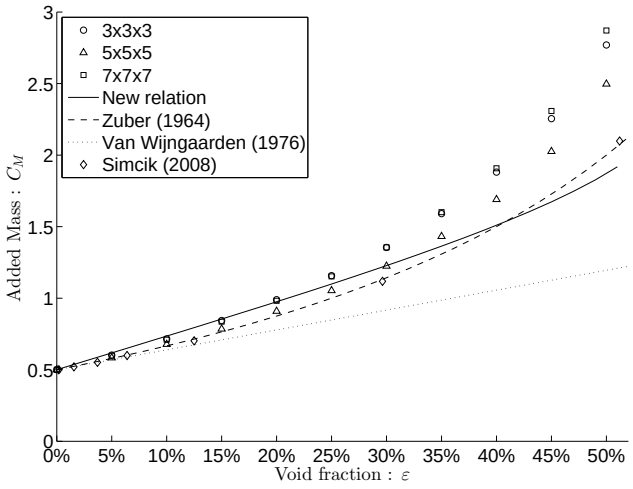

(b) Added mass.

Figure 3.11 Added mass of a central bubble in a cubic array (bubble in a box).

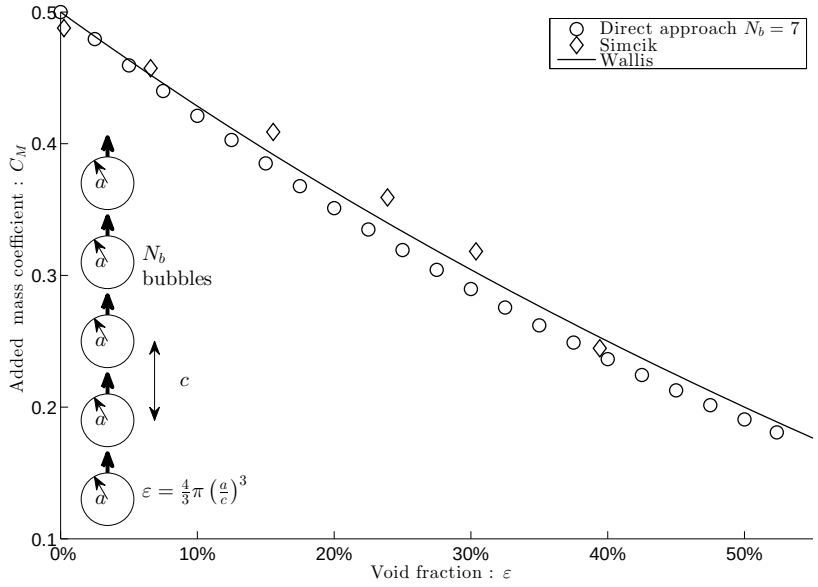

Figure 3.12 Added mass of a central bubble in a 7 bubbles column compared to CFD result of a bubble in a periodic box with pressure release by Simcik *et al.* (2008) and Wallis correlation of a spherical cell with "ideally compliant pressure release surface".

"ideally compliant pressure release surface". Wallis (1989) obtained the following correlation :

$$C_M = \frac{1}{2}\frac{2-2\varepsilon}{2+\varepsilon}. \tag{3.49}$$

Cai and Wallis (1994) proposed a more general description of the added mass coefficient :

$$C_M = \frac{1}{2}\frac{(2-2\varepsilon)+\lambda(1+2\varepsilon)}{(2+\varepsilon)+\lambda(1-\varepsilon)}, \tag{3.50}$$

with the unknown parameter λ related to the external impedance of the cell around the bubbles. $\lambda = 0$ and $\lambda \to \infty$ correspond respectively to the two extreme cases. The case suggested by Wallis (1989) corresponds to the lower bound while the one suggested by Zuber (1964) corresponds to an upper bound of the added mass. The external impedance would depend on the boundary conditions of the cell related to the bubble's configuration. Formulation (3.42) proposed in this paper can be applied for any array of identical spherical particles assuming a potential flow. It solves the problem of the unknown effect of bubbles configuration. We will show in this section that the proposed model is an universal definition of added mass for an array of identical particles.

The simple case considered by Zuber (1964) (a spherical body in a spherical domain)

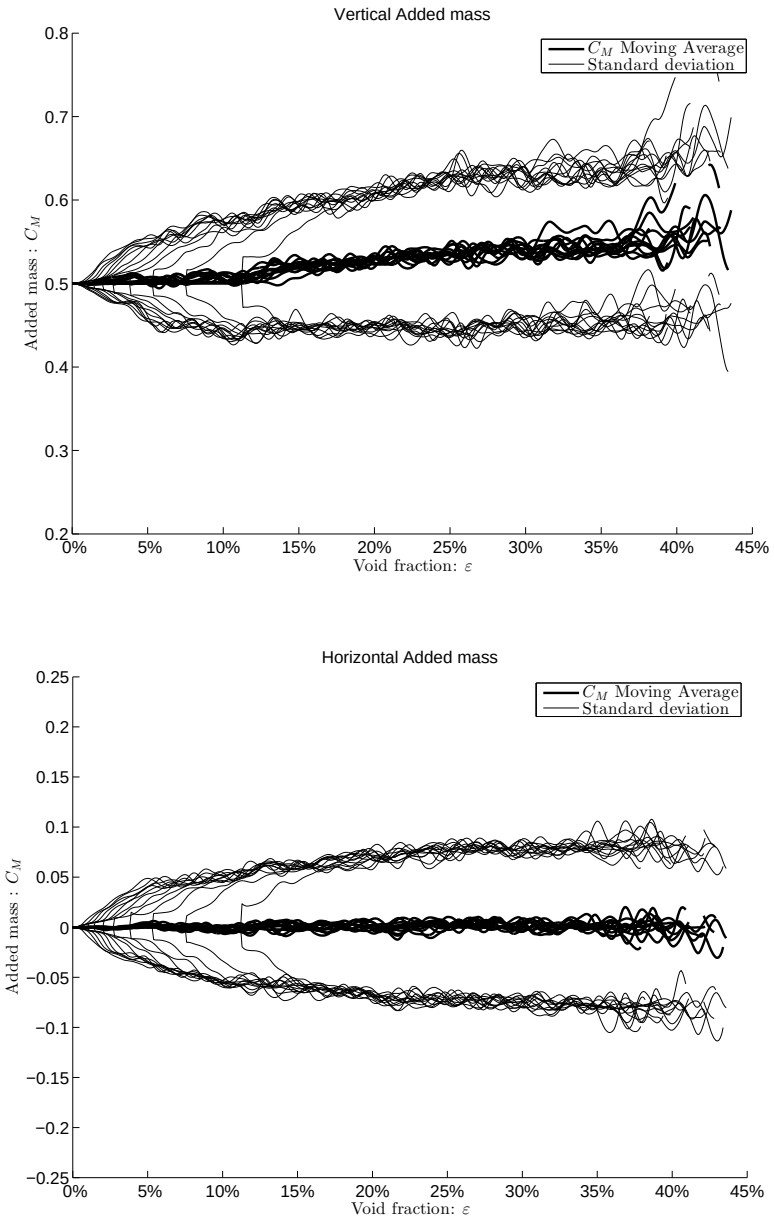

Figure 3.13 Added mass of the central bubble in a random cloud vs. void fraction for different size of control volume.

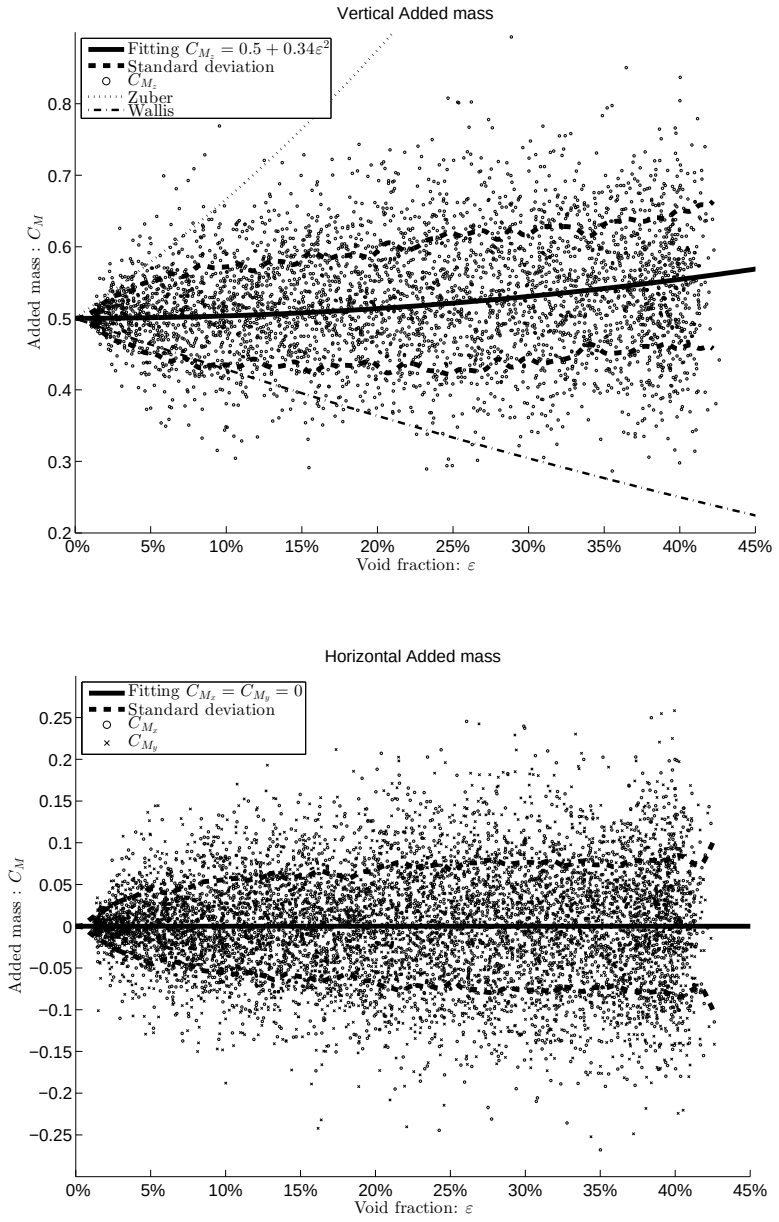

Figure 3.14 Added mass of the central bubble in a random cloud vs. void fraction for control volume $R/a = 5$ and proposed fitting (3.52).

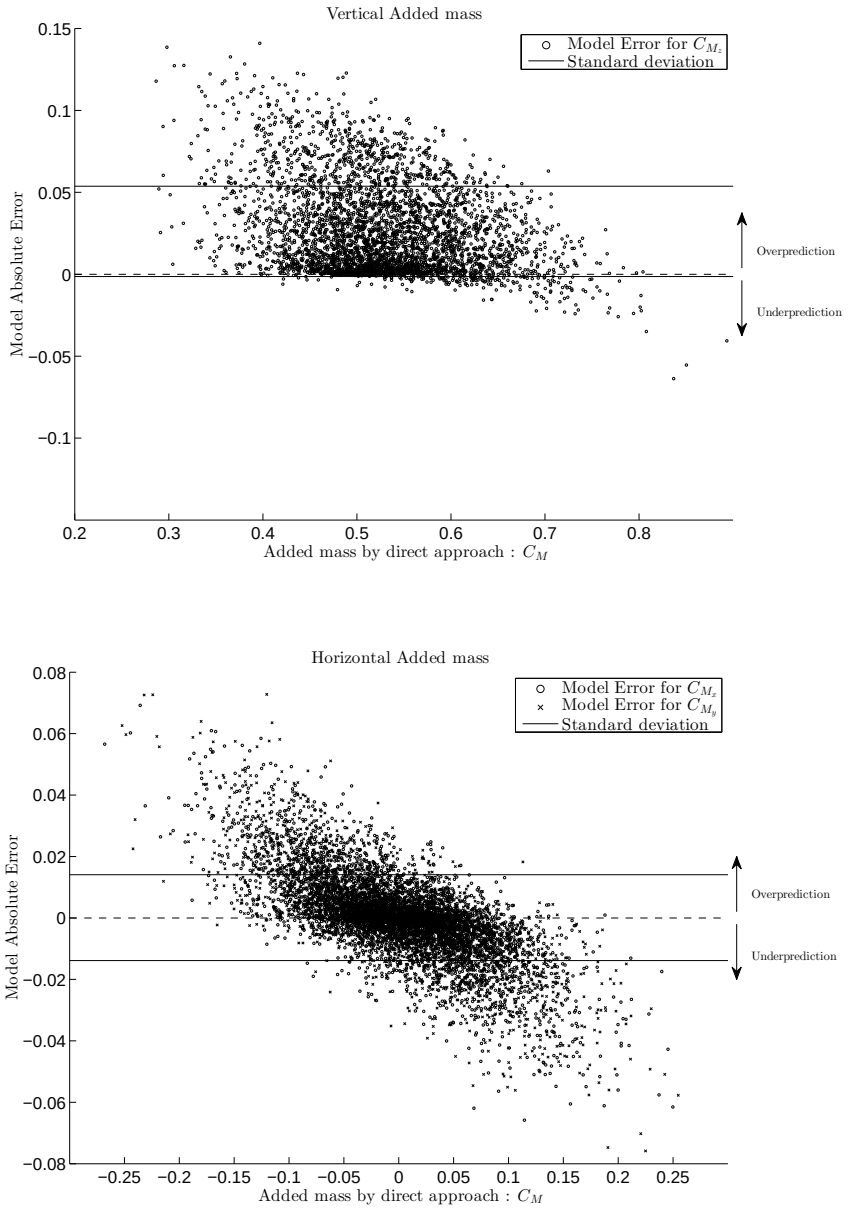

Figure 3.15 Added mass of the central bubble in a random cloud : comparison between direct approach and new formula (3.42).

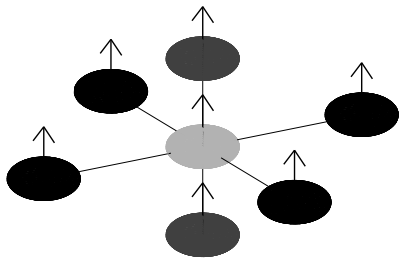

Figure 3.16 Bubble inside a cubic lattice with only the six closest bubbles.

yields an exact solution implying regular solid harmonics (3.3). Our approach relies only on irregular solid harmonics because regular solid harmonics diverge to infinity. Consequently, we cannot obtain this exact solution. However, this simple case can be estimated if bubbles are located in a cubic lattice with alternatively one plane accelerating upward and one plane accelerating downward. Figure 3.11(a) presents a 3x3 array of bubbles, where arrows stand for bubbles accelerations. For an infinite array of this kind, the cube around the central bubble is surrounded by symmetry planes which can be considered as a slip wall condition. This leads to the case of one bubble in a cubic box. Void fraction can then be defined as :

$$\varepsilon = \frac{4}{3}\pi\left(\frac{a}{c}\right)^3, \tag{3.51}$$

where c is the center-to-center distance equal to the width of the cubic box. This case has been numerically solved by Simcik *et al.* (2008). This configuration is unrealistic of a real cloud of bubbles as all bubbles will have roughly the same direction of acceleration. As underlined by Cai and Wallis (1994), this case corresponds more to an upper bound for the added mass coefficient. Results are presented in Figure 3.11(b). Up to 30% void fraction, all models are in good agreement : the new relation (3.42), the direct calculation with a cubic array of 3x3x3, 5x5x5 and 7x7x7 bubbles, Zuber (1964) formula (3.47), Van Wijngaarden (1976) formula (3.48) and Simcik *et al.* (2008) CFD results.

The correlation proposed by Wallis (1989) (3.49) corresponds to an "ideally compliant pressure release surface". This condition seems to correspond to the case of a bubble column. Choosing the same definition for void fraction (3.51), Wallis's correlation and direct calculation with seven bubbles are in good agreement as illustrated by Figure 3.12.

As the present model allows an added mass determination in a very short amount of computational time, we generate a random cloud of identical bubbles (same sizes and accelerations) around a central bubble. The radius of the sphere, where all bubble centers are

located, is $R = 6a$ (a is the radius of all bubbles). The number of bubbles varies from 1 to 70. For each number of bubbles, up to 70 different random clouds of bubbles are generated. Void fraction is defined by the volume occupied by bubbles over the volume of a control volume. The control volume is a sphere of radius R set between $R = 2a$ and $R = 5a$. Consequently, as we have at least one central bubble, the minimum void fraction is $\varepsilon = (a/R)^3$. For a control volume radius $R = 2a$, we have $\varepsilon_{min} = 12.5\%$ and for a control volume radius $R = 5a$, we have $\varepsilon_{min} = 0.8\%$.

All bubbles accelerate along the z-axis. The added mass coefficient for this direction is around 0.5 with a slight increase with void fraction, whereas the added mass coefficients for x and y directions are close to zero. Figure 3.13 shows added mass coefficient results, moving average and standard deviation. Moving average and standard deviation are calculated using a Hanning window. The different curves correspond to different sizes of control volume from $R = 2a$ up to $R = 5a$ in order to calculate the void fraction. We propose two correlations for the added mass :

$$C_{M_z} = \frac{1}{2} + 0.34\varepsilon^2,$$
$$C_{M_x} = C_{M_y} = 0, \tag{3.52}$$

where the z-axis is the axis of the cloud acceleration. All the results obtained with a control volume with $R = 5a$ and the proposed correlations are presented in Figure 3.14. These correlations have a standard deviation increasing with void fraction up to a typical value of 0.1. This standard deviation comes from different bubble configurations having the same void fraction. The added mass force also possesses a component perpendicular to the acceleration of the cloud attributed to the asymmetry of the cloud. This effect could be interpreted as a "random" force due to random bubble configuration. Indeed, these effects is due to the fact that the total added mass force decreases when bubbles are located in-line with the acceleration but increases when located perpendicularly as shown in section 3.5.3.

Figure 3.14 also presents the correlation proposed by Zuber (1964) (3.47). As expected, this correlation is close to a maximum value of the added mass. The correlation proposed by Wallis (1989) (3.50 with $\lambda = 0$) is also shown. As expected, this correlation is close to a minimum value of the added mass. The correlation proposed by Wallis (1989) corresponds to a boundary condition called an "ideally compliant pressure release surface". As shown by the result, even for a low void fraction of 10%, the added mass coefficient can vary from 0.3 to 0.8. Consequently, the added mass of a bubble can be multiplied by almost a factor of 3 with a change in the location of surrounding bubbles.

Unlike previous studies, we do not have any dependence with ε but only with ε^2. This

fact can be easily understood if we place bubbles inside a cubic lattice and only consider the six closest bubbles, see Figure 3.16 [two located vertically (dark gray) four located laterally (black)]. All bubbles accelerate upward and at the same distance c of the central bubble (light gray). The added mass force on the central bubble deduced from (3.42) is :

$$\mathbf{F} = -\rho\frac{4\pi a^3}{3}\left(\frac{1}{2}\frac{\mathbf{dU_b}}{\mathbf{dt}} + 2\left(\mathbf{f}_{\text{ver.}} + \mathbf{f}_{\text{ver}_{\cdot\text{induced}}}\right) + 4\left(\mathbf{f}_{\text{lat.}} + \mathbf{f}_{\text{lat}_{\cdot\text{induced}}}\right)\right). \tag{3.53}$$

$\mathbf{f}_{\text{ver.}}$ and $\mathbf{f}_{\text{ver}_{\cdot\text{induced}}}$ represent respectively the added mass correction and induced added mass due to the two bubbles located vertically (dark gray in Figure 3.16) :

$$\begin{aligned}\mathbf{f}_{\text{ver.}} &= \left(\frac{3}{2}\left(\frac{a}{c}\right)^6 + \frac{9}{2}\left(\frac{a}{c}\right)^8 + \ldots\right)\frac{\mathbf{dU_b}}{\mathbf{dt}},\\ \mathbf{f}_{\text{ver}_{\cdot\text{induced}}} &= -\left(\frac{3}{2}\left(\frac{a}{c}\right)^3 + \frac{3}{2}\left(\frac{a}{c}\right)^9 + \ldots\right)\frac{\mathbf{dU_b}}{\mathbf{dt}}.\end{aligned} \tag{3.54}$$

$\mathbf{f}_{\text{lat.}}$ and $\mathbf{f}_{\text{lat}_{\cdot\text{induced}}}$ represent respectively the added mass correction and induced added mass of the four lateral bubbles (black in Figure 3.16) :

$$\begin{aligned}\mathbf{f}_{\text{lat.}} &= \left(\frac{3}{8}\left(\frac{a}{c}\right)^6 + \frac{3}{2}\left(\frac{a}{c}\right)^8 + \ldots\right)\frac{\mathbf{dU_b}}{\mathbf{dt}},\\ \mathbf{f}_{\text{lat}_{\cdot\text{induced}}} &= \left(\frac{3}{4}\left(\frac{a}{c}\right)^3 + \frac{3}{16}\left(\frac{a}{c}\right)^9 + \ldots\right)\frac{\mathbf{dU_b}}{\mathbf{dt}}.\end{aligned} \tag{3.55}$$

With $\varepsilon = 4\pi/3(a/c)^3$, this leads to :

$$\mathbf{F} = -\rho\frac{4\pi a^3}{3}\left(\frac{1}{2} + \frac{9}{2}\frac{3}{4\pi}\varepsilon^2 + O(\varepsilon^{8/3})\right)\frac{\mathbf{dU_b}}{\mathbf{dt}} \simeq -\rho\frac{4\pi a^3}{3}\left(\frac{1}{2} + \varepsilon^2 + O(\varepsilon^{8/3})\right)\frac{\mathbf{dU_b}}{\mathbf{dt}}. \tag{3.56}$$

Indeed, at first order, the four lateral bubbles increase the added mass coefficient by a factor of $4 \times 3/4$ while the two bubbles located vertically decrease the added mass coefficient by a factor of $2\times3/2$ leading to no dependence with $0(\varepsilon)$. Equation (3.56) is close to the correlation for a random bubble configuration (3.52).

In the case of a Lagrangian approach where the location and acceleration of each bubble is known we can use new formula (3.42). The absolute error of this model is presented in Figure 3.15. The absolute error is defined as the difference between the added mass coefficient calculated using the new formula (3.42) and the one calculated with the direct approach. This model allows to take into account, more precisely, the effect of bubble distribution on the added mass. Consequently the model increases the accuracy in the prediction of bubble cloud dynamics. The model tends to over-predict the added mass in the acceleration direction. The average absolute error plus or minus standard deviation (−0.014 and +0.054) are shown in the

Figure. This is an improvement compared to the Euler modeling with a standard deviation of 0.1 (see Figure 3.14).

For the added mass coefficient in the direction perpendicular to the cloud acceleration the average absolute error plus or minus standard deviation is $-0.014, +0.014$. The model tends to under-predict the magnitude of this lateral force. Indeed the new formula (3.42) under-predicts positive values (ex : Model : 0.16 Direct approach : 0.2) and over-predicts negative values (ex : Model : -0.16 Direct approach : -0.2). This model is an important improvement compared to the Euler modeling with a standard deviation of 0.05 (see Figure 3.14). Moreover, it allows to model the "random" force, including its components perpendicular to the acceleration of the bubble.

3.7 Conclusion

The paper presents a relation for the added mass coefficient of spherical bubbles depending on void fraction obtained by a semi-analytical method using solid harmonics to solve 3D potential flow around bubbles. Several configurations were calculated for different numbers of particles and spatial configurations. The simple formulas are suitable for further use, particularly as an added mass model in an averaged equations for multiphase flow in the case of Euler-Lagrange modeling. The added mass force on the k^{th} bubble inside a cloud of N_b identical bubbles is :

$$\mathbf{F_k} = -\rho \frac{4\pi a^3}{3} \left(\frac{1}{2} \frac{\mathbf{dU_k}}{\mathbf{dt}} + \sum_{\substack{n=1 \\ n \neq k}}^{N_b} \mathbf{f_{kn}} + \mathbf{f_{nk}}_{\text{ ind}} \right), \tag{3.57}$$

with the first term, $\mathbf{f_{kn}}$ and $\mathbf{f_{nk}}_{\text{ ind}}$ representing respectively the added mass of a single bubble, the added mass correction and induced added mass on the k^{th} bubble due to the presence of the n^{th} bubble. Details are given in the section 3.5.

For an Euler-Euler model, assuming enough turbulence to ensure a random distribution, a value of $C_M = 0.5 + 0.34\varepsilon^2$ is the most suitable. The standard deviation linearly increases with the void fraction. This effect could be interpreted as a "random" force induced by the randomness of the bubble configuration. This added mass force has also a component perpendicular to the acceleration of the cloud. These effects will be difficult to model with an Euler-Euler model.

Bubbles located side by side lead to an added mass increase as they come closer with $C_M > 0.5$. This corresponds to a repelling force. However, bubbles located in-line lead to an added mass decrease as they come closer with $C_M < 0.5$. This corresponds to an attractive force.

The presence of a wall leads to increase added mass as the bubbles come closer to the

wall with $C_M > 0.5$. This corresponds to a repelling force.

The future of this work is to explore the effect of random size of bubbles and bubble clouds close to a wall.

3.8 Appendices

3.8.A Potential Computation

To numerically solve equation (3.18) rewritten below, we will limit the sum up to L. $\forall k \in \mathbb{N}, k \leq N_b, \forall \lambda \in \mathbb{N}, \forall \mu \in \mathbb{Z}, |\mu| \leq \lambda$

$$\sum_{\substack{n=1 \\ n\neq k}}^{N_b} \left(\sum_{\ell=0}^{\infty} \sum_{m=-\ell}^{\ell} g_{\ell,n}^{m} (-1)^{\frac{\mu+|\mu|}{2}} D_{\ell,\lambda}^{m,\mu} \lambda a_k^{\lambda-1} \tilde{S}_{\lambda+\ell}^{m-\mu}(\mathbf{c_{nk}}) \right) - g_{\lambda,k}^{\mu} (-1)^{\frac{|\mu|+\mu}{2}} \frac{\lambda+1}{a_k^{\lambda+2}} = \delta_{\lambda,1} L_k^{\mu}$$

with :

$$L_k^{\mu} = \begin{cases} -\dfrac{\sqrt{2}}{2}(\dot{x}_k + \imath \dot{y}_k) & \text{if } \mu = -1 \\ \dot{z}_k & \text{if } \mu = 0 \\ -\dfrac{\sqrt{2}}{2}(\dot{x}_k - \imath \dot{y}_k) & \text{if } \mu = 1 \end{cases} \tag{3.58}$$

We can note that this equation leads to $\forall k \in \mathbb{N}, g_{0,k}^{0} = 0$. Equation (3.58), with the sum limit up to L can then be rewritten as :

$\forall k \in \mathbb{N}, k \leq N_b, \forall \lambda \in \mathbb{N}^*, \lambda \leq L, \forall \mu \in \mathbb{Z}, |\mu| \leq \lambda$

$$\sum_{\substack{n=1 \\ n\neq k}}^{N_b} \left(\sum_{\ell=1}^{L} \sum_{m=-\ell}^{\ell} g_{\ell,n}^{m} D_{\ell,\lambda}^{m,\mu} \frac{\lambda a_k^{2\lambda+1}}{\lambda+1} \tilde{S}_{\lambda+\ell}^{m-\mu}(\mathbf{c_{nk}}) \right) - g_{\lambda,k}^{\mu} = \delta_{\lambda,1} \Lambda_k^{\mu}$$

with :

$$\Lambda_k^{\mu} = \begin{cases} \dfrac{\sqrt{2} a_k^3}{4}(\dot{x}_k + \imath \dot{y}_k) & \text{if } \mu = -1 \\ -\dfrac{a_k^3}{2} \dot{z}_k & \text{if } \mu = 0 \\ -\dfrac{\sqrt{2} a_k^3}{4}(\dot{x}_k - \imath \dot{y}_k) & \text{if } \mu = 1 \end{cases} \tag{3.59}$$

Noting

$$g_{\ell,n}^{m} = x_j = x_{(n-1)L(L+2)+l^2+l+m}, \tag{3.60}$$

equation (3.59) is reduced to N equations and can be written as :

$$\begin{bmatrix} b_{11} & \cdots & b_{1N} \\ \vdots & \ddots & \vdots \\ b_{N1} & \cdots & b_{NN} \end{bmatrix} \underbrace{\begin{pmatrix} x_1 \\ \vdots \\ x_N \end{pmatrix}}_{g^m_{\ell,n}} = \underbrace{\begin{pmatrix} h_1 \\ \vdots \\ h_N \end{pmatrix}}_{\Lambda^\mu_\lambda(\mathbf{c_{nk}})}, \tag{3.61}$$

with $N = N_b L(L+2)$ and

$$\begin{aligned}
&\forall n,k,\ell,\lambda \in \mathbb{N}^2, n \le N_b, k \le N_b, \ell \le L, \lambda \le L,\\
&\forall m,\mu \in \mathbb{Z}^2 |m| \le \ell, |\mu| \le \lambda\\
&i = (n-1)L(L+2) + \lambda^2 + \lambda + \mu\\
&j = (k-1)L(L+2) + l^2 + l + m\\
&b_{ij} = \begin{cases} -D^{m,\mu}_{\ell,\lambda} \dfrac{\lambda a_k^{2\lambda+1}}{\lambda+1} \tilde{S}^{m-\mu}_{\lambda+\ell}(\mathbf{c_{nk}}) & \text{,if } n \ne k \\ 1 & \text{,if } i = j \\ 0 & \text{, Otherwise} \end{cases}
\end{aligned} \tag{3.62}$$

$$h_j = \delta_{\lambda,1} \begin{cases} \dfrac{\sqrt{2}a_k^3}{4}(\dot{x}_k + \imath \dot{y}_k) & \text{if } \mu = -1 \\ -\dfrac{a_k^3}{2}\dot{z}_k & \text{if } \mu = 0 \\ -\dfrac{\sqrt{2}a_k^3}{4}(\dot{x}_k - \imath \dot{y}_k) & \text{if } \mu = 1 \end{cases}$$

$D^{m,\mu}_{\ell,\lambda}$ is evaluated through Pascal's rules :

$$\binom{n}{k} = \binom{n-1}{k-1} + \binom{n-1}{k} \tag{3.63}$$

This allows to reach theoretically $L = 1035$ for 64 bit real number definition, but for most of the cases we reach zero machine around $L = 50$.

3.8.B Added Mass Computation

According to equation (3.32), we can define the added mass coefficients of the k^{th} bubble as :

$$\begin{pmatrix} C_{\bullet x} \\ C_{\bullet y} \\ C_{\bullet z} \end{pmatrix}_{nk} = \sum_{\ell=0}^{\infty}\sum_{m=-\ell}^{\ell}\sum_{\substack{n=1\\n\neq k}}^{N_b}\frac{g_{\ell,n}^{m}}{\sqrt{2}}\begin{pmatrix} D_{\ell,1}^{m,-1}\tilde{S}_{\ell+1}^{m+1}(\mathbf{c_{nk}}) - D_{\ell,1}^{m,1}\tilde{S}_{\ell+1}^{m-1}(\mathbf{c_{nk}}) \\ -\imath(D_{\ell,1}^{m,-1}\tilde{S}_{\ell+1}^{m+1}(\mathbf{c_{nk}}) + D_{\ell,1}^{m,1}\tilde{S}_{\ell+1}^{m-1}(\mathbf{c_{nk}})) \\ -\sqrt{2}D_{\ell,1}^{m,0}\tilde{S}_{\ell+1}^{m}(\mathbf{c_{nk}}) \end{pmatrix} + \ldots \\ \frac{1}{\sqrt{2}a_k^3}\begin{pmatrix} g_{1,k}^{-1} - g_{1,k}^{1} \\ -\imath(g_{1,k}^{-1} + g_{1,k}^{1}) \\ -\sqrt{2}g_{1,k}^{0} \end{pmatrix} \tag{3.64}$$

Noting $g_{\ell,n}^{m} = x_j = x_{(n-1)L(L+2)+l^2+l+m}$, we have :

$$\begin{pmatrix} C_{\bullet x} \\ C_{\bullet y} \\ C_{\bullet z} \end{pmatrix}_{nk} = \sum_{j=1}^{N_b L(L+2)} x_j \mathbf{C_j} \tag{3.65}$$

with

- $\forall n \neq k$

$$\mathbf{C_j} = \frac{1}{\sqrt{2}}\sum_{\ell=1}^{\infty}\sum_{m=-\ell}^{\ell}\sum_{\substack{n=1\\n\neq k}}^{N_b}\begin{pmatrix} D_{\ell,1}^{m,-1}\tilde{S}_{\ell+1}^{m+1}(\mathbf{c_{nk}}) - D_{\ell,1}^{m,1}\tilde{S}_{\ell+1}^{m-1}(\mathbf{c_{nk}}) \\ -\imath(D_{\ell,1}^{m,-1}\tilde{S}_{\ell+1}^{m+1}(\mathbf{c_{nk}}) + D_{\ell,1}^{m,1}\tilde{S}_{\ell+1}^{m-1}(\mathbf{c_{nk}})) \\ -\sqrt{2}D_{\ell,1}^{m,0}\tilde{S}_{\ell+1}^{m}(\mathbf{c_{nk}}) \end{pmatrix}, \tag{3.66}$$

- For $n = k$

$$\mathbf{C_j} = \frac{1}{a_k^3}\begin{cases} 2\mathbf{I_1^{-1}} & \text{,if } \ell = 1, m = -1 \quad \text{or } j = (n-1)L(L+2)+1 \\ -\mathbf{I_1^0} & \text{,if } \ell = 1, m = 0 \quad \text{or } j = (n-1)L(L+2)+2 \\ 2\mathbf{I_1^1} & \text{,if } \ell = 1, m = 1 \quad \text{or } j = (n-1)L(L+2)+3 \\ 0 & \text{,if } \ell \neq 1 \end{cases} \tag{3.67}$$

3.8.C In line case - analytical solution

We will study the specific case of two identical bubbles : bubble "1", located in [0 0 0], has a vertical velocity $\dot{z}$ and bubble "2", located in [0 0 c],has a vertical velocity $-\dot{z}$. Consequently, in spherical coordinates, we have $\mathbf{c_{12}} = [c\ 0\ 0]$ and $\mathbf{c_{21}} = [c\ \pi\ 0]$. As $P_\ell^m(1) = \delta_{0m}$ and $P_\ell^m(-1) = (-1)^\ell \delta_{0m}$ we deduce from equation (3.3) :

$$\begin{aligned} S_\ell^m(\mathbf{c_{12}}) &= \frac{\delta_{0m}}{c^{\ell+1}} \\ S_\ell^m(\mathbf{c_{21}}) &= (-1)^\ell \frac{\delta_{0m}}{c^{\ell+1}} \end{aligned} \tag{3.68}$$

System (3.59) leads to $\forall \mu \neq 0, g_{\ell,2}^\mu = g_{\ell,1}^\mu = 0$. With the superscript $^\mu$ removed for clarity and knowing $D_{\ell,\lambda}^{0,0} = (-1)^\lambda \binom{\lambda+\ell}{\ell}$, system (3.59) yields

$$\begin{aligned} k=1 : \sum_{\ell=1}^{\infty} \left(g_{\ell,2}(-1)^\ell \binom{\lambda+\ell}{\ell} \frac{\lambda}{\lambda+1} \frac{a^{2\lambda+1}}{c^{\lambda+\ell+1}} \right) - g_{\lambda,1} &= \delta_{\lambda,1} \frac{a^3}{2} \dot{z} \\ k=2 : \sum_{\ell=1}^{\infty} \left(g_{\ell,1}(-1)^\lambda \binom{\lambda+\ell}{\ell} \frac{\lambda}{\lambda+1} \frac{a^{2\lambda+1}}{c^{\lambda+\ell+1}} \right) - g_{\lambda,2} &= -\delta_{\lambda,1} \frac{a^3}{2} \dot{z} \end{aligned} \tag{3.69}$$

Equations for $k = 1$ and $k = 2$ become equivalent, if we have $A_\ell a^{\ell+2} = g_{\ell,1} = (-1)^\ell g_{\ell,2}$, we obtain :

$$\sum_{\ell=1}^{\infty} \left(A_\ell \binom{\lambda+\ell}{\ell} \frac{\lambda}{\lambda+1} \left(\frac{a}{c}\right)^{\lambda+\ell+1} \right) - A_\lambda = \delta_{\lambda,1} \frac{\dot{z}}{2} \tag{3.70}$$

Assuming $A_l = \sum_{k=0}^{\infty} \frac{\dot{z}}{2} \alpha_{\ell,k} \left(\frac{a}{c}\right)^k$, we obtain :

$$\sum_{\ell=1}^{\infty} \left(\sum_{n=0}^{\infty} \alpha_{\ell,n} \binom{\lambda+\ell}{\ell} \frac{\lambda}{\lambda+1} \left(\frac{a}{c}\right)^{\lambda+\ell+n+1} \right) - \sum_{k=0}^{\infty} \alpha_{\lambda,k} \left(\frac{a}{c}\right)^k = \delta_{\lambda,1}. \tag{3.71}$$

We deduce

$$\begin{cases} \alpha_{\lambda,k} = 0 \text{ except } \alpha_{1,0} = -1 & \forall k < \lambda+1 \\ \alpha_{\lambda,k} = \sum_{\ell=1}^{k-\lambda-1} \alpha_{\ell,k-\lambda-\ell-1} \binom{\lambda+\ell}{\ell} \frac{\lambda}{\lambda+1}, & \forall k \geq \lambda+2 \end{cases} \tag{3.72}$$

Then we will study the specific case of two identical bubbles : bubble "1", located in [0 0 0], has a vertical velocity $\dot{z}$ and bubble "2",located in [0 0 c], has a vertical velocity $\dot{z}$. The system

becomes :

$$\begin{aligned} k=1 &: \sum_{\ell=1}^{\infty}\left(g_{\ell,2}(-1)^{\ell}\binom{\lambda+\ell}{\ell}\frac{\lambda}{\lambda+1}\frac{a^{2\lambda+1}}{c^{\lambda+\ell+1}}\right)-g_{\lambda,1}=\delta_{\lambda,1}\frac{a^3}{2}\dot{z} \\ k=2 &: \sum_{\ell=1}^{\infty}\left(g_{\ell,1}(-1)^{\lambda}\binom{\lambda+\ell}{\ell}\frac{\lambda}{\lambda+1}\frac{a^{2\lambda+1}}{c^{\lambda+\ell+1}}\right)-g_{\lambda,2}=\delta_{\lambda,1}\frac{a^3}{2}\dot{z} \end{aligned} \tag{3.73}$$

Equations for $k=1$ and $k=2$ become equivalents, if we have $B_\ell a^{\ell+2}=g_{\ell,1}=(-1)^{\ell+1}g_{\ell,2}$. We get :

$$\sum_{\ell=1}^{\infty}\left(B_\ell\binom{\lambda+\ell}{\ell}\frac{\lambda}{\lambda+1}\left(\frac{a}{c}\right)^{\lambda+\ell+1}\right)+B_\lambda=-\delta_{\lambda,1}\frac{\dot{z}}{2} \tag{3.74}$$

Assuming $Y_l=\sum_{k=0}^{\infty}\frac{\dot{z}}{2}\beta_{\ell,k}\left(\frac{a}{c}\right)^k$, we obtain :

$$\sum_{\ell=1}^{\infty}\left(\sum_{n=0}^{\infty}\beta_{\ell,n}\binom{\lambda+\ell}{\ell}\frac{\lambda}{\lambda+1}\left(\frac{a}{c}\right)^{\lambda+\ell+n+1}\right)+\sum_{k=0}^{\infty}\beta_{\lambda,k}\left(\frac{a}{c}\right)^k=-\delta_{\lambda,1}, \tag{3.75}$$

we deduce

$$\begin{cases} \beta_{\lambda,k}=0 \text{ except } \beta_{1,0}=-1 & \forall k<\lambda+1 \\ \beta_{\lambda,k}=-\sum_{\ell=1}^{k-\lambda-1}\beta_{\ell,k-\lambda-\ell-1}\binom{\lambda+\ell}{\ell}\frac{\lambda}{\lambda+1}, & \forall k\geq\lambda+2 \end{cases} \tag{3.76}$$

Finally, one bubble,located in [0 0 0], with a vertical velocity $\dot{z}$ and one still bubble located in [0 0 c] is the sum divided by two of the two preceding cases. It generates the following velocity potential :

$$\frac{\partial\Phi}{\partial\dot{z}}=\sum_{\ell=1}^{\infty}\left[\overbrace{\sum_{k=0}^{\infty}\frac{\alpha_{\ell,k}+\beta_{\ell,k}}{4}\left(\frac{a}{c}\right)^k a^{\ell+2}}^{g_{\ell,1}}\frac{P_\ell(\cos\theta_1)}{r_1^{\ell+1}}+\ldots\right.$$
$$\left.\underbrace{\sum_{k=0}^{\infty}(-1)^{\ell}\frac{\alpha_{\ell,k}-\beta_{\ell,k}}{4}\left(\frac{a}{c}\right)^k a^{\ell+2}}_{g_{\ell,2}}\frac{P_\ell(\cos\theta_2)}{r_2^{\ell+1}}\right] \tag{3.77}$$

From equation (3.32) we can express the added mass of bubble "1" :

$$\begin{aligned} C_{zz} &= -\sum_{\ell=1}^{\infty}g_{\ell,2}D_{\ell,1}^{0,0}\tilde{S}_{\ell+1}^{0}(\mathbf{c_{21}})-\frac{1}{a^3}g_{1,1} \\ &= -\sum_{\ell=0}^{\infty}\sum_{k=0}^{\infty}\frac{\alpha_{\ell,k}-\beta_{\ell,k}}{4}\left(\frac{a}{c}\right)^{k+\ell+2}(\ell+1)-\sum_{k=0}^{\infty}\frac{\alpha_{1,k}+\beta_{1,k}}{4}\left(\frac{a}{c}\right)^k \\ &= \frac{1}{2}\left[1+\frac{3}{64}\left(\frac{2a}{c}\right)^6+\frac{9}{256}\left(\frac{2a}{c}\right)^8+\frac{9}{512}\left(\frac{2a}{c}\right)^{10}+\sum_{n=11}^{\infty}d_n\left(\frac{2a}{c}\right)^n\right] \end{aligned} \tag{3.78}$$

Exact values for d_n up to $n = 66$ are presented in table 3.2. The values, for which d_n is not reported, are null.

From equation (3.32) we can express the added mass of bubble "2" :

$$\begin{aligned} C_{zz_{ind}} &= -\sum_{\ell=1}^{\infty} g_{\ell,1} D^{0,0}_{\ell,1} \tilde{S}^0_{\ell+1}(\mathbf{c_{12}}) - \frac{1}{a^3} g_{1,2} \\ &= -\sum_{\ell=0}^{\infty}\sum_{k=0}^{\infty} \frac{\alpha_{\ell,k}+\beta_{\ell,k}}{4}\left(\frac{a}{c}\right)^{k+\ell+2}(\ell+1) + \sum_{k=0}^{\infty}\frac{\alpha_{1,k}-\beta_{1,k}}{4}\left(\frac{a}{c}\right)^k \\ &= \frac{1}{2}\left[-\frac{3}{8}\left(\frac{2a}{c}\right)^3 - \frac{3}{512}\left(\frac{2a}{c}\right)^9 - \frac{9}{1024}\left(\frac{2a}{c}\right)^{11} + \sum_{n=12}^{\infty} d_n^{ind}\left(\frac{2a}{c}\right)^n\right] \end{aligned} \tag{3.79}$$

Exact values for d_n^{ind} up to $n = 69$ are presented in table 3.3. The values, for which d_n^{ind} is not reported, are null. According to the trend of d_n and d_n^{ind} when $n \to \infty$, C_{zz} and $C_{zz_{ind}}$ approximation can be expressed with a dilogarithm also known as Spence's function. Note that Spence's function has analytical values for $c/(2a) = 1$, $c/(2a) = 2$ and $c/(2a) \to \infty$.

3.8.D Side by side case - analytical solution

We will study the specific case of two identical bubbles : bubble "1", located in [0 0 0], has an horizontal velocity $\dot{x}$ and bubble "2",located in [0 0 c], has a horizontal velocity $-\dot{x}$. Consequently, in spherical coordinates, we have $\mathbf{c_{12}} = [c\ 0\ 0]$ and $\mathbf{c_{21}} = [c\ \pi\ 0]$. As $P_\ell^m(1) = \delta_{0m}$ and $P_\ell^m(-1) = (-1)^\ell \delta_{0m}$, from equation (3.3), we deduce :

$$\begin{aligned} S_\ell^m(\mathbf{c_{12}}) &= \frac{\delta_{0m}}{c^{\ell+1}} \\ S_\ell^m(\mathbf{c_{21}}) &= (-1)^\ell \frac{\delta_{0m}}{c^{\ell+1}} \end{aligned} \tag{3.80}$$

System (3.59) leads to $\forall |\mu| \neq 1, g^\mu_{\ell,2} = g^\mu_{\ell,1} = 0$. We will denote $g_{\ell,n} = g^1_{\ell,n} = -g^{-1}_{\ell,n}$. Considering :

$$D^{-1,-1}_{\ell,\lambda} = D^{1,1}_{\ell,\lambda} = (-1)^{\lambda+1}\binom{\lambda+\ell}{\ell+1}\sqrt{\frac{\ell(\ell+1)}{\lambda(\lambda+1)}}, \tag{3.81}$$

system (3.59) becomes $\forall \lambda \in \mathbb{N}^* \forall |\mu| = 1$

$$\begin{aligned} k = 1 : \sum_{\ell=1}^{\infty}\left(g_{\ell,2}(-1)^{\ell+1}\binom{\lambda+\ell}{\ell+1}\sqrt{\frac{\ell(\ell+1)}{\lambda(\lambda+1)}}\frac{\lambda}{\lambda+1}\frac{a^{2\lambda+1}}{c^{\lambda+\ell+1}}\right) - g_{\lambda,1} &= \delta_{\lambda,1}\frac{\sqrt{2}a^3}{4}\dot{x} \\ k = 2 : \sum_{\ell=1}^{\infty}\left(g_{\ell,1}(-1)^{\lambda+1}\binom{\lambda+\ell}{\ell+1}\sqrt{\frac{\ell(\ell+1)}{\lambda(\lambda+1)}}\frac{\lambda}{\lambda+1}\frac{a^{2\lambda+1}}{c^{\lambda+\ell+1}}\right) - g_{\lambda,2} &= -\delta_{\lambda,1}\frac{\sqrt{2}a^3}{4}\dot{x} \end{aligned} \tag{3.82}$$

Tableau 3.2 ANALYTICAL EXPANSION OF C_{zz}

n	d_n	$d_n \times n^2$
0	1	~ 0
6	3/64	~ 1.69
8	9/256	~ 2.25
10	9/512	~ 1.76
12	33/4096	~ 1.16
14	9/2048	~ 0.86
16	27/8192	~ 0.84
18	789/262144	~ 0.98
20	1503/524288	~ 1.15
22	5625/2097152	~ 1.30
24	5121/2097152	~ 1.41
26	36477/16777216	~ 1.47
28	64017/33554432	~ 1.50
30	111513/67108864	~ 1.50
32	6205851/4294967296	~ 1.48
34	5411979/4294967296	~ 1.46
36	75978129/68719476736	~ 1.43
38	268836237/274877906944	~ 1.41
40	959870979/1099511627776	~ 1.40
42	3458446581/4398046511104	~ 1.39
44	6283543599/8796093022208	~ 1.38
46	23004849681/35184372088832	~ 1.38
48	169523528265/281474976710656	~ 1.39
50	156971731833/281474976710656	~ 1.39
52	2335368160413/4503599627370496	~ 1.40
54	2178780852285/4503599627370496	~ 1.41
56	8152205367807/18014398509481984	~ 1.42
58	7641749644947/18014398509481984	~ 1.43
60	114811018046739/288230376151711744	~ 1.43
62	107968452140781/288230376151711744	~ 1.44
64	1626682348775871/4611686018427387904	~ 1.44
66	3067263855097249/9223372036854775808	~ 1.45
> 66	$\sim 1.5/n^2$ if n is even, 0 else	$\sim 1.45 - 1.55$

Tableau 3.3 ANALYTICAL EXPANSION OF $C_{zz_{ind}}$

n	d_n^{ind}	$d_n^{ind} \times n^2$
3	−3/8	~ 3.38
9	−3/512	~ 0.48
11	−9/1024	~ 1.06
13	−9/1024	~ 1.49
15	−243/32768	~ 1.67
17	−189/32768	~ 1.67
19	−2277/524288	~ 1.57
21	−6867/2097152	~ 1.44
23	−2655/1048576	~ 1.34
25	−34155/16777216	~ 1.27
27	−229053/134217728	~ 1.24
29	−6219/4194304	~ 1.25
31	−177435/134217728	~ 1.27
33	−10289523/8589934592	~ 1.30
35	−18809505/17179869184	~ 1.34
37	−34518501/34359738368	~ 1.38
39	−507412029/549755813888	~ 1.40
41	−1864880361/2199023255552	~ 1.43
43	−856618335/1099511627776	~ 1.44
45	−25185714363/35184372088832	~ 1.45
47	−2894330493/4398046511104	~ 1.45
49	−85249856997/140737488355328	~ 1.45
51	−157202961801/281474976710656	~ 1.45
53	−2324076583131/4503599627370496	~ 1.45
55	−269094543057/562949953421312	~ 1.45
57	−63981599146629/144115188075855872	~ 1.44
59	−119180377216323/288230376151711744	~ 1.44
61	−111310668397413/288230376151711744	~ 1.44
63	−833953103134705/2305843009213693952	~ 1.44
65	−391521679577675/1152921504606846976	~ 1.43
67	−5896304563677775/18446744073709551616	~ 1.43
69	−5562443587404469/18446744073709551616	~ 1.44
> 69	$\sim -1.5/n^2$ if n is odd, 0 else	~ 1.45 − .55

Equations for $k = 1$ and $k = 2$ become equivalents, if we have $G_\ell a^{\ell+2}/\sqrt{\ell(\ell+1)} = g_{\ell,1} = (-1)^\ell g_{\ell,2}$. We obtain :

$$\sum_{\ell=1}^{\infty}\left(G_\ell\binom{\lambda+\ell}{\ell+1}\frac{\lambda}{\lambda+1}\left(\frac{a}{c}\right)^{\lambda+\ell+1}\right)+G_\lambda=-\delta_{\lambda,1}\frac{\dot{x}}{2} \tag{3.83}$$

Assuming $G_l = \sum_{k=0}^{\infty}\frac{\dot{x}}{2}\gamma_{\ell,k}\left(\frac{a}{c}\right)^k$, we obtain :

$$\sum_{\ell=1}^{\infty}\left(\sum_{n=0}^{\infty}\gamma_{\ell,n}\binom{\lambda+\ell}{\ell+1}\frac{\lambda}{\lambda+1}\left(\frac{a}{c}\right)^{\lambda+\ell+n+1}\right)+\sum_{k=0}^{\infty}\gamma_{\lambda,k}\left(\frac{a}{c}\right)^k=-\delta_{\lambda,1} \tag{3.84}$$

We deduce

$$\begin{cases}\gamma_{\lambda,k}=0 \text{ except } \gamma_{1,0}=-1 & \forall k<\lambda+1\\ \gamma_{\lambda,k}=-\sum_{\ell=1}^{k-\lambda-1}\gamma_{\ell,k-\lambda-\ell-1}\binom{\lambda+\ell}{\ell+1}\frac{\lambda}{\lambda+1}, & \forall k\geq\lambda+2\end{cases} \tag{3.85}$$

We consider now the specific case of two identical bubbles : bubble "1",located in [0 0 0], has an horizontal velocity $\dot{x}$ and bubble "2",located in [0 0 c], has a horizontal velocity $\dot{x}$. We will denote again $g_{\ell,n} = g^1_{\ell,n} = -g^{-1}_{\ell,n}$ and then the system (3.59) becomes $\forall\lambda\in\mathbb{N}^*\forall|\mu|=1$

$$\begin{aligned}k=1:&\sum_{\ell=1}^{\infty}\left(g_{\ell,2}(-1)^{\ell+1}\binom{\lambda+\ell}{\ell+1}\sqrt{\frac{\ell(\ell+1)}{\lambda(\lambda+1)}}\frac{\lambda}{\lambda+1}\frac{a^{2\lambda+1}}{c^{\lambda+\ell+1}}\right)-g_{\lambda,1}=\delta_{\lambda,1}\frac{\sqrt{2}a^3}{4}\dot{x}\\ k=2:&\sum_{\ell=1}^{\infty}\left(g_{\ell,1}(-1)^{\lambda+1}\binom{\lambda+\ell}{\ell+1}\sqrt{\frac{\ell(\ell+1)}{\lambda(\lambda+1)}}\frac{\lambda}{\lambda+1}\frac{a^{2\lambda+1}}{c^{\lambda+\ell+1}}\right)-g_{\lambda,2}=\delta_{\lambda,1}\frac{\sqrt{2}a^3}{4}\dot{x}\end{aligned} \tag{3.86}$$

Equations for $k = 1$ and $k = 2$ become equivalents, if we have $E_\ell a^{\ell+2}/\sqrt{\ell(\ell+1)} = g_{\ell,1} = (-1)^{\ell+1} g_{\ell,2}$. We obtain :

$$\sum_{\ell=1}^{\infty}\left(E_\ell\binom{\lambda+\ell}{\ell+1}\frac{\lambda}{\lambda+1}\left(\frac{a}{c}\right)^{\lambda+\ell+1}\right)-E_\lambda=\delta_{\lambda,1}\frac{\dot{x}}{2} \tag{3.87}$$

Assuming $E_l = \sum_{k=0}^{\infty}\frac{\dot{x}}{2}\epsilon_{\ell,k}\left(\frac{a}{c}\right)^k$, we obtain :

$$\sum_{\ell=1}^{\infty}\left(\sum_{n=0}^{\infty}\epsilon_{\ell,n}\binom{\lambda+\ell}{\ell+1}\frac{\lambda}{\lambda+1}\left(\frac{a}{c}\right)^{\lambda+\ell+n+1}\right)-\sum_{k=0}^{\infty}\epsilon_{\lambda,k}\left(\frac{a}{c}\right)^k=\delta_{\lambda,1}. \tag{3.88}$$

We deduce

$$\begin{cases} \epsilon_{\lambda,k} = 0 \text{ except } \epsilon_{1,0} = -1 & \forall k < \lambda + 1 \\ \epsilon_{\lambda,k} = \sum_{\ell=1}^{k-\lambda-1} \epsilon_{\ell,k-\lambda-\ell-1} \binom{\lambda+\ell}{\ell} \frac{\lambda}{\lambda+1}, & \forall k \geq \lambda + 2 \end{cases} \tag{3.89}$$

Finally, one bubble, located in [0 0 0], with a horizontal velocity $\dot{x}$ and a still bubble still, located in [0 0 c], generates the following velocity potential (sum divided by two of the two preceding cases) :

$$\frac{\partial \Phi}{\partial \dot{x}} = -\sum_{\ell=1}^{\infty} \left[\overbrace{\sum_{k=0}^{\infty} \frac{\gamma_{\ell,k} + \varepsilon_{\ell,k}}{4\sqrt{\ell(\ell+1)}} \left(\frac{a}{c}\right)^k a^{\ell+2}}^{g_{\ell,1} = g^1_{\ell,1} = -g^{-1}_{\ell,1}} \frac{P^1_\ell(\cos\theta_1)}{r_1^{\ell+1}} \frac{2\cos\varphi_1}{\sqrt{\ell(\ell+1)}} + \ldots \right.$$
$$\left. \underbrace{\sum_{k=0}^{\infty} (-1)^\ell \frac{\gamma_{\ell,k} - \varepsilon_{\ell,k}}{4\sqrt{\ell(\ell+1)}} \left(\frac{a}{c}\right)^k a^{\ell+2}}_{g_{\ell,2} = g^1_{\ell,2} = -g^{-1}_{\ell,2}} \frac{P^1_\ell(\cos\theta_2)}{r_2^{\ell+1}} \frac{2\cos\varphi_2}{\sqrt{\ell(\ell+1)}} \right] \tag{3.90}$$

From equation (3.32) we can express the added mass of bubble "1" (note that $g_{\ell,n} = g^1_{\ell,n} = -g^{-1}_{\ell,n}$) :

$$\begin{aligned} C_{xx} = C_{yy} &= -\sum_{\ell=1}^{\infty} \sqrt{2} g_{\ell,2} D^{1,1}_{\ell,1} \tilde{S}^0_{\ell+1}(\mathbf{c_{21}}) - \frac{\sqrt{2}}{a^3} g_{1,1} \\ &= \sum_{\ell=1}^{\infty} \sum_{k=0}^{\infty} \frac{\gamma_{\ell,k} - \varepsilon_{\ell,k}}{4} \left(\frac{a}{c}\right)^{k+\ell+2} - \sum_{k=0}^{\infty} \frac{\gamma_{1,k} + \varepsilon_{1,k}}{4} \left(\frac{a}{c}\right)^k \\ &= \frac{1}{2}\left[1 + \frac{3}{256}\left(\frac{2a}{c}\right)^6 + \frac{3}{256}\left(\frac{2a}{c}\right)^8 + \frac{27}{4096}\left(\frac{2a}{c}\right)^{10} + \sum_{n=12}^{\infty} e_n \left(\frac{2a}{c}\right)^n\right] \end{aligned} \tag{3.91}$$

Exact values for e_n up to n=40 are presented in table 3.4. The values, for which e_n is not reported, are null.

From equation (3.32) we can express the added mass of bubble "2" as :

$$\begin{aligned} C_{xx_{ind}} &= C_{yy_{ind}} = -\sum_{\ell=1}^{\infty} \sqrt{2} g_{\ell,1} D^{1,1}_{\ell,1} \tilde{S}^0_{\ell+1}(\mathbf{c_{12}}) - \frac{\sqrt{2}}{a^3} g_{1,2} \\ &= \sum_{\ell=0}^{\infty} \sum_{k=0}^{\infty} \frac{\gamma_{\ell,k} + \varepsilon_{\ell,k}}{4} \left(\frac{a}{c}\right)^{k+\ell+2} + \sum_{k=0}^{\infty} \frac{\gamma_{1,k} - \varepsilon_{1,k}}{4} \left(\frac{a}{c}\right)^k \\ &= \frac{1}{2}\left[\frac{3}{16}\left(\frac{2a}{c}\right)^3 + \frac{3}{4096}\left(\frac{2a}{c}\right)^9 + \frac{3}{2048}\left(\frac{2a}{c}\right)^{11} + \sum_{n=12}^{\infty} e^{ind}_n \left(\frac{2a}{c}\right)^n\right] \end{aligned} \tag{3.92}$$

Exact values for e^{ind}_n up to n=41 are presented in table 3.5. The values, for which e^{ind}_n

is not reported, are null. According to the trend of e_n and e_n^{ind} when $n \to \infty$, C_{xx} and $C_{xx_{ind}}$ approximation can be expressed as a polylogarithm function also known as Jonquière's function.

Tableau 3.4 ANALYTICAL EXPANSION OF C_{xx} or C_{yy}

n	e_n	$e_n \times n^{2,4}$
0	1	~ 0
6	3/256	~ 0.86
8	3/256	~ 1.72
10	27/4096	~ 1.66
12	195/65536	~ 1.16
14	21/16384	~ 0.72
16	689/1048576	~ 0.51
18	24121/50331648	~ 0.49
20	3753/8388608	~ 0.59
22	118983/268435456	~ 0.74
24	9232443/21474836480	~ 0.88
26	19414531/48318382080	~ 1.00
28	3369179819/9277129359360	~ 1.08
30	26380886429/82463372083200	~ 1.12
32	47933417293/173173081374720	~ 1.13
34	3938387628451/16624615811973120	~ 1.12
36	805224694292273/3989907794873548800	~ 1.10
38	58838001082253/341992096703447040	~ 1.06
40	3136888504211549/21279508239325593600	~ 1.03
> 40	$\sim 1/n^{2.4}$ if n is even, 0 else	~ 0.95 – 1.05

Tableau 3.5 ANALYTICAL EXPANSION OF $C_{xx_{ind}}$ or $C_{yy_{ind}}$

n	e_n^{ind}	$e_n^{ind} \times n^{2,4}$
3	3/16	~ 2.62
9	3/4096	~ 0.14
11	3/2048	~ 0.47
13	59/32768	~ 0.85
15	1827/1048576	~ 1.16
17	3075/2097152	~ 1.32
19	4751/4194304	~ 1.33
21	3354637/4026531840	~ 1.24
23	2904515/4831838208	~ 1.11
25	939073/2147483648	~ 0.99
27	338657701/1030792151040	~ 0.89
29	2243249765/8658654068736	~ 0.84
31	15976663637/74217034874880	~ 0.82
33	6663776732011/35624176739942400	~ 0.83
35	3098143748599/18471795346636800	~ 0.85
37	5657390434351/36943590693273600	~ 0.89
39	14997472824454259/106397541196627968000	~ 0.93
41	49787904667645363/383031148307860684800	~ 0.97
> 41	$\sim 1/n^{2.4}$ if n is odd, 0 else	~ 0.95 – 1.05

References

BATCHELOR, G. (2010). *An introduction to fluid dynamics*. Cambridge University Press, New York, 14^e édition.

BIESHEUVEL, A. and SPOELSTRA, S. (1989). The added mass coefficient of a dispersion of spherical gas-bubbles in liquid. *International Journal of Multiphase Flow*, 15, 911–924.

BIESHEUVEL, A. and VAN WIJNGAARDEN, L. (1982). The motion of pairs of gas bubbles in a perfect liquid. *Journal of engineering Mathematics*, 16, 349–365.

BRENNEN, C. (2005). *Fundamentals of Multiphase Flow*. Cambridge University Press.

CAI, X. L. and WALLIS, G. B. (1994). A more general cell model for added-mass in 2-phase flow. *Chemical Engineering Science*, 49, 1631–1638.

DARMANA, D., DEEN, N., KUIPERS, J., HARTEVELD, W. and MUDDE, R. (2009). Numerical study of homogeneous bubbly flow : influence of the inlet conditions to the hydrodynamic behavior. *International Journal of Multiphase Flow*, 35, 1077–1099.

ISHII, M. and HIBIKI, T. (2006). *Thermo-Fluid Dynamics*. Springer.

KENDOUSH, A., SULAYMON, A. and S.A.M, M. (2007). Experimental evaluation of the virtual mass of two solid spheres accelerating in fluids. *Experimental Thermal and Fluid Science*, 31, 813–823.

KOK, J. (1993). Dynamics of a pair of gas bubbles moving through liquid. i : Theory. *European journal of mechanics. B, Fluids*, 12, 515–540.

KUMARAN, V. and KOCH, D. (1993). The effect of hydrodynamic interactions on the average properties of a bidisperse suspension of high reynolds number, low weber number bubbles. *Physics of Fluids A : Fluid Dynamics*, 5, 1123.

KUSHCH, V. I., SANGANI, A. S., SPELT, P. D. and KOCH, D. L. (2002). Finite-weber-number motion of bubbles through a nearly inviscid liquid. *Journal of Fluid Mechanics*, 460, 241–280.

LEGENDRE, D., MAGNAUDET, J. and MOUGIN, G. (2003). Hydrodynamic interactions between two spherical bubbles rising side by side in a viscous liquid. *Journal of Fluid Mechanics*, 497, 133–166.

MILNE-THOMSON, L. (1968). *Theorical Hydrodynamics*. Macmillan, New York, 5^e édition.

MOKEYEV, G. (1977). Effect of particule concentration on their drag and induced mass. *Fluid Mechanics Sov. Res.*, 6, 161.

NIEMANN, J. and LAURIEN, E. (1991). Computing virtual mass by direct numerical simulation. *Journal of Pressure Vessel Technology*, 113, 233–253.

SANGANI, A. S. and DIDWANIA, A. (1993). Dynamic simulations of flows of bubbly liquids at large reynolds numbers. *Journal of Fluid Mechanics*, 250, 307–337.

SANGANI, A. S., ZHANG, D. and PROSPERETTI, A. (1991). The added mass, basset, and viscous drag coefficients in nondilute bubbly liquids undergoing small-amplitude oscillatory motion. *Physics of Fluids A : Fluid Dynamics*, 3, 2955–2970.

SIMCIK, M., RUZICKA, M. and DRAHOS, J. (2008). Computing the added mass of dispersed particles. *Chemical Engineering Science*, 63, 4580–4595.

SMEREKA, P. (1993). On the motion of bubbles in a periodic box. *Journal of Fluid Mechanics*, 254, 79–112.

SPELT, P. and SANGANI, A. (1997). Properties and averaged equations for flows of bubbly liquids. *Applied scientific research*, 58, 337–386.

TOMIYAMA, A., CELATA, G., HOSOKAWA, S. and YOSHIDA, S. (2002). Terminal velocity of single bubbles in surface tension force dominant regime. *International Journal of Multiphase Flow*, 28, 1497 – 1519.

TOMIYAMA, A., MATSUOKA, T., FUKUDA, T. and SAKAGUCHI, T. (1995). Transverse migration of single bubbles in simple shear flows. *Advances in Multiphase Flow, Society of Petroleum Engineers, Inc*, 241–252.

VAN GELDEREN, M. (1998). The shift operators and translations of spherical harmonics. *DEOS Progress Letter*, 1, 57–67.

VAN WIJNGAARDEN, L. (1976). Hydrodynamic interaction between gas bubbles in liquid. *Journal of Fluid Mechanics*, 77, 27–44.

VAN WIJNGAARDEN, L. (1991). *Bubble Deformation in Bubbly Liquid and Its Effect on the Stability of Voidage Waves*. Mathematical approaches in Hydrodynamics, SIAM, miloh t. édition.

WALLIS, G. B. (1989). Inertial coupling in dispersed potential flow : macroscopic properties of suspensions in an inviscid fluid. *Multiphase Science Technology*, 5, 238–361.

ZUBER, N. (1964). On the dispersed two-phase flow in the laminar flow regime. *Chemical Engineering Science*, 19, 897–903.

CHAPITRE 4

ARTICLE 2 : EXPERIMENTS OF AIR BUBBLES IMPACTING A RIGID WALL IN TAP WATER

Dans la section précédente, les bulles étaient considérées comme rigides et la dynamique du mouvement des bulles n'a pas été discutée. Ce chapitre s'intéresse expérimentalement à la dynamique des collisions de bulles sur un mur.

Soumis pour publication dans : *Physics of Fluid*

É. PELLETIER, C. BÉGUIN & S. ÉTIENNE
BWC/AECL/NSERC Chair of Fluid-Structure Interaction
Department of Mechanical Engineering, École Polytechnique,
P.O.Box 6079, succ. Centre-Ville, Montréal (Québec), Canada, H3C 3A7

Abstract *Trajectory and impact dynamics of bubbles in tap water were studied. Results confirm that bubbles with identical radii can be classified in two categories : fast bubbles and slow bubbles. Each category of bubble can describe zig-zag or helical motion. The aspect ratio and terminal velocity of a bubble depend on its radius and category.*

Restitution relations are also presented for the two categories of bubble after impact with an horizontal wall. With these relations, the ejection state of a bubble can be predicted from its initial state. The initial aspect ratio of the bubble is found to play a key role in the dynamics of the impacts.

Finally, collisions with an inclined wall were studied. Sliding and repeated bouncing motions were observed. On repeated bounces, images suggest that the bubble rolls *into a prolate shape before ejection. Repeated bounces were only observed for fast bubbles.*

4.1 Introduction

Bubbly flows appear in many industrial applications such as steam generators, heat exchangers and chemical reactors. Different approaches can be used to model these flows : homogeneous, drift-flux, Euler-Lagrange, Euler-Euler and direct numerical simulation. In an

Euler-Lagrange formalism, bubbles are individually tracked through an Eulerian defined liquid phase. They are considered as classic bodies on which forces are applied. This approach was used by many authors to model collisions of bubbles on walls.

Many of these models (Klaseboer *et al.*, 2001; Moraga and R.T. Lahey, 2005; Canot *et al.*, 2003; Kushch *et al.*, 2002) were only compared with the study from Tsao and Koch (1997) in which only one bubble-wall impact was described. Later, Zenit and Legendre (2009) as well as Podvin *et al.* (2008) developed their models and compared them to their own experiments. For the majority of these studies, the water was considered pure and the bubble trajectories were rectilinear.

Unfortunately, in real applications, these conditions are rarely met. First, the water is likely to be contaminated to a certain degree with surfactant thus increasing shear stress at the interface. The latter or any other perturbation from the system is likely to trigger trajectory instability leading to a zig-zag or an helical path (Tomiyama *et al.*, 2002; Ellingsen and Risso, 2001).

The aim of this study is to present a realistic dataset to compare with models. The next section presents the experimental apparatus. Section 4.3 describes the details of the post-processing method. Results concerning the shape and trajectory of bubbles are grouped in section 4.4. Data from impacts with an horizontal wall are shown in section 4.5 and a qualitative analysis of impact on an inclined wall is presented in section 4.6.

4.2 Experiments

The experimental setup is shown in Fig. 4.1(a). The container is built from 2 cm thick plexiglas. Its dimensions are $10 \times 10 \times 40$ cm^3. The contact plate is made from the same plexiglas. It is held in position at a 20 cm height. Two contact plates were made for different inclinations :0° and 60°. Compression feedthroughs were inserted at the base of the column to adequately position the air feeding tubes. Two horizontal, flat ended tubes were used : 2.4mm inner diameter (ID) plastic tube and 0.6mm ID metal tube. The tubes were connected to a 1 cm^3 syringe via flexible tubing.

Bubble motions were tracked by a high-definition, black & white high speed camera at 1000 Hz. With the optical setup illustrated on Fig. 4.1(b), simultaneous and perpendicular views were obtained. This is achieved by targeting two light paths side by side on the camera sensor. Each light path starts of a halogen light source. It is then diffused by soft-box diffuser (LS) and confined by a mask to limit the exposed area (MS). The light then goes through the center of the plate, gets reflected by an optical mirror (M) and again by the beam splitter (BS). The light path ends at the high-speed camera (HSC). This set-up allowed a resolution

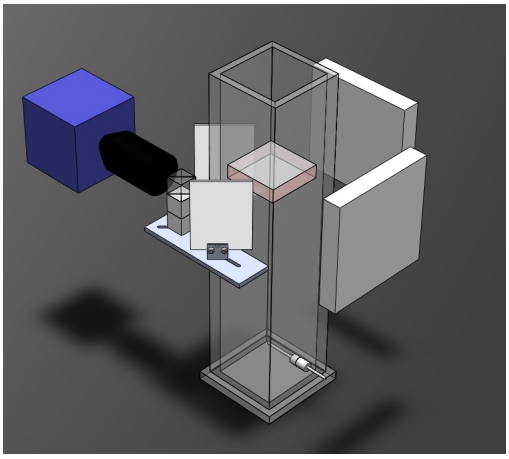

(a) Isometric view of the experimental set-up.

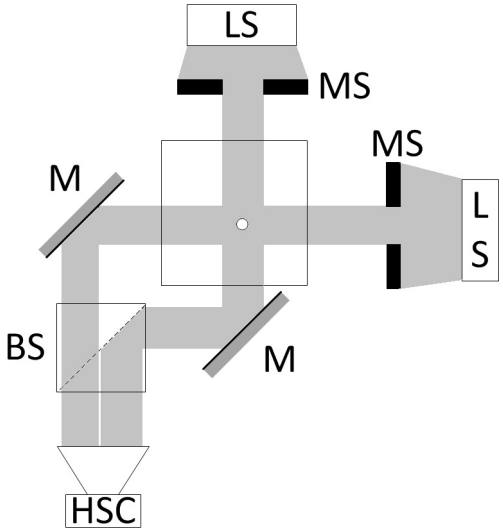

(b) Top view of the optical system.

Figure 4.1 Experimental apparatus.

of 38 μm/pixel. Each view having therefore a real size of approximately 2.2 cm width × 3.8 cm height. Each impact event includes approximately 300 images.

Tap water was poured into the container to roughly 30 cm high. The water was left still over the night to reach thermal equilibrium with the room and to allow the removal of solubilized air. Room temperature was approximately 20°C. The syringe was manually actuated in a back-and-forth motion to generate an isolated bubble. Once the bubble reaches the plexiglas plate and does not move anymore, a squeegee is used to remove it.

4.3 Post-Process

From raw images (Fig. 4.2a), a threshold is selected to distinguish bubble area from non-bubble area. On each view, the center of mass of the bubble area is calculated. The location of the center of the bubble is defined as the average of both centers of mass. z defines the vertical axis, x and y are both set perpendicular to a view.

The bubble shape is assumed to be a revolution ellipsoid of small axes a_1, a_2 and great axis b. Angles θ_x and θ_y refer to rotation about their associated axis (see Fig. 4.3). An optimization algorithm is used to fit these variables to the bubble projections. Fig. 4.2b illustrates this with the bubble projections in black and the contour of best fitted projection in white. Fig. 4.2c and Fig. 4.2d are the projection and isometric view of the reconstructed 3D bubble.

Once this process has been conducted on every frame, the equivalent radius of the bubble,

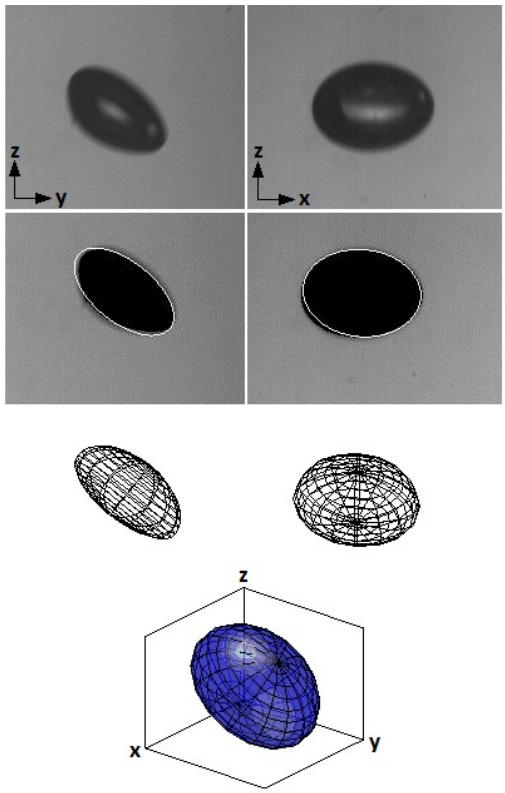

Figure 4.2 a) Raw images ; b) Threshold Best projection fit ; c) Projection ; d) 3D reconstruction.

r_b, can be determined. This equivalent radius is defined as the radius of a sphere having the same volume as the ellipsoid [*i.e.* : $(a_1 + a_2)b^2 = 2r_b^3$]. Fig. 4.4 shows the calculated values of r_b as well as the average radius for a given experiment. Small oscillations of r_b are observed before the impact (t_{impact}=0.7s) and decay after contact has been made. The variation is yet of the order of the pixel throughout the experiment. The error on the radius estimation is therefore set to 1 pixel ($\approx 40\mu m$)

From the measured ellipsoidal characteristics (a_1, a_2, b) , the aspect ratio χ is defined as

$$\chi = \frac{2b}{a_1 + a_2} \tag{4.1}$$

Note that all reported values without subscripts are averages. They were calculated from all the images of a sequence in which the bubble-wall distance is greater than 2 r_b. Values with i or f subscripts are instantaneous values.

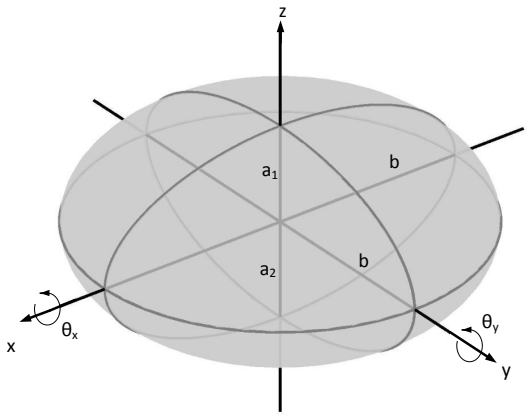

Figure 4.3 Illustration of the hypothesis on bubble shape.

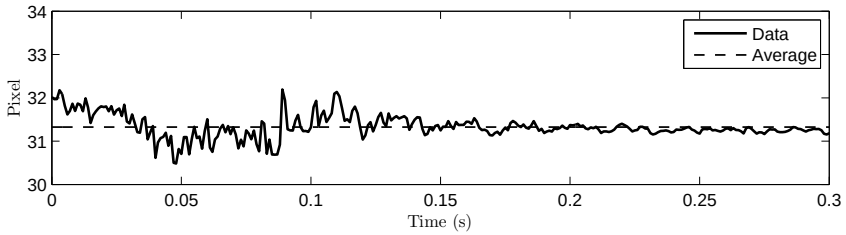

Figure 4.4 Variation on the post-processed equivalent radius r_b.

4.4 Free rise of the bubbles

In the following section, general characteristics of the bubble shapes and trajectories are presented. It will be shown that the aspect ratio of the bubble is likely to be a key driver in the terminal velocity yet it may not play an essential role in the trajectory type.

4.4.1 Types of bubble

As already described by other authors (Tomiyama *et al.*, 2002; Peters and Els, 2012), the initial deformation of a bubble determines the bubble behavior. A small initial deformation generates a low terminal velocity and a small aspect ratio bubble. In contrast, a high initial deformation leads to a higher terminal velocity and a larger aspect ratio. Our study borrows Peters and Els (2012) notation by referring to those two types of behaviors as slow bubbles and fast bubbles respectively. The associated trajectory shape will be discussed in section 4.4.2.

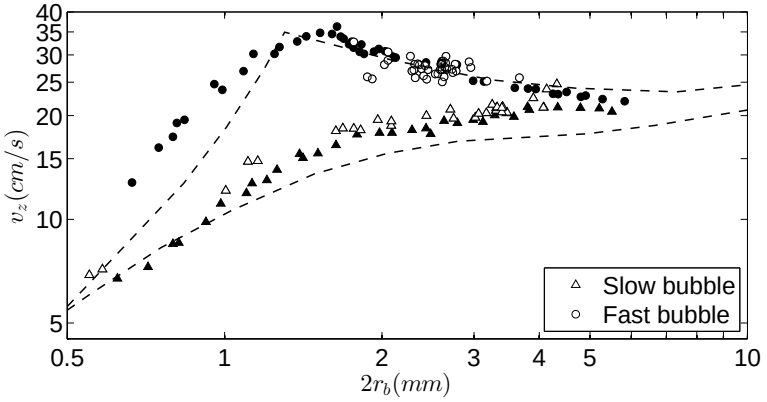

Figure 4.5 Bubble terminal velocities. (○) and (△) present experiments. (▲) and (●) Peters and Els (2012) experiments . (−−) lower and upper boundaries defined by Clift and Weber (1978).

Fig. 4.5 shows the terminal velocities of the bubbles from this study and from Peters and Els (2012) experiments . Both dataset behave similarly. The upper branch corresponds to fast bubbles and the lower branch to slow bubbles. Our slow bubble branch shows a small systematical upshift in terminal velocity. Also, our fast bubble branch presents more scatter than Peters and Els results. These discrepancies might be attributed to the variable contamination on each bubble and to the small window over which our data were collected. Peters and Els averaged the rise velocity over a distance of 560 mm. Our average was over approximately 20 mm. The following section gives details about the bubble trajectories.

4.4.2 Trajectory of bubbles

After spatial reconstruction of the bubble trajectories, projections of the motions can be plotted in the $x-y$ plane (Fig. 4.6). Both slow and fast bubbles have demonstrated zig-zag and helical trajectories. Helical trajectory seems to occur less often for slow bubbles. Table 4.1 describes the properties of the bubbles from which the projection of Fig. 4.6 are extracted.

Fast bubbles in our experiments are related to the bubble type studied by Ellingsen and Risso (2001). They show a high aspect ratio and are past the onset of path oscillation defined by Clift and Weber (1978) as Re > 450 (Re=$2r_b\rho_\ell v/\mu$). Also, note that the fast bubbles presented in Fig. 4.6 are of similar sizes to those characterized by Ellingsen and Risso (r_b = 1.25mm, χ = 2.05). The transition of a bubble trajectory from rectilinear to zig-zag to helical is well described by Ellingsen and Risso (2001). As this transition progresses, a decrease in rise velocity v_z is observed while the total velocity v remains constant. The same

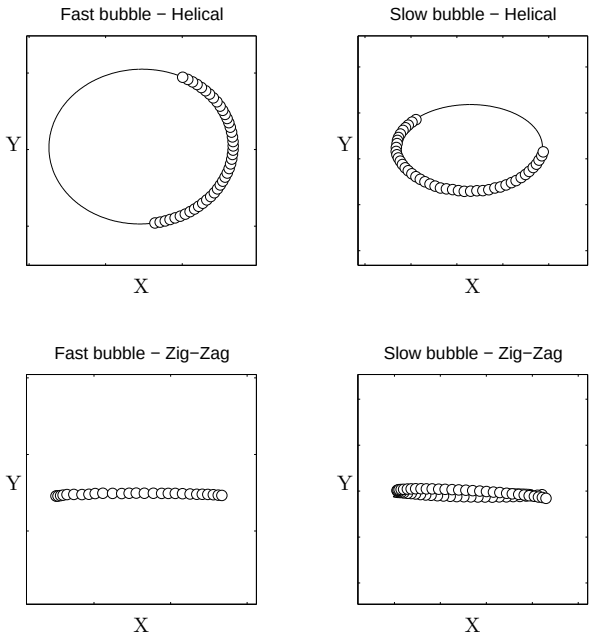

Figure 4.6 $x - y$ projection of the bubble trajectories for $|z_b| > 2r_b$.

behavior is observed in our experiments even though the nature of the growing instability might not be identical.

Slow bubbles were described by Tomiyama *et al.* (2002) as zig-zag bubbles. As mentioned by Tomiyama *et al.* (2002), some bubbles evolve from zig-zag ($\chi \approx 1$) to helical. Yet there is no mention of the aspect ratio of these helical bubbles. Our experiments show some near spherical slow bubbles exhibiting helical motion as presented in Fig. 4.6 (top-right).

Fast bubbles were generally obtained with the small capillary while slow bubbles were obtained with a larger diameter plastic tube. This is in agreement with other author's observations (Wu and Gharib, 2002). Furthermore, the bubbles were generated by a rocking motion in the syringe. Doing so, perturbations in the wake were probably facilitating the developpement of path instabilities. This could explain the early occurence of helical motion on both bubble types.

4.4.3 Aspect ratio

As it will be described in section 4.5, the aspect ratio seems to have a primordial role in the impact and the rebound of bubbles on walls. The aspect ratio of each bubble at terminal rise velocity is presented as a function of their radii in Fig. 4.7. For most of these experiments, the

Tableau 4.1 Characteristics of the bubbles associated with trajectories of Fig. 4.6.

Type	Trajectory	r_b (mm)	χ	v_z (cm/s)	v (cm/s)
fast Bubble	Helical	1.31	1.9	26.0	30.7
	Zig-Zag	1.33	2.1	28.4	31.3
slow bubble	Helical	1.03	1.14	19.2	19.9
	Zig-Zag	1.02	1.13	18.7	19.4

aspect ratios were slightly fluctuating over the observed period so the average was calculated. Two branches appear on this graph and they are used to define the slow and fast bubble type.

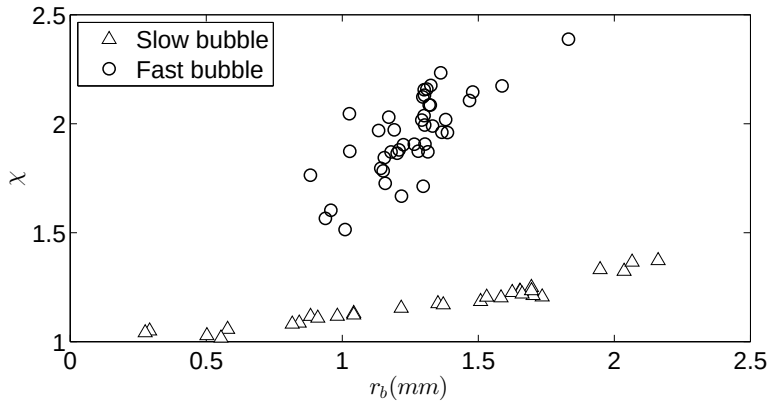

Figure 4.7 Aspect ratio of the bubbles as a function of the equivalent radius r_b.

Comparison to other works

Fig. 4.8 shows the aspect ratios of all the observed bubbles as a function of their Weber number (We) :

$$We = 2\rho r_b v^2/\sigma \tag{4.2}$$

On the graph are also shown two relations from Moore (1965). Eq. (4.3) is a first order shape approximation obtained from the equilibrium of dynamical pressure and surface tension on the surface of a spherical bubble.

$$\chi = 1 + \frac{9}{64}We \tag{4.3}$$

The second relation is based on the same equilibrium condition yet it is only imposed at the stagnation points and at the equator of an ellipsoidal bubble (Eq. (4.4)). Note that both

relations were developed in a no shear stress hypothesis (i.e. purified water).

$$We = 4\chi^{4/3}(\chi^3 + \chi - 2)[\chi^2 sec^{-1}\chi - (\chi^2 - 1)^{1/2}]^2(\chi^2 - 1)^3 \tag{4.4}$$

Legendre *et al.* (2012) proposed relation (4.5) based on experimental fits on their experiments of bubbles rising in tap water . Note that this equation fits Moore's Eq. (4.3) for small We.

$$\chi = \frac{1}{1 - \frac{9}{64}We} \tag{4.5}$$

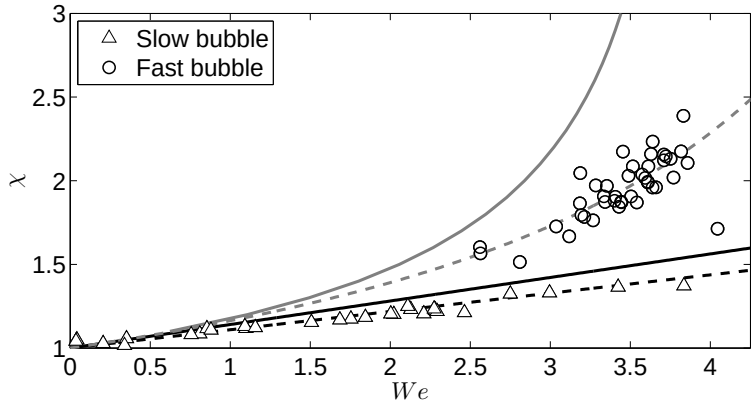

Figure 4.8 Aspect ratio (χ) as a function of Weber number. ($\circ$) and ($\triangle$) this study ; Eq. (4.3) is (-) ; Eq. (4.4) is (Gray, -) ; Eq. (4.5) is (Gray, $--$) ; Eq. (4.6) is ($--$).

Once again, two branches appear on Fig. 4.8. Slow bubbles lie on the lowest branch whereas fast bubbles are distributed on an upper branch. As the higher branch is well fitted by Legendre *et al.* relation, the first branch does not fit with any relation found in the literature. In fact, its dependency on χ is smaller than the first order approximation by Moore. The best fit on the lowest branch is

$$\chi = 1 + \frac{7}{64}We \tag{4.6}$$

This section described the terminal rising state of the bubbles. The next section will discuss the impact of a bubble with a rigid wall.

4.5 Impacts

In our study, bubbles did not depict rectilinear trajectories. This adds some complexity to the impact analysis. To describe the collision events, three parameters were chosen : (z,r,χ).

z-axis is perpendicular to the wall. r-axis is tangent to the wall in the direction of the bubble velocity. Therefore, near the wall, the bubble velocity is defined as $\mathbf{v} = (v_z, v_r)$. The motions of the bubbles are considered to stay in a fixed plane when close to the wall. That is, x and y axes can be treated as a single radial axis r.

Fig. 4.9 shows typical impacts with regards to z and χ. Fig. 4.10 shows sequences of images associated with the same impacts. These experiments were chosen to compare fast and slow bubbles of similar radius. The reader will note, without surprise, two distinct behaviors for different bubble categories. The bubble characteristics for each experiment are described in the caption. Dimensionless numbers with z subscript were calculated with the z component of velocity only. The angle between the velocity vector and vertical is defined as θ.

Slow bubbles exhibit high compression on impact compared to their initial states yet they show very low rebound height. In contrast, fast bubbles showed variable compression rates upon impact with regards to their initial states. The bubble of Fig. 4.10c compresses on impact in contrast with Fig. 4.10d that does not compress. For fast bubbles, from the first point of contact between the bubble and the wall, a nearly rigid body rotation is induced. For higher We number bubble, a more complex deformation is observed as presented in Fig. 4.10d, third image.

4.5.1 Restitution relations

In this section, the initial and ejection states of the bubbles are compared. When dealing with bubbles in rectilinear motion, it might be possible to describe the impact dynamic from a single restitution coefficient. In our case, it is not considered sufficient for some reasons. First, handling oscillatory trajectories requires the use of a tangential restitution coefficient as well. Second, to fully characterize a system, not only must the perpendicular ejection velocity be known but also a χ-velocity in order to combine it with the center of mass position and the aspect ratio. Finally, to complete this characterization, a time relation should also be observed.

The initial state was arbitrarily chosen to be the instant at which the bubble center is at a distance of $2r_b$ from the wall. This distance is considered to be large enough so that the wall does not influence significantly the bubble yet small enough for the tangential velocity to stay linear. Fig. 4.11 shows a typical $x-y$ projection of the bubble position after $t(z = 2r_b)$. It shows that the bubble radial motion stays almost linear. The ejection state is chosen to be the instant of maximal perpendicular departure velocity of the center of mass after maximal compression. In other words, it is the instant of maximal rebound velocity. At both instants, z positions, aspect ratios χ and velocity vectors $\mathbf{v} = (v_z, v_r)$ are stored. As a notation convention,

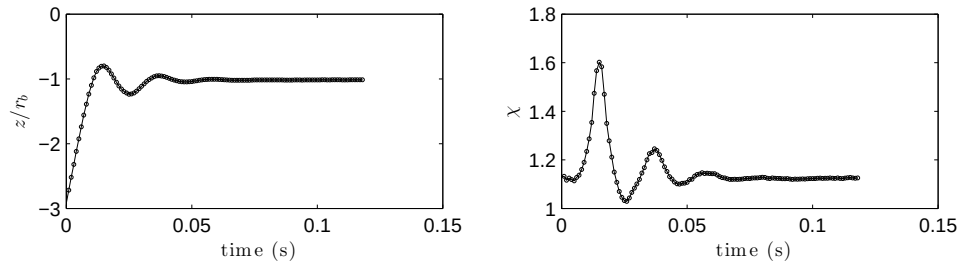

(a) Slow bubble, r_b = 1.02mm, Re=385, We=1, χ = 1.13, θ = 3°

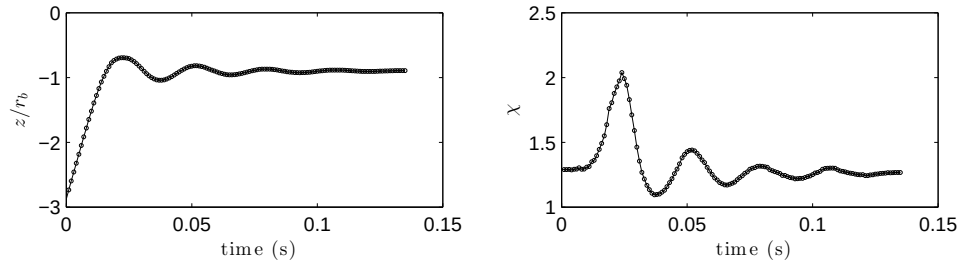

(b) Slow bubble, r_b = 1.63mm, Re=700, We=2.13, χ = 1.3, θ = 2°

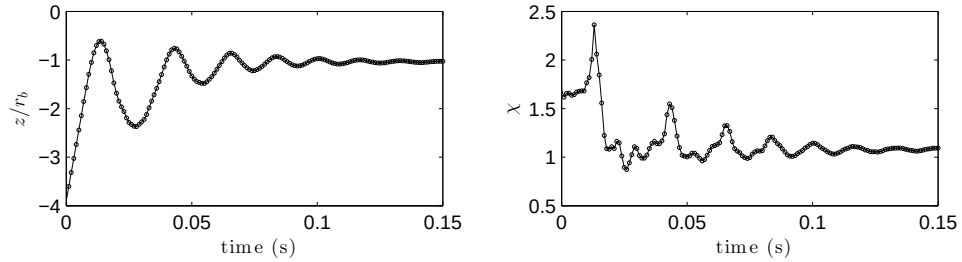

(c) Fast bubble, r_b = 0.93mm, Re=540 Re_z=470, We=2.17, We_z=1.63, χ = 1.68, θ = 30°

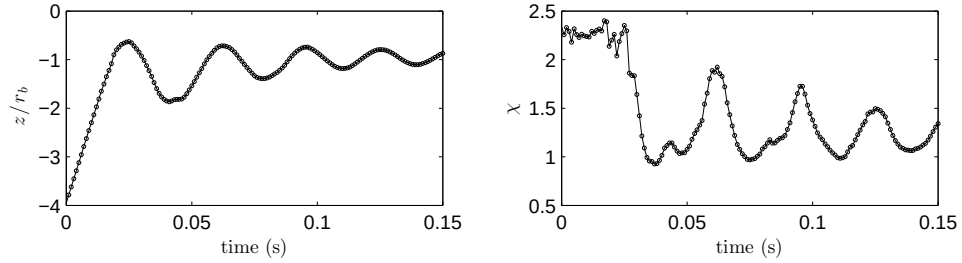

(d) Fast bubble, r_b = 1.58mm, Re=865, Re_z=800, We=3.3, We_z=2.7, χ = 2.25, θ = 23°

Figure 4.9 Typical motion (z) and aspect ratio (χ) for bubble impacting against horizontal wall.

the initial and the final states will be referred to with $_o$ and $_f$ subscripts respectively.

Also, for the restitution relations, the choice of independent axis was somewhat subjective. The ones which produced the best collapse of data for both bubble types were selected.

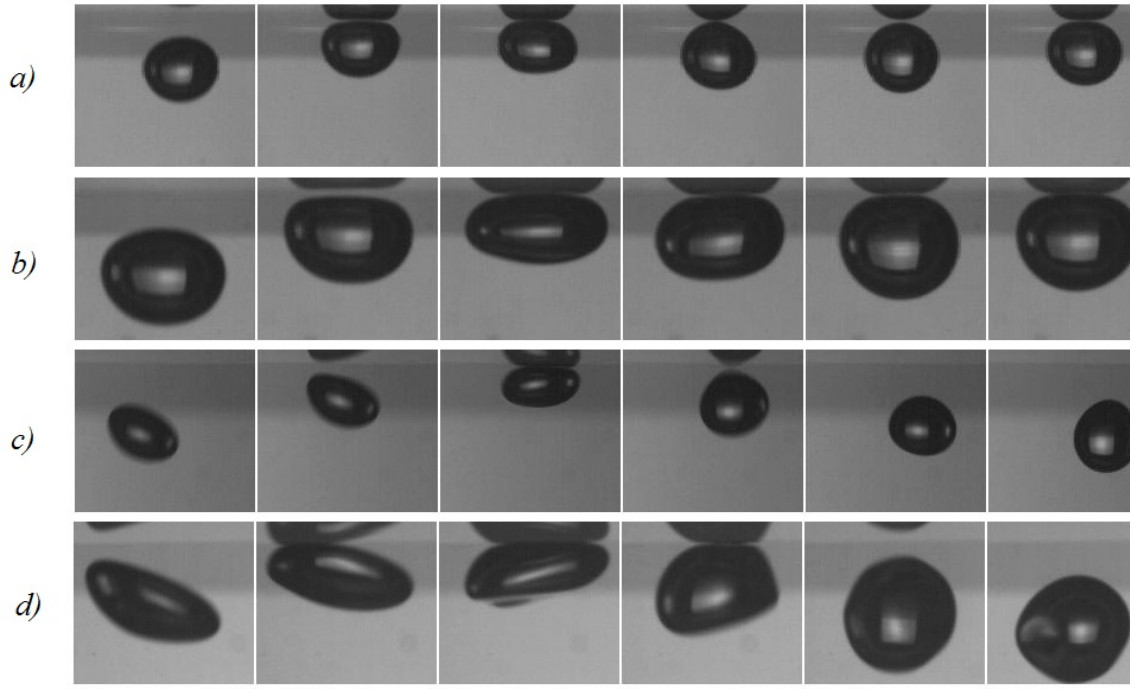

Figure 4.10 Sequence of image from which Fig. 4.9 graphs were extracted. All images share the same spatial scale but time scale is variable to illustrate the bounce.

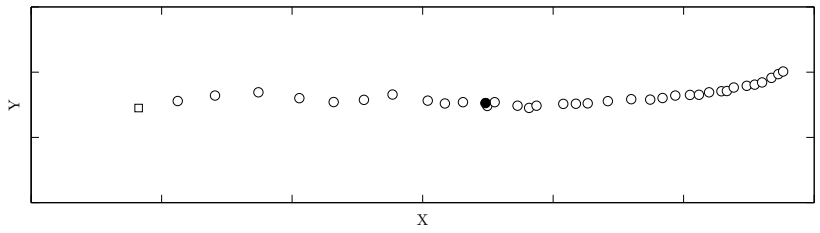

Figure 4.11 Projection of the bubble position in the $x-y$ plane from $t(z = 2r_b)$ and later. Square is initial state. Solid circle is the moment of maximum compression.

Location at ejection

Fig. 4.12 shows the location of the bubble centers at ejection as a function of the bubble radius. Slow bubbles are on or below the $z_f = r_b$ line and the fast bubbles are above. The relation best fitting the slow and fast bubbles are given by Eq. (4.7) and Eq. (4.8). The relations could have been given in terms of the Eötvös number ($\rho g r_b/\sigma$). But as r_b was varied on a small range, the dimensional form r_b was preferred.

$$z_f^{\text{slow}} = r_b - 0.10 r_b^2; \tag{4.7}$$

$$z_f^{\text{fast}} = r_b + 0.17 r_b^2; \tag{4.8}$$

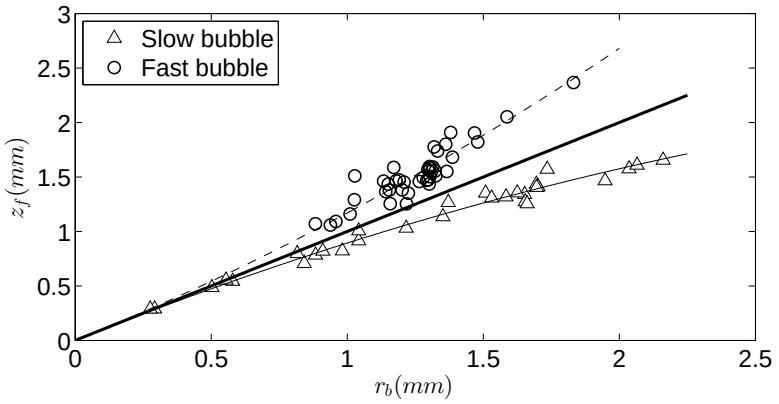

Figure 4.12 Distance from center of bubble to wall at ejection. (○) and (△) this study ; Thick black is ($z_f = r_b$) ; (−−) is Eq. (4.8) ; (–) is Eq. (4.7).

Aspect ratio at ejection

Fig. 4.13 shows the aspect ratio χ_f at ejection as a function of the initial deformation χ_o. Eq. (4.9) and Eq.(4.10) are fits for slow and fast bubbles respectively .

$$\chi_f^{\text{slow}} = 1 + 1.62(\chi_o - 1); \tag{4.9}$$

$$\chi_f^{\text{fast}} = 1.02; \tag{4.10}$$

Aspect ratio velocity at ejection

Fig. 4.14 shows the χ velocity at ejection as a function of the initial compression. Note that the velocity was rendered dimensionless by multiplying by the characteristic time r_b/v_{zo}. Eq. (4.11) and Eq. (4.12) are fits for slow and fast bubbles respectively.

$$\dot{\chi}_f^{\text{slow}} = -\frac{v_{zo}}{r_b}(7\chi_o - 6.35) \tag{4.11}$$

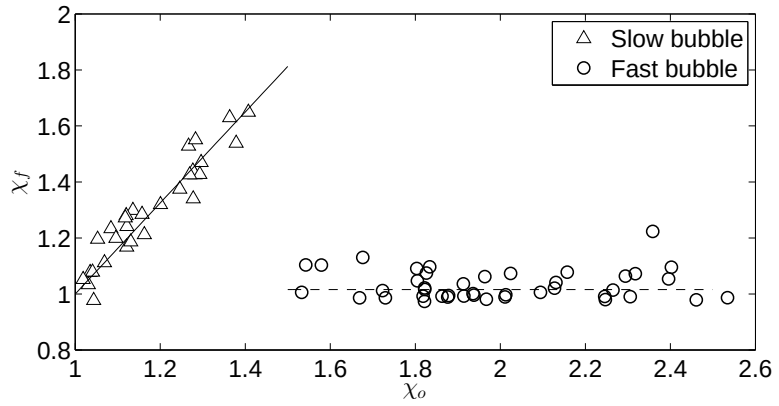

Figure 4.13 Aspect ratio of the bubble at ejection (○) and (△) this study ; (−−) is Eq. (4.10) ; solid is Eq. (4.9).

$$\dot{\chi}_f^{\text{fast}} = -\frac{v_{zo}}{r_b}(0.56) \tag{4.12}$$

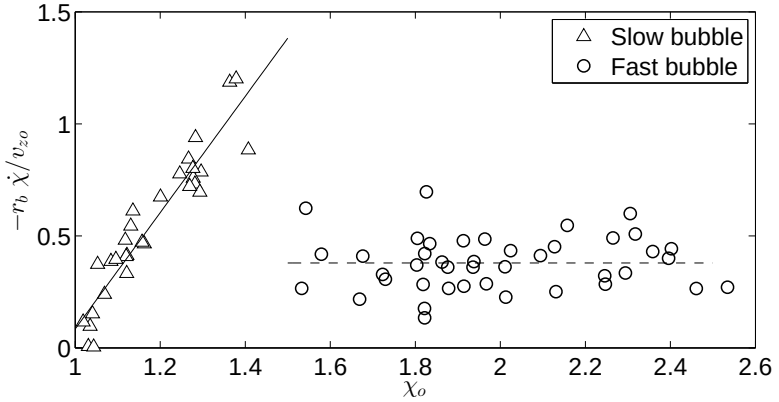

Figure 4.14 Aspect ratio velocity at ejection. (○) and (△) this study ; (−−) is Eq. (4.12) ; (–) is Eq. (4.11).

Normal restitution coefficient

Fig. 4.15 presents the z restitution coefficient (ε_Z) as a function of the initial aspect ratio (left) and as a function of initial velocity (right). The restitution coefficient is calculated as v_{zf}/v_{zo} . Eq. (4.13) is the fit for the left figure.

$$\varepsilon_z = 0.73\left\{1 - \exp\left[-2.69\left(\chi_o - 1\right)\right]\right\} \tag{4.13}$$

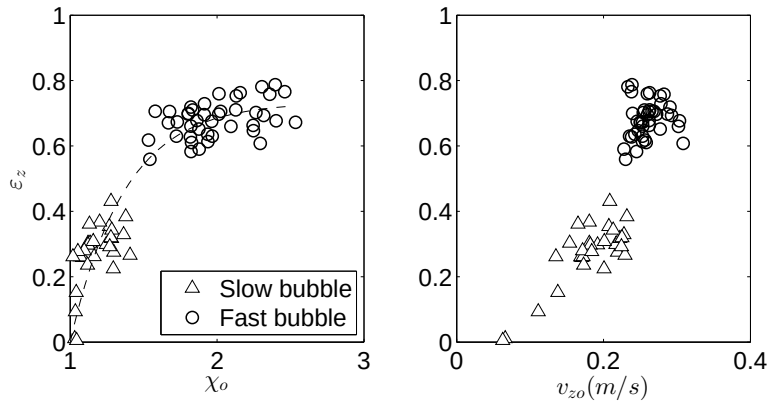

Figure 4.15 Normal restitution coefficient ;(○) and (△) this study ; (−−) is Eq. (4.13) ;

Tangential restitution coefficient

Fig. 4.16 presents the tangential restitution coefficient, in the r direction, as a function of the initial radial velocity. The restitution coefficient is calculated as v_{rf}/v_{ro}. Note that the restitution coefficient determined for small initial radial velocities are subjected to large uncertainties due to error propagation. As the radial velocity increases, the restitution coefficient seems to converge to a constant value of ε_r (Eq. (4.14)).

$$\varepsilon_r = 0.55 \tag{4.14}$$

Time interval

Fig. 4.17 shows the time interval between initial and final states as a function of initial deformation. Time was made dimensionless by dividing by the characteristic time r_b/v_z (Zenit and Legendre, 2009). Note that the uppermost point for slow bubble is the largest bubble with r_b =2.2 mm. Eq. (4.15) fits the experimental results.

$$\tilde{t}_f - \tilde{t}_o = 2 + 1.84\ \left(\chi_o - 1\right)^{1/3} \tag{4.15}$$

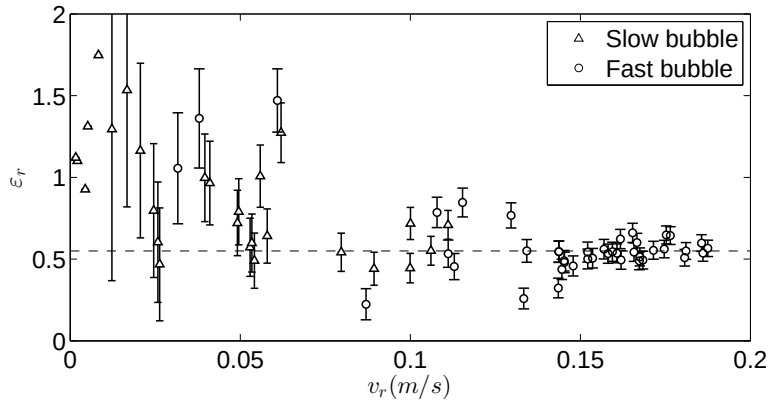

Figure 4.16 Tangential restitution coefficient ; (○) and (△) this study ; (−−) is Eq. (4.14).

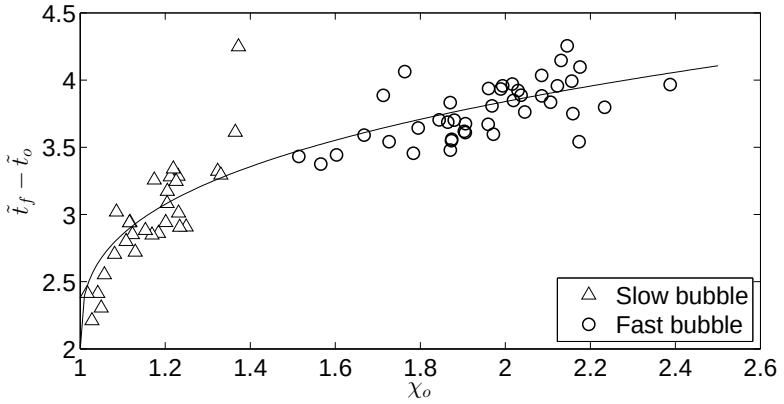

Figure 4.17 dimensionless time interval between initial and final state (○) and (△) this study ; (–) is Eq. (4.15).

Note on the angle dependency

It is surprising that the angle of approach does not demonstrate any correlations with previous parameters. Only ε_z seems to present a slight dependency on the initial angle and solely for fast bubbles. This effect might be attributed to the terminal rise velocity which is also affected by this angle. Indeed, our data reveals that the velocity magnitude is constant. Ellingsen and Risso (2001) arrived at the same observation. In other words, the more inclined the bubble trajectory is, the slower is the rise velocity. As it can be seen from the right side of Fig. 4.15, the terminal rise velocity has a significant effect on the restitution coefficient. Therefore, the angle of contact is not considered significant in the analysis of the rebound.

On the other hand, the angle of approach do have an influence on the radial displacement between the initial and the final states. From the previous relations, it is possible to estimate this radial displacement (Δr). First, let us assume that the bubble approaches the wall without deceleration. The dimensionless time at contact is therefore $\tilde{t} = 2$. For $\tilde{t} < 2$, the radial velocity is v_{ro}. For the remaining of the time of contact ($2 < \tilde{t} < \tilde{t}_f$), the radial velocity is assumed to be $0.55 v_{ro}$ (see Eq. (4.15)). Altogether, the total radial displacement is written as Eq. (4.16).

$$\frac{\Delta r}{r_b} = \left[2 + (\chi_o - 1)^{1/3}\right] \tan(\theta) \tag{4.16}$$

where $\tan(\theta) = v_{ro}/v_{zo}$. Fig. 4.18 illustrates this relation calculated with experimental χ_o and θ. Eq. (4.16) is adequately representing the radial displacement on the full range of approach angles.

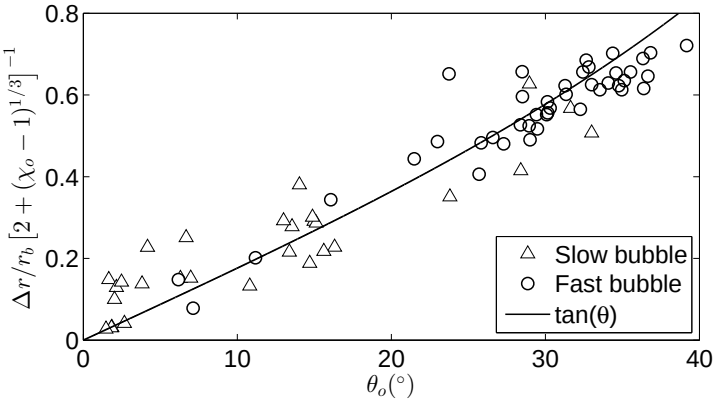

Figure 4.18 Radial displacement of the bubble as a function of the angle of approach.

4.5.2 Discussion

As it can be seen from the previous sections, there is a clear distinction between slow and fast bubbles. Indeed, terminal velocities, aspect ratios and bouncings all behave differently. For small radius bubbles, one could argue that the difference in bounce behavior stems from the difference in rise velocity. But in the limits of large r_b, both bubble types converge to the same terminal velocity yet the bounce behavior is still radically different. The aspect ratio might therefore be at the origin of the discrepancies. It is easily understood by considering the energy stored in the surface deformation. Under the assumption of a perfect ellipsoidal shape and by using Klaseboer *et al.* (2001) relation for added mass coefficient C_M , the kinetic energy can be calculated as $E_k = 1/2 C_M(\chi) V_b \rho v_z^2$ with V_b the bubble volume. The surface

deformation energy can be calculated as $E_S = \sigma S$, where σ is the surface tension (0.072 N/m) and S the bubble surface area. For instance, a slow and a fast bubble of $r_b = 2$mm will have aspect ratio of 1.3 and 2.4 and a terminal rise velocity of approximately $v_z = 23$ cm/s. The fast bubble has twice the kinetic energy and ten times the surface deformation energy of the slow bubble. For the fast bubble, the surface tension energy represents one third of the total energy. Altogether, there is 2.7 times more energy in the fast bubble than in the slow bubble available to propulse the bubble away from the wall.

4.5.3 Comparison with other works

Legendre *et al.* (2005) studied drops impacting an horizontal wall. They developed a theoretical framework to determine the functional dependency of the restitution coefficient ε_z by considering bubbles as a damped harmonic oscillators. They defined ε_z as the ratio of the departure velocity (loss of contact point) over the terminal rise velocity. Restitution coefficients were found to follow the relation :

$$\varepsilon_z = \exp(-\beta_1/St^*) \tag{4.17}$$

where St^* is the modified Stokes number :

$$St^* = 2\rho C_M r_b v_z/(9\mu) \tag{4.18}$$

and $C_M = C_M(\chi)$ is the added mass coefficient given by Klaseboer *et al.* (2001).

The relation was later on compared to experiments of air-bubble impact by Zenit and Legendre (2009). The functional dependence to St^* was found out to be satisfied with $\beta_1 = 3.5$. Fig. 4.19 shows the results from the present study compared with those obtained by Zenit and Legendre (2009). Our data for fast bubbles are in agreement with their experiments and with Legendre *et al.* (2005) functional dependence . It seems that even though the bubbles depict oscillatory motions, the coefficient of restitution still follows the same trend. Also, the scatter in our values for fast bubbles is comparable to the scatter of rectilinear bubbles. Since the trajectory types are attributed to the configuration of the bubble wake. This suggests that the interaction of the wake with the rebound dynamic is not significant. The trajectory motion of the bubble could be omitted to describe the impact.

However, the coefficients of restitution for slow bubbles do not fit the suggested relation. Since data were collected on a limited Stokes number range, no further comparison will be made.

Zenit and Legendre (2009) suggested that the functional dependence could be described

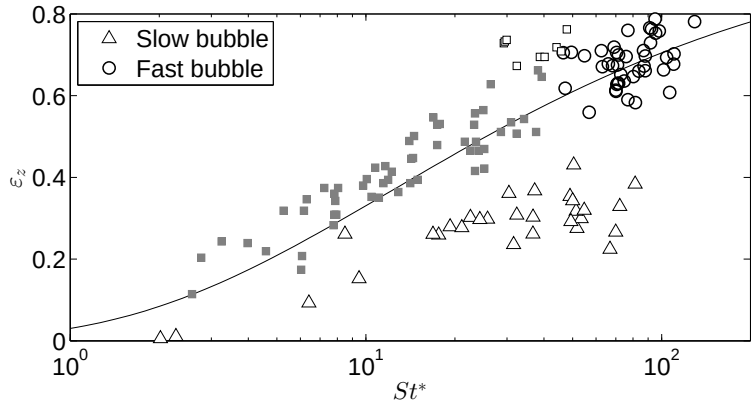

Figure 4.19 Restitution coefficient ; (○) and (△) this study ; (■) and (□) rectilinear and oscillatory path from Zenit and Legendre (2009) ; Solid line is Eq. (4.17).

by

$$\varepsilon_z = \exp\left(-\beta_2\sqrt{\frac{Ca}{St^*}}\right) \tag{4.19}$$

where Ca is the capillary number ($Ca = \mu v_z/\sigma$) and $\beta_2 = 30$. Fig. 4.20 presents our data and Zenit data as well as Eq. (4.19). Although the dependence in St^* fits our fast bubbles dataset, this new dependence in Ca/St^* does not.

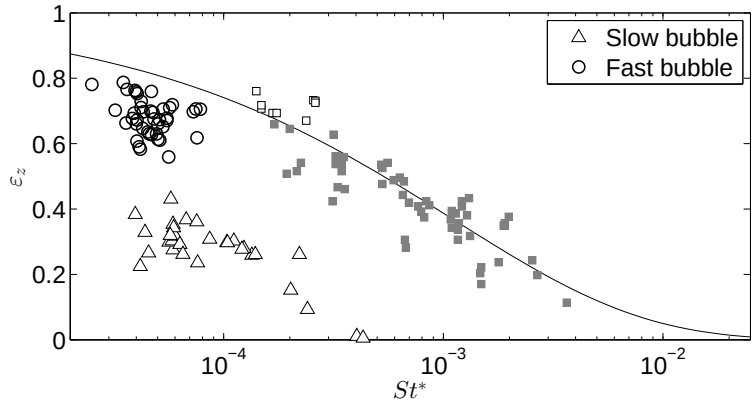

Figure 4.20 Restitution coefficient ; (○) and (△) this study ; (■) and (□) rectilinear and oscillatory from Zenit and Legendre (2009) ; Solid line is Eq. (4.19).

4.6 Collision with an inclined wall

Finally, the impacts of a few oscillatory bubbles with a rigid wall at an angle of 60° with the horizontal were studied. Due to the oscillatory motion, the impact dynamic is more difficult to quantify. In the approach stage, it is almost impossible to distinguish the influence of the wall from that of the oscillatory motion. Even very close to the wall, the oscillatory forces dominate the wall force and the previous definition on initial state cannot be used. For instance, a bubble at a perpendicular distance of $2r_b$ from the wall might or might not touch the wall depending on the evolution of the oscillatory motion. Therefore, we could not generate a database large enough to take into account each and every parameter of the impact with oscillatory bubbles.

Nonetheless, generic comments can be made regarding the behavior of slow and fast bubbles. As already described by other authors (Tsao and Koch, 1997; Podvin *et al.*, 2008), bubbles can either exhibit a repeated bouncing or a bounce-and-slide motion. Those two phenomena are illustrated in Fig. 4.21.

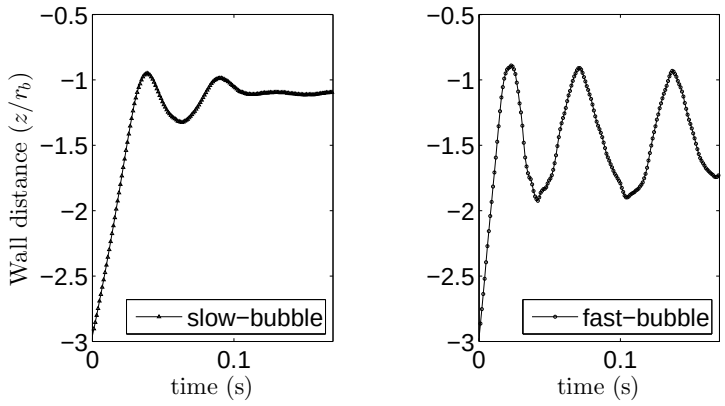

Figure 4.21 Distance from the wall for a 1.25mm bubble at impact with a 60° wall for slow (left) and fast bubble (right).

Tsao and Koch varied the angle of the wall for bubbles with equivalent radii of 0.5-0.7mm. It was found that for inclination greater than 55°, bubbles started to exhibit repeated bouncing (Tsao and Koch, 1997). This critical angle can also be seen in terms of normal-velocity Weber number ($We_\perp$). They expected that for bubbles with $We_\perp$ >0.4 , repeated bouncing would be observed. Also, the onset angle would be smaller as the bubble diameter increases. Podvin *et al.* (2008) did a similar study with a range of bubble radii slightly larger : 0.65-0.7mm. The critical angle was found to be between 50-60° in agreement with Tsao and Koch (1997).

In our experiments, fast bubbles had radii in the range 1.15-1.25mm while slow bubbles ranged from 0.7-1.45mm. Figure 4.21 presents the normal distance from the bubble centers to the wall for slow and fast bubbles of equal radii (left and right sides respectively). $We_{\perp}$ number values are of 0.24 and 0.71 (left and right sides respectively). This is in agreement with Tsao's expectation regarding the onset of repeated bouncing for $We_{\perp} > 0.4$. Also, note that both bubbles approached the wall almost vertically.

The behavior on the first bounce for both bubble types is similar to those illustrated in Fig. 4.10. Slow bubbles compress and bounce with a nearly spherical shape and are then rapidly damped thus inducing the sliding motion as obserbed by Tsao and Koch (1997). For fast bubbles, a rigid body rotation combined with sliding is observed upon contact with the wall. Then, the bubble leaves the wall with a nearly spherical shape. After a variable number of transient bounces, repeated bouncing motion settles.

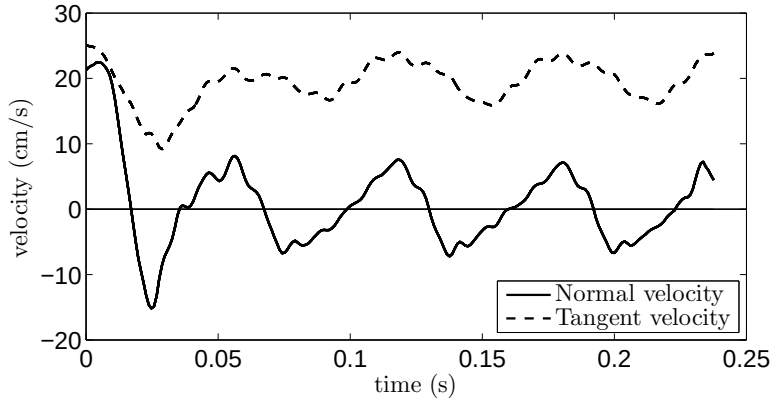

Figure 4.22 Normal and tangent component of the velocity during the collision of a fast bubble with an inclined wall r_b = 1.14mm, $We_{\perp}$ = 1.4, χ_o = 2.15 .

Repeated bounces differ slightly from the first one mainly in the approach velocity and contact angle. Fig. 4.22 shows the normal and tangent components of the velocity relative to the wall. As expected, the velocity at impact is constant for every bounce following the first. Fig. 4.23 shows the first and the third bounce for a given bubble on steady bouncing motion. Left and right columns show the left and front views of the same bubble. On the first impact, the left view shows the bubble great axis rotating around its center before ejection. Note that the bubble was compressed throughout this rotation process in an oblate ellipsoidal shape. Now let's consider the third impact, once the great axis starts to rotate about its center, the projection of the bubble in the left view becomes almost spherical. Yet in the front view, it is still an oblate ellipsoid. The only way to have those two projections simultaneously is to

have a prolate ellipsoid with its major axis perpendicular to the left view. This observation was repeatable through all our experiments.

An hypothesis that would explain this behavior is that the slip condition on the surface is not satisfied. Therefore, the interface in contact with the liquid film between the bubble and the wall would be immobile thus inducing a *rolling effect*. The inertia of the bubble would then create the prolate ellipsoid observed. While it might not be evident by looking at still images, the animated sequence supports this *rolling* mechanism. This explanation of the phenomenon is also in agreement with Podvin *et al.* (2008) hypothesis on the no-slip condition on the bubble for collisions with an inclined wall. Note that this phenomenon is only observed upon contact with fast bubbles. Slow bubbles show almost spherical shapes and appear to slide on the wall.

4.7 Conclusion

In agreement with Peters and Els (2012), bubbles behaved in two ways : slow and fast bubbles. Results show that both bubble categories could exhibit zig-zag or helical trajectories. A detailed study of the generation of the bubble with a broader window would be needed to deepen the understanding of this behavior. Especially, it would be interesting to identify if the helical slow bubble motion is stable or if it is a precursor to fast bubble with helical motion.

A set of restitution relations was given for these two categories of bubbles impacting a wall. Two conclusions are drawn. First, fast bubbles describing oscillatory motion follow the Stokes functional dependence as proposed by Zenit *et al.* for rectilinear bubbles. Second, the aspect ratio before impact is the key driver of the rebound process. Slow bubbles, having a low aspect ratio prior to impact, demonstrated almost no bounce in contrast with fast bubbles.

Also, a qualitative analysis of the impacts of slow and fast bubbles with an inclined wall at 60° was presented. Results show that for the studied range of radii, all slow bubbles showed the sliding motion as the fast bubbles exhibited the repeated bouncing motion. More importantly, results show that in steady bouncing motion, upon contact, the bubble takes a prolate shape. This suggests that the bubble *rolls* against the wall.

Acknowledgments

This work was sponsored by the Natural Sciences and Engineering Research Council, Babcock & Wilcox Canada and Atomic Energy of Canada Ltd., through the BWC/AECL/NSERC research chair in fluid-structure interactions.

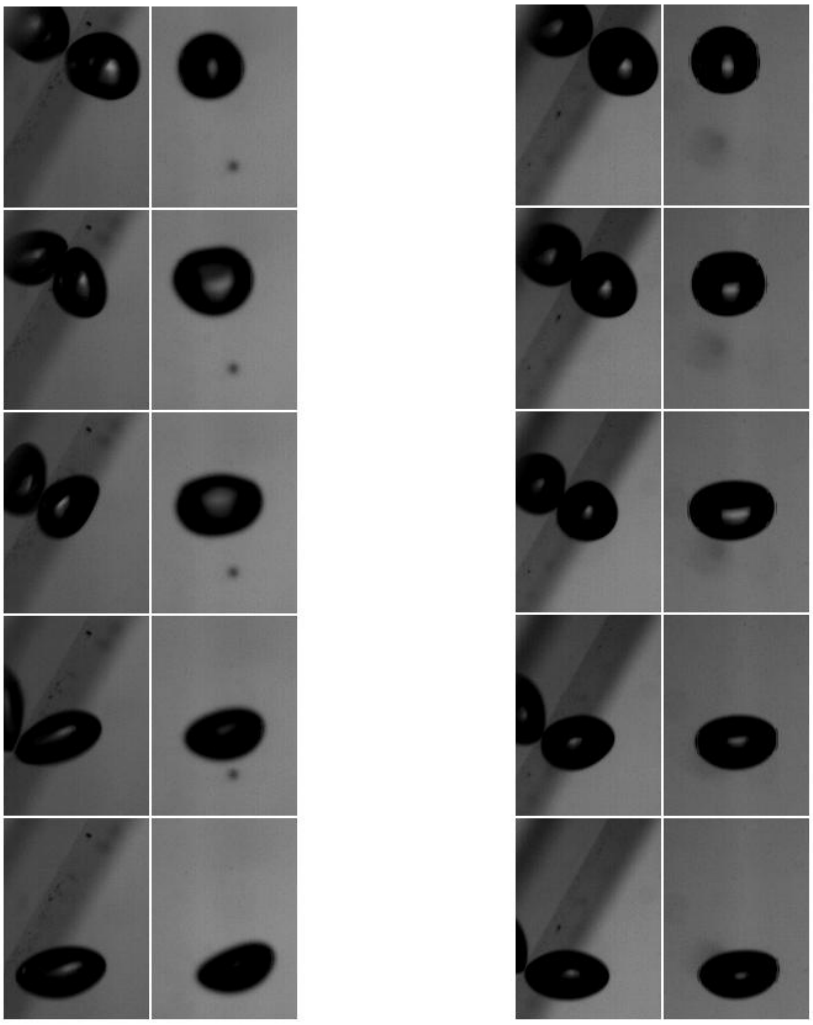

(a) First impact.

(b) Third impact.

Figure 4.23 Left and Front view of an impact with an inclined wall. Time evolution is directed bottom-up. 5ms separate each pair of images. r_b = 1.23mm, $We_\perp$ = 0.71, χ_o = 1.95

References

CANOT, E., DAVOUST, L., EL HAMMOUMI, M. and LACHKAR, D. (2003). Numerical simulation of the buoyancy-driven bouncing of a 2-d bubble at a horizontal wall. *Theoretical and Computational Fluid Dynamics*, 17, 51–72.

CLIFT, ROLAND, G. J. R. and WEBER, M. E. (1978). *Bubbles, drops, and particles*. Academic press, New York.

ELLINGSEN, K. and RISSO, F. (2001). On the rise of an ellipsoidal bubble in water : oscillatory paths and liquid-induced velocity. *Journal of Fluid Mechanics*, 440, 235–268.

KLASEBOER, E., CHEVAILLIER, J.-P., MATÉ, A., MASBERNAT, O. and GOURDON, C. (2001). Model and experiments of a drop impinging on an immersed wall. *Physics of Fluids*, 13.

KUSHCH, V. I., SANGANI, A. S., SPELT, P. D. and KOCH, D. L. (2002). Finite-weber-number motion of bubbles through a nearly inviscid liquid. *Journal of Fluid Mechanics*, 460, 241–280.

LEGENDRE, D., DANIEL, C. and GUIRAUD, P. (2005). Experimental study of a drop bouncing on a wall in a liquid. *Physics of Fluids*, 17, 97105.

LEGENDRE, D., ZENIT, R. and VELEZ-CORDERO, J. R. (2012). On the deformation of gas bubbles in liquids. *Physics of Fluids*, 24, –.

MOORE, D. W. (1965). The velocity of rise of distorted gas bubbles in a liquid of small viscosity. *Journal of Fluid Mechanics*, 23, 749–766.

MORAGA, F.J., S. C. and R.T. LAHEY, J. (2005). Modeling wall induced forces on bubbles for inclined walls. *Multiphase Science and Technology*, 17, 483–505.

PETERS, F. and ELS, C. (2012). An experimental study on slow and fast bubbles in tap water. *Chemical Engineering Science*, 82, 194–199.

PODVIN, B., KHOJA, S., MORAGA, F. and ATTINGER, D. (2008). Model and experimental visualizations of the interaction of a bubble with an inclined wall. *Chemical Engineering Science*, 63, 1914 – 1928.

TOMIYAMA, A., CELATA, G., HOSOKAWA, S. and YOSHIDA, S. (2002). Terminal velocity of single bubbles in surface tension force dominant regime. *International Journal of Multiphase Flow*, 28, 1497 – 1519.

TSAO, H. and KOCH, D. L. (1997). Observations of high reynolds number bubbles interacting with a rigid wall. *Physics of Fluids*, 9.

WU, M. and GHARIB, M. (2002). Experimental studies on the shape and path of small air bubbles rising in clean water. *Physics of Fluids*, 14, L49.

ZENIT, R. and LEGENDRE, D. (2009). The coefficient of restitution for air bubbles colliding against solid walls in viscous liquids. *Physics of Fluids*, 21.

CHAPITRE 5

ARTICLE 3 : MODELLING OF BUBBLE-WALL COLLISION

Afin de rendre compte des observations expérimentales sur la dynamique d'impact des bulles sur un mur, un modèle théorique a été créé. Le prochain article décrit les éléments de ce modèle. Les prédictions du modèle sont ensuite comparées avec les résultats expérimentaux du chapitre précédent.

Soumis pour publication dans : *Physics of Fluid*

É. PELLETIER, C. BÉGUIN & S. ÉTIENNE
BWC/AECL/NSERC Chair of Fluid-Structure Interaction
Department of Mechanical Engineering, École Polytechnique,
P.O.Box 6079, succ. Centre-Ville, Montréal (Québec), Canada, H3C 3A7

A model for bubble-wall interaction is developed assuming that the bubble shape is a revolution ellipsoid of constant volume. Two degrees of freedom are considered : distance from the wall and aspect ratio. Forces acting on the bubble are derived from the potential flow theory. Regression relations are calculated for the added mass and the drag coefficients as a function of both degrees of freedom. The model is then compared to experimental impacts of air bubble (0.5 to 4.4 mm diameter) on a rigid wall in tap water. Experimental data contains 30 impacts of slow bubbles and 42 impacts of fast bubbles.

Nomenclature

a	: Small axis of the bubble [m]	z_b	: Center of the bubble position [m]
χ	: Aspect ratio of the bubble	r_b	: Equivalent radius of a bubble [m]
ρ_g	: Density of the gas phase [kg/m^3]	ρ_ℓ	: Density of the liquid phase [kg/m^3]
V_b	: Volume of a bubble [m^3]	$\mathbf{v}$	: Interface element velocity [m/s]
C_M	: Added mass coefficeint	$\mathbf{u}$	: Flow velocity [m/s]
C_D	: Drag coefficeint	C_J	: Jet coefficeint
Re_z	: z_b-Reynolds number ($2r_b\rho_\ell\dot{z}_b/\mu$)	Re_a	: a-Reynolds number ($2r_b\rho_\ell\dot{a}/\mu$)
We_z	: z_b-Weber number ($2r_b\rho_\ell\dot{z}_b^2/\sigma$)	We	: Weber numberr ($2r_b\rho_\ell\mathbf{v_b^2}/\sigma$)
A_b	: Cross-section area of the equivalent spherical bubble (πr_b^2) [m^2]		

Values with $_o$ and $_f$ subscripts relate to specific instants before and after impact respectively.

5.1 Introduction

Two phase flows are present in many industrial applications such as steam generators, heat exchangers and chemical reactors. At some point in these processes the flow will take a bubbly structure. In an effort to create a numerical model for these flows, a Lagrangian formalism can be used to describe the motion of each bubble. The computational power required to perform the simulations increases with number of bubbles. For example, the amount of computations increases quadratically if you consider all bubble-bubble interactions. Thus, it is important that the model describing the motions of bubble be efficient. This paper focuses on the efficient modelling of bubbles impacting walls.

Different approaches are reported in the literature to model this phenomenon. The simplest of them was developed by Legendre *et al.* (2005) to characterize the restitution coefficient of drops in liquid . Their method was to consider the bubbles as damped harmonic oscillators and to describe the rebound velocity as a function of initial conditions. The technique was then applied to air bubbles in water by Zenit and Legendre (2009). This method only deals with a part of the motion however it gives a clear understanding of the controlling mechanism.

Klaseboer *et al.* (2001) introduced a more complete model by coupling the drainage pressure in the film between a deformable bubble and the wall to a Lagragian description of the bubble motion . As it leads to good agreement when compared to experiments, the method was extended to inclined walls by Moraga and R.T. Lahey (2005) and later by Podvin *et al.* (2008) . Again, up to inclination angles of $60°$, the agreement with experiments was good. This technique is suited to describe the approach motion, rebound and eventually immobilization. It is computationally expensive since drainage flow, interface deformation and bubble

motion have to be calculated at each time step.

Down the road of complexity, other authors solved the entire flow around deformable bubbles under some simplifying assumptions. For instance, Canot *et al.* (2003) solved an irrotational flow by the boundary element method. No-slip condition on the interface was prescribed and a 2D geometry was assumed. Kushch *et al.* (2002) solved the potential flow around the bubble using ellipsoidal harmonics . Drainage pressure was added as a force on the bubble center and slip condition was prescribed on the interface. Although both methods present comparable results with experiments, they are not computationally efficient for clouds of bubbles and they do not give insight about the control mechanism.

In this study, the potential flow around a partially deformable bubble was considered. The bubble is assumed tobe a deformable revolution ellipsoid of constant volume. A set of flow configurations are solved prior to the simulation. From these flows are extracted regression relations for forces acting on the bubble. Simulations are then compared to experimental results. It will be shown that this model can predict the restitution coefficient of slow and fast bubbles.

5.2 Flow resolution

5.2.1 Definition of the problem

The bubble is considered to be a revolution ellipsoid of constant volume with small axis a and great axis $a\chi$. The equivalent radius r_b is defined as the radius of the sphere having the same volume as the ellipsoidal bubble ($r_b^3 = a^3\chi^2$). The distance from the wall to the closest apex of the bubble is given by the parameter d as illustrated in Fig. 5.1 and is defined as a positive quantity.

As mentioned previously, the flow is considered to be inviscid and irrotational. Under these assumptions, the flow around the bubble can be extracted from the potential function Φ which is solution of Eq. (5.1) and satisfies appropriate boundary conditions.

$$\nabla^2\Phi = 0 \tag{5.1}$$

Two boundary conditions are prescribed. First, a no shear stress condition on the interface of the bubble is assumed. This condition, namely the slip condition, is represented by Eq. (5.2) where $\mathbf{u}$ is the flow velocity, $\mathbf{v}$ the interface velocity and $\mathbf{n}$ its normal vector directed outward.

$$\mathbf{u}\cdot\hat{\mathbf{n}} = \mathbf{v}\cdot\hat{\mathbf{n}} \qquad \text{where } \mathbf{u} = \nabla\Phi \tag{5.2}$$

The interface velocity will be defined by the motion type. In the model, two motion types

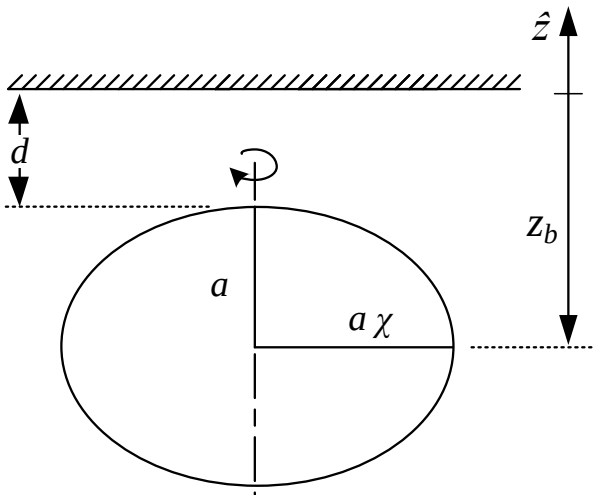

Figure 5.1 Geomerical definition of the problem.

are considered : translation and compression. Translation is a solid body motion in the direction of the small axis. Compression is defined as a modification of χ along with a modification of a to preserve the volume. The boundary condition on the translation mode is given by $\mathbf{v} = \dot{z}_b\hat{\mathbf{z}}$ where $\dot{z}_b$ is the velocity of the center of the bubble. It has a constant value everywhere on the surface of the bubble. The boundary condition associated with the compression mode is less trivial. The exact derivation is given in the work by van Wijngaarden and Veldhuis (2008). Equations (5.3a) and (5.3b) show these boundary conditions. ζ represents the height of a surface element relative to the center equatorial plane of the bubble and $\dot{a}$ the velocity of the uppermost apex relative to the velocity of the center of mass $\dot{z}_b$.

$$\mathbf{u}\cdot\hat{\mathbf{n}} = \dot{\mathbf{z}}_\mathbf{b}\cdot\hat{\mathbf{n}} \qquad \text{Translation mode} \qquad (5.3a)$$

$$\mathbf{u}\cdot\hat{\mathbf{n}} = \dot{a}\frac{\chi\left(3\zeta^2/a^2-1\right)}{2\left[1+\left(\chi^2-1\right)\zeta^2/a^2\right]^{1/2}} = \dot{a}\beta \qquad \text{Compression mode} \qquad (5.3b)$$

In order to take into account the presence of the wall, a virtual bubble is used similarly to Milne-Thomson (1968). Both bubbles are symmetrically located on a line perpendicular to the desired wall. With respect to that wall, velocities are also symmetrical. This geometry ensures a no-penetration condition through the symmetry plane thus creating a wall with an implicit slip condition.

5.2.2 Resolution

This sectionl focuses on the resolution of the flow around the bubble. Solution of Eq. (5.1) in spherical coordinates is assumed to be in the form of

$$\Phi = \sum_{k}^{2} \sum_{\ell,m} g_{\ell,m}^{k} S_{\ell,m}^{k}(\mathbf{r_k}) \tag{5.4}$$

where $S_{\ell,m}^{k}(\mathbf{r})$ is the solid harmonic function of mode ℓ, m in the reference frame of bubble k and $g_{\ell,m}^{k}$ is its associated coefficient that has to be determined. Index k refers to the real bubble when $k = 1$ and to the virtual bubble when $k = 2$. The solid harmonic functions are defined as

$$S_{\ell,m}^{k}(\mathbf{r}) = S_{\ell,m}^{k}(r,\theta,\varphi) = \frac{(-1)^{\frac{m+|m|}{2}}}{r^{\ell+1}} \sqrt{\frac{(\ell-m)!}{(\ell+m)!}} P_{\ell}^{m}(cos(\theta)) e^{im\varphi} \tag{5.5}$$

Due to the azimuthal symmetry of the system, only modes $S_{\ell,0}^{k}$ contribute to the description of the flow. m indices will therefore be dropped. Assuming a limited number of spherical hamonics, the boundary condition given by Eq. (5.2) can be rewritten as

$$\sum_{k=1}^{2} \sum_{\ell=0}^{L} g_{\ell}^{k} (\underbrace{\nabla S_{\ell}^{k}(\mathbf{r})}_{\mathbf{u_{\ell}^{k}(r)}} \cdot \hat{\mathbf{n}}) = \mathbf{v} \cdot \hat{\mathbf{n}} \tag{5.6}$$

In Eq. (5.6) was introduced the velocity vector $\mathbf{u_{\ell}^{k}}$ induced by the mode ℓ of bubble n at position $\mathbf{r}$ in the reference frame of bubble k.

Since the orthogonality of spherical harmonics can only be used on spheres, no analytic solutions can be found on the surface of an ellipsoidal bubble. In order to find an approximate solution for the g_{ℓ}^{k} coefficients, L points on the polar arc of the surface were chosen upon which is enforced compliance with the boundary conditions (see Fig. 5.2). S and S' are the source points of the harmonic functions for the real and virtual bubble. p_i and p_i' are the enforcement points of the boundary conditions on the real and virtual bubble. Eq. (5.6) can be written for the evaluation point i as

$$\sum_{k=1}^{2} \sum_{\ell=0}^{L} g_{\ell}^{k} \left(\mathbf{u_{\ell}^{k}} \left(\mathbf{r_{k}^{i}} \right) \cdot \hat{\mathbf{n}}_{\mathbf{i}} \right) = \mathbf{v_i} \cdot \hat{\mathbf{n}}_{\mathbf{i}} \tag{5.7}$$

Symmetry of the problem yields

$$\mathbf{u_{\ell}^{1}}(\mathbf{p_i'}) \cdot \hat{\mathbf{n}}_{\mathbf{i}}' = \mathbf{u_{\ell}^{2}}(\mathbf{p_i}) \cdot \hat{\mathbf{n}}_{\mathbf{i}} \tag{5.8}$$

$$g_{\ell}^{2} = (-1)^{\ell} g_{\ell}^{1} \tag{5.9}$$

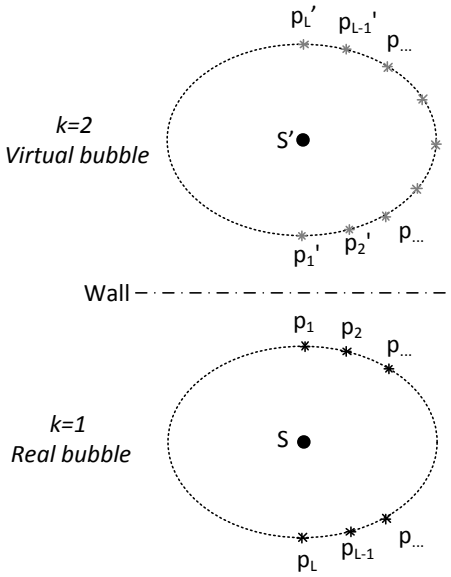

Figure 5.2 Scheme of the resolution approach.

Relations (5.8) and (5.9) state that to evaluate the g_ℓ^k coefficients, calculation from a single source term is sufficient. Eq. (5.7) becomes a linear system of L equations with g_ℓ^1 as the unknowns.

$$\sum_{i=1}^{L}\sum_{\ell=0}^{L} g_\ell^1 \left[\left(\mathbf{u_\ell^1}(\mathbf{p_i}) + (-1)^{\ell+1}\mathbf{u_\ell^1}(\mathbf{p_1'})\right)\cdot\hat{\mathbf{n}}_\mathbf{i}\right] = \sum_{i}^{L}\mathbf{v_i}\cdot\hat{\mathbf{n}}_\mathbf{i} \tag{5.10}$$

The numerical application is straightforward. The term in the bracket of Eq. (5.10) must be evaluated to fill the (i,ℓ) element of the coefficient matrix. The non-homogeneous vector is filled with the right-hand term of Eq. (5.10) and corresponds to the boundary condition on each node.

5.2.3 Note on the numerical application

The number of evaluation points is equal to the maximal order of harmonic functions used. This yields the only existing solution to the system. Unfortunately, this choice generates numerical issues. Since the harmonic functions vary as $|\mathbf{r}|^{-(\ell+1)}$, an ill-conditioned matrix is obtained when $|\mathbf{r}|$ is different from unity when L grows. Thus, a limited analysis is done for L=30 and $0.9 < \chi < 1.25$. All of the relations given in this article must be seen as a first order approximation around the spherical shape.

5.3 Force extraction

In the previous section, the resolution method for the flow was presented. This section focuses on the forces induced by the flow on the bubbles. It also serves as a validation of the algorithm by comparing to relations available in the literature. These forces are of two types : pressure and viscous.

5.3.1 Pressure Forces

Bernoulli unsteady equation states that the pressure in a potential flow can be calculated as

$$P = -\rho_\ell \frac{\partial \Phi}{\partial t} - \frac{1}{2}\rho_\ell \mathbf{u}^2 - \rho_\ell g z \tag{5.11}$$

Using the definition of total derivative as well as the chain rule, Eq. (5.11) yields

$$P = -\rho_\ell \left[\underbrace{\frac{\partial \Phi}{\partial \dot{z}_b}\ddot{z}_b + \frac{\partial \Phi}{\partial \dot{a}}\ddot{a}}_{A} + \underbrace{\frac{\partial \Phi}{\partial z_b}\dot{z}_b + \frac{\partial \Phi}{\partial a}\dot{a}}_{B} - \underbrace{\mathbf{u}\nabla\Phi + \frac{1}{2}(\nabla\Phi)^2}_{C} + \underbrace{gz}_{D} \right] \tag{5.12}$$

In Eq. (5.12), four terms on the right hand side are identified. The added mass term (A) is proportional to the acceleration. The jet term (B) is the reaction induced by the varying added mass. The third term is the dynamic pressure (C) and the last term is the usual buoyancy (D).

From linearity of the Laplace's equation (Eq. (1)), the potential function Φ can be obtained from the sum of the two functions associated to the translation and compression modes. Also, since the boundary conditions are linear with velocities $\dot{z}_b$ and $\dot{a}$, each mode can be defined as the product of this velocity with its associated normalized potential function. These functions, ϕ_z and ϕ_a, are solutions of the system with $\dot{z}_b$ and $\dot{a}$ taken as unity in Eq. (5.3) respectively. ϕ_z and ϕ_a depend only on the position and shape of the bubble. The general potential function is defined as

$$\Phi = \dot{z}_b \phi_z(a, z_b) + \dot{a}\phi_a(a, z_b) \tag{5.13}$$

Note that by substituting Eq. (5.13) into (5.12), coupled pressure terms between the translation and compression modes appear.

In the following sections, forces acting on each mode are detailled. Eq. (5.14a) and (5.14b)

are used to calculate these forces from the pressure relation. They are derived from a virtual work approach where the fluid pressure is projected on each mode.

$$F_z = -\int P\ \hat{\mathbf{n}} \cdot \hat{\mathbf{z}}\ dS \qquad \text{Translation mode} \qquad (5.14a)$$

$$F_a = -\int P\ \beta\ dS \qquad \text{Compression mode} \qquad (5.14b)$$

whith β defined in Eq. (5.3).

Added Mass - Validation

As traditionally formulated, the general added mass induced by q_2 on q_1 is

$$F_{Mq_1,q_2} = -\rho_\ell V_b C_{Mq_1,q_2} \ddot{q}_2 \qquad (5.15)$$

The added mass force is the result of the integration of the first two terms of Eq. (5.12). Our numerical approach gives comparable results with existing relations for C_M. Fig. 5.3(a) compares our solution to the analytical solution of Kok (1993) for a spherical bubble approaching a wall with a limited expansion of 5 terms. Both relations are in good agreement for large d and present a small drift as d approaches 0. This discrepancy stems from the limited number of terms used in the expansion. The series expansion containing 100 terms fits perfectly our calculations. Fig. 5.3(b) compares the added mass coefficient of an ellipsoidal bubble in translation mode to the results of Klaseboer *et al.* (2001). Note that the calculated results follow closely the exact solution given by (Klas.1). Relation (Klas.2) is the linearization calculated by Klaseboer *et al.* (2001)($C_{Mz,z} = 0.62\chi - 0.12$) .

Fig. 5.3(c) shows the points calculated for the added mass coefficient on the compression mode compared to the relation obtained from Kushch *et al.* (2002) ($C_{Ma,a} = 0.2\chi^{1.17}$). Again, a good agreement is found and results in a validation of the present approach.

Added mass - Relation

The previous section compared our results for added mass coefficients to those already published in the literature. The goal of this section is to extract regression relations to describe forces acting on z or a as a result of the acceleration in either of these two coordinates as a function of the shape of the bubble and its distance from the wall. We imposed that the regression formulas are the product of two independent functions. i.e. :

$$C_M(d, \chi) = D(d)X(\chi) \qquad (5.16)$$

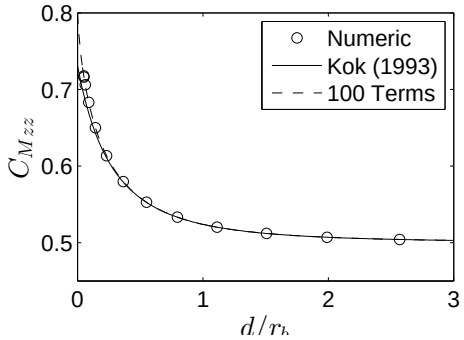

(a) Spherical bubble approaching a wall.

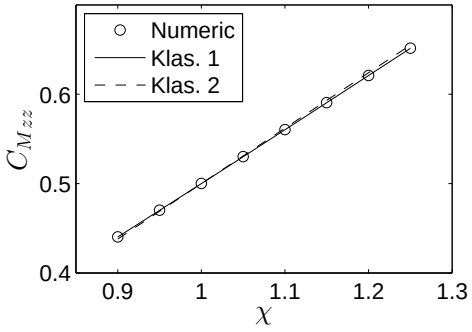

(b) Ellipsoidal bubble translating in unbounded fluid.

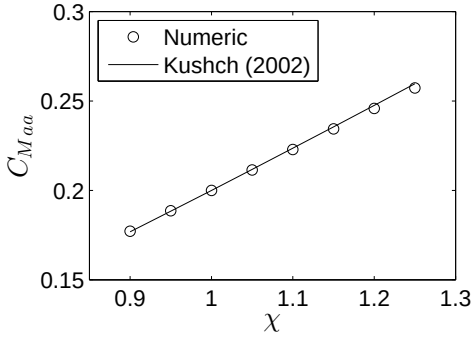

(c) Ellipsoidal bubble compressing in unbounded fluid.

Figure 5.3 Validation of approach for added mass coefficients.

Also, at each time relations were found in the literature, they were adopted when the accuracy was found acceptable. Under these assumptions, we constructed relations (5.17a), (5.17b) and (5.17c) for added mass coefficients.

$$C_{Mz,z} = (0.62\chi - 0.12)\left[1 + \frac{3}{8}\left(\frac{r_b}{h}\right)^3 + \frac{3}{64}\left(\frac{r_b}{h}\right)^6 + \frac{9}{256}\left(\frac{r_b}{h}\right)^8 + \frac{3}{512}\left(\frac{r_b}{h}\right)^9 + ...\right] \tag{5.17a}$$

$$C_{Ma,a} = \left(0.2\chi^{1.17}\right)\left[1 + \frac{1}{(d/r_b + 1.1)^{7.25}}\right] \tag{5.17b}$$

$$C_{Ma,z} = C_{Ma,z} = (0.035\chi - 0.016)\left[\frac{1}{(d/r_b + 0.5)^3}\right] \tag{5.17c}$$

where h is the dimensionless distance from the center of a *spherical* bubble to the wall as demonstrated by Kok (1993). With the present formalism, this translates to $h = d + 1$. As it can be observed on Fig. 5.4(a)-5.4(c), decomposing the coefficient function as a product of

two independent functions yields good results in the computed range of χ for all values of the distance d.

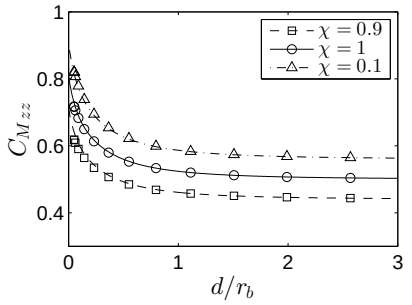

(a) Translation mode.

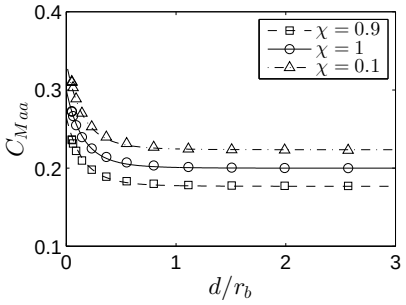

(b) Compression mode.

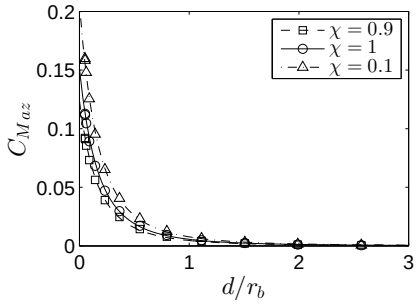

(c) Cross-coupling.

Figure 5.4 Regression (line) and calculated values (nodes) of added mass coefficients.

5.3.2 Jet force

As mentioned previously, the jet force is a result of the spatially varying added mass coefficient. To illustrate this, let us consider a simple case of a body of mass $m = m(z)$. The right way to describe the motion of the body is to use the conservation of momentum as presented in Eq. (5.18). The *jet force* of Eq. (5.11) is analogous to the last term of the right-hand side of Eq. (5.18). The only difference is that in our case, the mass depends on two coordinates (z_b, a).

$$\frac{d}{dt}(m\dot{z}) = \frac{dm}{dt}z + m\ddot{z} = \sum F \implies m\ddot{z} = \sum F \underbrace{-\frac{\partial m}{\partial z}\dot{z}^2}_{\text{Jet force}} \tag{5.18}$$

Substituting Eq. (5.13) in Eq. (5.11) and keeping only the terms relative to the jet force

yields

$$P_J = -\rho_\ell \left[\dot{z}_b^2 \frac{\partial \phi_z}{\partial z} + \dot{a}^2 \frac{\partial \phi_a}{\partial a} + \dot{z}_b \dot{a} \left(\frac{\partial \phi_z}{\partial a} + \frac{\partial \phi_a}{\partial z} \right) \right] \tag{5.19}$$

By integrating Eq. (5.19) over the surface of the bubble and defining the format of the resulting force as a traditional drag force, the jet force coefficient can be defined by Eq. (5.20).

$$F_{J q_1, q_2 q_3} = -\frac{1}{2} \rho_\ell \pi r_b^2 C_{J q_1, q_2 q_3} \; \dot{q}_2 \dot{q}_3 \tag{5.20}$$

where the force is applied on coordinate q_1 and is proportional to the product of coordinates $q_2 q_3$. For instance, $C_{Ja,az}$ would be the force coefficient on a as a result of the cross-coupling between a and z_b. After some manipulations, the jet coefficients can be expressed in terms of the added mass coefficients from Eqs. (5.17). Their expressions are listed in Eqs. (5.21).

$$C_{Jz,zz} = \frac{8}{3} \frac{\partial}{\partial z} C_{Mz,z} \tag{5.21a}$$

$$C_{Jz,aa} = \frac{8}{3} \frac{\partial}{\partial a} C_{Ma,z} \tag{5.21b}$$

$$C_{Ja,zz} = \frac{8}{3} \frac{\partial}{\partial z} C_{Ma,z} \tag{5.21c}$$

$$C_{Ja,aa} = \frac{8}{3} \frac{\partial}{\partial a} C_{Ma,a} \tag{5.21d}$$

$$C_{Jz,az} = \frac{8}{3} \left(\frac{\partial}{\partial z} C_{Ma,z} + \frac{\partial}{\partial a} C_{Mz,z} \right) \tag{5.21e}$$

$$C_{Ja,az} = \frac{8}{3} \left(\frac{\partial}{\partial a} C_{Ma,z} + \frac{\partial}{\partial z} C_{Ma,a} \right) \tag{5.21f}$$

5.3.3 Dynamic pressure

It has been shown by Legendre *et al.* (2003) that the potential flow is a valid approximation for added mass relations in a wide range of Reynolds number values. This fact supports the significance of the relations in section 5.3.1 and 5.3.2.

As shown by Moore (1965) and Batchelor (2010), the application of drag forces derived from dynamic pressure in potential flow is questionnable. However, the dissipation method by Levich (1949) adequately predict the drag forces by including both pressure and viscous drag. For these reasons, dynamic pressure terms are considered through the dissipation method of section 5.3.5.

5.3.4 Buoyancy

Buoyancy pressure term resumes to the usual buoyancy force which depends and acts only on z_b.

$$F_b = V_b(\rho_\ell - \rho_g)g \tag{5.22}$$

In the present case, we will neglect ρ_g as the gas density is much smaller than the liquid density.

5.3.5 Viscous dissipation - Validation

Viscous drag is estimated by the dissipation rate induced by viscosity (see Batchelor (2010)). From this technique, one can extract the drag force acting on a body from the total work rate in the fluid. Eq. (5.23a) defines this dissipation rate. After some manipulation, Eq. (5.23d) shows that there are components of the dissipation rate associated to pure modes ($\dot{z}_b^2$ and $\dot{a}^2$) and to a cross-coupled term ($\dot{z}_b\dot{a}$). In order to ensure that the proper amount of energy is dissipated, this last term has to be explicitely distributed on both modes. This energy dissipation is distributed in a manner proportional to the relative velocity of each mode as described by Eq. (5.23e). Doing so, dissipation rates are always preserved and no drag forces are applied on modes that are not active.

$$\dot{E} = \mu \iiint \nabla^2 \left(\nabla \left(\dot{z}_b\phi_z + \dot{a}\phi_a\right)\right)^2 dV \tag{5.23a}$$

$$= \mu \iiint \left[\nabla^2(\nabla\dot{z}_b\phi_z)^2 + \nabla^2(\nabla\dot{a}\phi_a)^2 + 2\nabla^2(\nabla\dot{z}_b\phi_z \cdot \nabla\dot{a}\phi_a)\right] dV \tag{5.23b}$$

$$\equiv \dot{E}_z + \dot{E}_a + 2\dot{E}_{a,z} \tag{5.23c}$$

$$= \dot{z}_b^2 I_z + \dot{a}^2 I_a + \dot{a}\dot{z}_b I_{a,z} \tag{5.23d}$$

$$= \dot{z}_b \underbrace{\left(I_z + \frac{|\dot{z}_b|}{|\dot{z}_b| + |\dot{a}|}\dot{a} I_{a,z}\right)}_{2F_{Dz}} + \dot{a} \underbrace{\left(I_a + \frac{|\dot{a}|}{|\dot{z}_b| + |\dot{a}|}\dot{z}_b I_{a,z}\right)}_{2F_{Da}} \tag{5.23e}$$

The total domain contains two identical bubbles, the real one and its image. Thus, the total dissipation rate corresponds to twice that of a single bubble (see Eq. (5.23e)). Drag forces F_{Dz} and F_{Da} can be described by the sum of two terms. Each term can be written in the form of Eq. (5.24) where the drag coefficients C_D are defined with the same formulation as for the jet coefficients.

$$F_{D_{q,q_1q_2}} = -\frac{1}{2}\rho_\ell \pi r_b^2 C_{D_{q_1,q_2q_3}}\ \dot{q}_2\dot{q}_3 \tag{5.24}$$

For pure translation and compression modes, the associated drag coefficients are compared to known relations in Fig. 5.5(a)-5.5(c). Fig. 5.5(a) presents a limited 5 terms expansion series by Kok in dashed and a higher order solution. Fig. 5.5(b) presents the χ dependency of the drag compared results of Moore (1965). The numerical calculation leads to a perfect agreement with Moore's relation. However, when comparing the drag on the compression mode, a slight deviation from Kushch *et al.* (2002) results is observed. Yet the agreement between both curves is good .

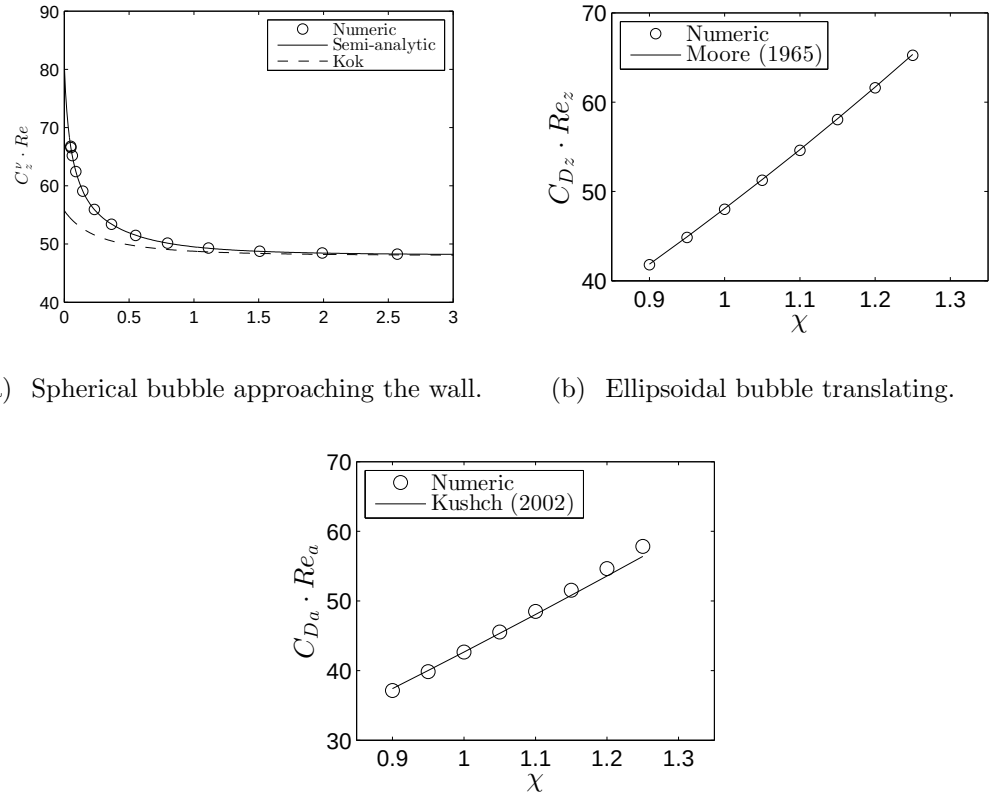

(a) Spherical bubble approaching the wall.

(b) Ellipsoidal bubble translating.

(c) Ellipsoidal bubble compressing.

Figure 5.5 Validation of the numeric approach for viscous drag coefficients.

5.3.6 Viscous dissipation - Regression relation

As it was done previously with the added mass coefficients, the drag coefficient regressions are modelled as the product of two independent functions. Doing so, a set of relations for drag coefficients is constructed in Eq. (5.25)-(5.28). These relations are then compared to the numerical calculation in Fig. 5.6(a)-5.6(c).

$$C_{Dz,zz} = \frac{48}{Re_z}\left[1 + \frac{0.0432}{(d/r_b + 0.195)^{1.56}}\right]G(\chi) \tag{5.25}$$

$$C_{Da,aa} = \frac{128/3}{Re_a}\left[1 + \frac{1}{(d/r_b + 1.09)^{8}}\right]\chi^{1.25} \tag{5.26}$$

$$C_{Dz,az} = \frac{1}{Re_z}\left[\frac{1.1}{(d/r_b + 1.86)^{1.85}}\right](2.05\chi - 1) \tag{5.27}$$

$$C_{Da,az} = \frac{1}{Re_a}\left[\frac{1.1}{(d/r_b + 1.86)^{1.85}}\right](2.05\chi - 1) \tag{5.28}$$

$$\tag{5.29}$$

where $G(\chi)$ is the relation of Eq. (5.30) given by Moore (1965) and the functional dependency in $\chi^{1.25}$ comes from the work by Kushch *et al.* (2002).

$$G(\chi) = \frac{\chi^{4/3}}{3}(\chi^2 - 1)^{3/2}\frac{[(\chi^2 - 1)^{1/2} - (2 - \chi^2)\mathrm{sec}^{-1}(\chi)]}{[\chi^2\mathrm{sec}^{-1}(\chi) - (\chi^2 - 1)^{1/2}]^2} \tag{5.30}$$

5.4 Model

This section focuses on the equation of motion governing the system and its application.

5.4.1 Equation of motion

Given the theoretical work presented in section 5.3, the equation of motion can be written as Eq. (5.31). Two new forces acting on a are introduced as F_σ and F_C. The first is the surface tension force and the second is the force induced by the translation motion on the compression mode.

$$\rho_\ell V_b \begin{pmatrix} C_{Mz,z} & C_{Ma,z} \\ C_{Ma,z} & C_{Ma,a} \end{pmatrix}\begin{pmatrix} \ddot{z}_b \\ \ddot{a} \end{pmatrix} = -\frac{1}{2}\rho_\ell A_b \begin{pmatrix} C_{Dz,zz} + C_{Jz,zz} & C_{Jz,aa} & C_{Dz,az} + C_{Jz,az} \\ C_{Ja,zz} & C_{Da,aa} + C_{Jz,aa} & C_{Da,az} + C_{Ja,az} \end{pmatrix}\begin{pmatrix} \dot{z}_b^2 \\ \dot{a}^2 \\ \dot{a}\dot{z}_b \end{pmatrix} + \begin{pmatrix} \rho_\ell V_b g \\ F^C + F^\sigma \end{pmatrix} \tag{5.31}$$

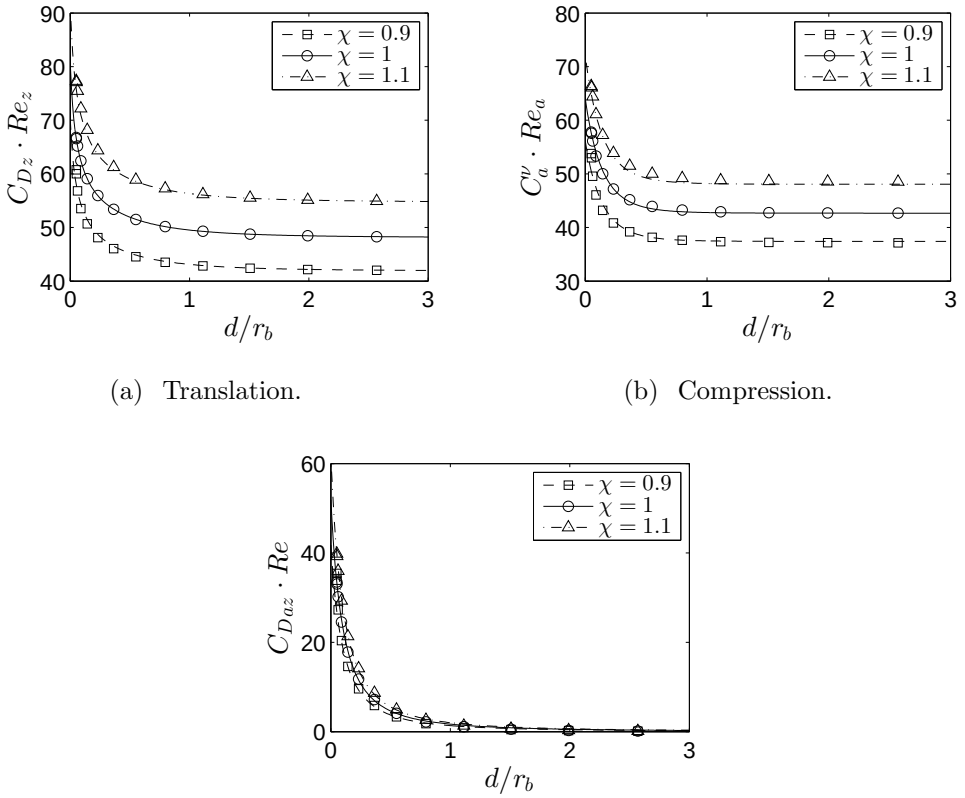

(a) Translation.

(b) Compression.

(c) Cross-coupling.

Figure 5.6 Regression (lines) and calculated values (nodes) of drag coefficients.

The accelerating mass of air is neglected since the added mass term is much larger due to density difference.

5.4.2 Surface tension force : F_σ

The potential energy stored in the surface is calculated as $E_\sigma = \sigma S$ where σ is the surface tension. S is the surface area of the bubble. Since surface deformation energy is conservative, the force acting against deformation can be calculated from $F_\sigma = -\partial E_\sigma / \partial a$. This relation can be fitted by the expression

$$F_\sigma = 4.482 \sigma r_b (\chi^{1.55} - 1) \tag{5.32}$$

for χ ranging from [0.8-3]. In the present model, σ was set to 0.072 N/m.

5.4.3 Compression force : F_C

The compression force is defined as :

$$F_C = -\frac{1}{2}\rho_\ell \pi r_b^2 C_C \dot{z}_b^2 \tag{5.33}$$

where C_C is the compression coefficient fitted to each experiment. This approach was selected to ensure that the initial state taken from the experiment is a steady state in the model. In other words, under terminal rise conditions, $F_C + F_\sigma = 0$. Therefore, no net forces are acting on a. Note that this equilibrium also gives rise to a $\chi(We_z)$ relation where We_z is the usual Weber number calculated with the z velocity component only.

As pointed out by Peters and Els (2012), two categories of bubbles can be generated in tap water : slow and fast bubbles. Each type having specific compression dependency over the We number. The expression (5.33) allows us to take these bubble categories into account.

5.4.4 Note on the drag forces

From the viscous dissipation rate theory detailed in section 5.3.5, the drag coefficients are found to decrease monotically with increasing Reynolds number for both a and z_b. As this is true for small Reynolds numbers, drag coefficients are empirically found to be bounded to a minimal value. This lower bound was added to the model.

For the translation mode, the terminal drag coefficient was calculated as the equilibrium between drag and buoyancy :

$$C_{Do} = \frac{8}{3}\frac{g r_b}{(\dot{z}_b)_o^2} \tag{5.34}$$

This value is set as the lower boundary of the $C_{Dz,zz}$ coefficient and allows initial conditions to create steady states.

The same limiting behavior is expected from the drag in the compression mode. As there is no empirical data on this drag relation, the lower boundary of $C_{Da,aa}$ was arbitrarily defined to be 5. It was chosen to produce similar behaviors between simulation and experiment.

5.4.5 Contact with the wall

Upon contact with the wall (i.e. $a = -z_b$), the system no longer depends on 2 degrees of freedom (DoF) since both coordinates are now equal. The governing equation during contact can be calculated as the difference of both lines of Eq. (5.31) with $a = -z_b$. The bubble becomes analogous to a damped oscillator of variable mass. Initial conditions are calculated assuming preservation of kinetic energy from the 2 DoF to the 1 DoF system. The kinetic

energy is evaluated through added mass coefficients as the total kinetic energy in the fluid (Milne-Thomson, 1968).

5.4.6 Departure from the wall

During contact, the condition $\ddot{z}_b = -\ddot{a}$ is enforced thus eliminating the need for a reaction force from the wall. A departure condition must therefore be defined without resorting to a reaction force. Departure from the wall occurs if the decompression speed of a bubble is not fast enough to compensate for the exit velocity. Numerically, this happens when $\ddot{a} < -\ddot{z}_b$ considering the 2 DoF system.

To evaluate this condition, Eq. (5.31) is used to calculate the acceleration of each mode assuming no contact. An event location routine is used to identify the exact time of departure. From that moment on, the system is modeled with the 2 DoF described previously with initial conditions $\dot{a} = -\dot{z}_b$.

5.5 Results

This section focuses on the applications of the model. First, a qualitative look over the model is given. Then, the model is compared with the experiment of Tsao and Koch (1997). Finally, a statistical comparison with our experimental results is done. Our experimental method and results are presented in another article (Pelletier *et al.*, 2014). The initial conditions of the simulations were extracted from experimental points and are denoted with subscript $_o$.

5.5.1 Qualitative description

Fig. 5.7 shows a comparison of the model and the experiments for different bubble properties. Fig. 5.7(a) represents the smallest bubble of our experimental dataset. The experimental curve of z_b/r_b shows an overdamped behavior of the bubble motion upon impact. The model predicts small oscillations before immobilization yet the overall behavior is respected. The slight offset between the equilibrium positions is of the order of the experimental resolution. Note that the aspect ratio is almost constant both for the model and the experiments ($\chi \simeq 1$).

The second and third row (Fig. 5.7(b) and Fig. 5.7(c)) are typical results for middle range radius of a fast and a slow bubble. On both z_b/r_b graphs, the model is underestimating the contact time. Also, the oscillation frequency is higher in the model than what is observed. This is likely to be a consequence of an overestimation in the bubble stiffness related to suface tension energy.

As previously described in Pelletier *et al.* (2014), fast and slow bubbles have different behaviors upon impact. Fast bubbles depict high rebound height while slow bubbles barely leave the wall. The present model is able to capture this behavior difference to the limit of the first bounce. After the second contact with the wall, the model overestimates the energy dissipation and the bouncing becomes heavily damped.

Finally, the last row (Fig. 5.7(d)) shows the biggest bubble observed experimentally. The model does not fit well with this particular experiment. This is mainly due to the fact that the bubble is further away than the assumed ellipsoidal shape. Visual inspection of images at impact shows high complexity deformation that cannot be taken into account with this model. Yet, the conclusions made previously for the stiffness overestimation and damped motion still hold.

5.5.2 Comparison with other work

Fig. 5.8 compares the present model to the data by Tsao and Koch (1997). Computation were done with $r_b = 0.83mm$, $(\dot{z}_b)_o = .25m/s$ and $\chi_o = 1.8$. The height of the rebound predicted by the model is underestimated when compared to the experimental results. The agreement is better for a higher value of χ_o as illustrated. Note that the calculation of χ by Tsao and Koch comes from a 2D projection of the bubble. This application might lead to underestimated χ if the motion of the bubble trajectory is not perfectly rectilinear.

The present model describes adequately the approach, contact and rebound stages. Discrepancies are observed after this first rebound and tend to amplify over time. From the data available in Tsao and Koch article, a restitution coefficient and a time interval were extracted and they will be compared to our experiments in section 5.5.3.

5.5.3 Statistical description

Numerous experimental impacts were conducted by changing the bubble size in our laboratory (Pelletier *et al.*, 2014). The first bounce of these bubbles will be studied in more details. To describe this process from the experimental point of view, an initial state and a final state were chosen. The initial state corresponds to the instant at which $z_b = -2r_b$ and is referred to with the $_o$ subscript. The final state (ejection sate) is the time at which the center of mass velocity is maximal and is referred to with the $_f$ subscript. Relations between these states are given in Pelletier *et al.* (2014).

For each experimental impact, a simulation was run. The initial values of the simulations were taken from the experimental initial state. The ejection state of the model was defined similarly to the experimental ejection state. The following sections will discuss the results.

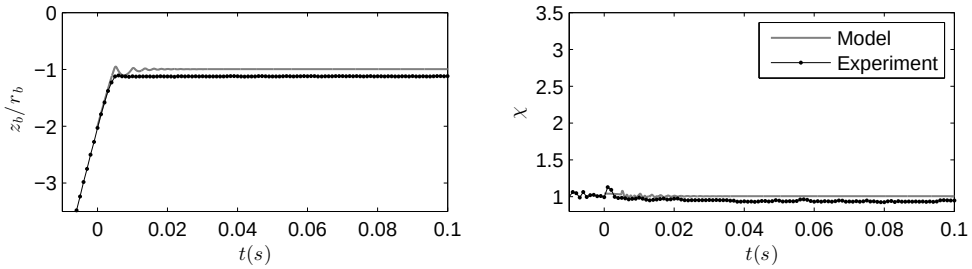

(a) Smallest bubble ; r_b =0.27mm ; Re=Re$_z$=35 ; We = We_z=.03

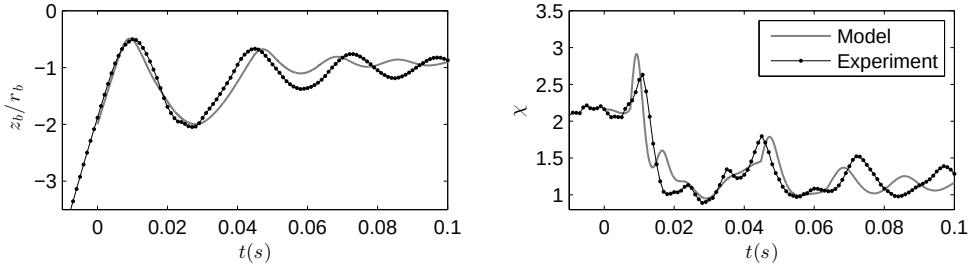

(b) Fast bubble ; r_b =1.3mm ; Re=790 ; Re$_z$=680 ; We = 3.33 ; We_z =2.5

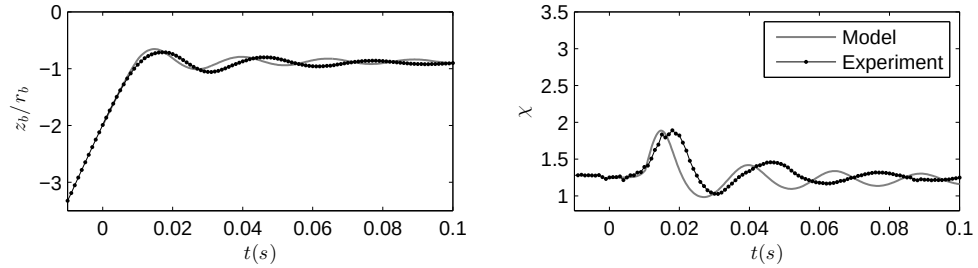

(c) Slow bubble ; r_b =1.7mm ; Re=760 ; Re$_z$=735 ; We = 2.35 ; We_z =2.21

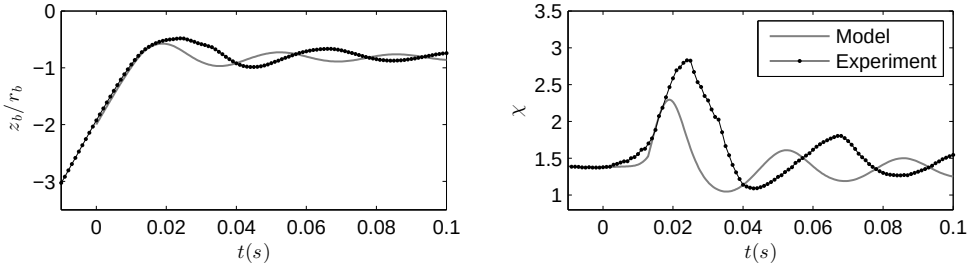

(d) Large bubble ; r_b =2.2mm ; Re=1030 ; Re$_z$=1000 ; We = 3.4 ; We_z =3.2

Figure 5.7 Distance from wall and aspect ratio of bubbles for different collision events : experiment and model.

Location at ejection

Fig. 5.9 illustrates the location of the center of mass at ejection (z_f) as a function of the bubble radius. Experimentally, fast and slow bubbles create two branches. The model

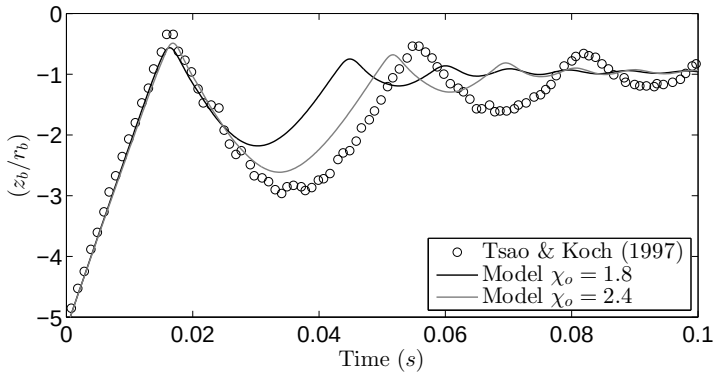

Figure 5.8 Comparison of the present model with Tsao & Koch (1997).

predict similar locations at ejection for both bubble types. The bouncing mechanism is based on the ellipsoidal shape assumption of bubbles. Experiments have shown that slow bubbles follow closely the assumed shape during the bounce. Fast bubbles, in contrast, go through a *triangular* shape during rebound as described by Zenit and Legendre (2009). This specific shape might be at the origin of the higher branch (see Fig. 5.14).

Fig. 5.10 shows the aspect ratio of the bubbles at ejection. There is a good agreement for slow bubbles and a considerable difference for fast bubbles. The discrepancy is induced again by the ellipsoidal bubble shape assumption. The model predicts that fast bubbles will bounce while preserving ellipsoidal shape thus creating a linear dependency to the initial aspect ratio as with the slow bubbles.

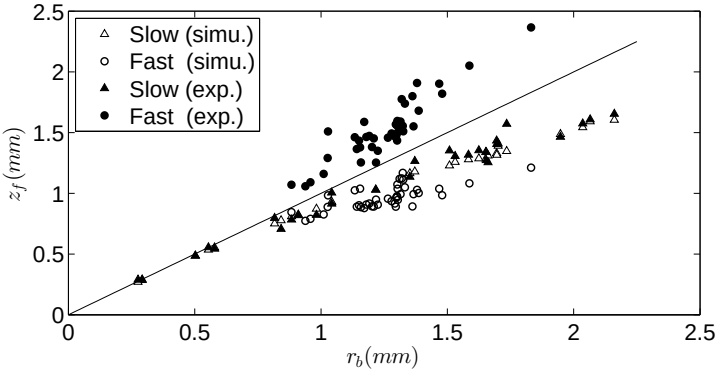

Figure 5.9 Center of mass position at maximal ejection velocity.

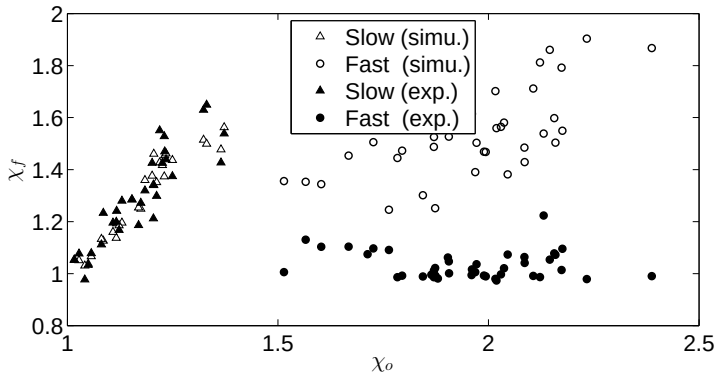

Figure 5.10 Aspect ratio at maximal ejection velocity.

Velocity at ejection

Fig. 5.11 and 5.12 show the velocity characteristics of the bubble at ejection. Fig. 5.11 shows the restitution coefficient as a function of the initial aspect ratio. The restitution coefficient is described as the ejection velocity over the initial velocity. These are in good agreement when $\chi_o > 1.25$. For smaller χ_o, the discrepancy is mainly due to a lack of drag forces on the bubble. For these bubbles, Reynolds number values are in the range 35-400. These bubble sizes would probably benefit from a Stokes flow analysis flow or the use of lubrication model.

Fig. 5.12 shows a dimensionless $\dot{\chi}_f$ as a function of χ_o. For slow bubbles, since the model ejection velocities are greater than the experimental results, the predicted χ velocities are also greater than in the experiments. Also, the predictions for the fast bubbles χ velocity are almost on a linear extrapolation of the slow bubbles χ velocity. This is in contrast with the constant values obtained from experimental fast bubbles.

Time delay

Fig. 5.13 shows the time interval between the initial and final state. The time is set non-dimensional by dividing by a characteristic time $\tau = r_b/\dot{z}_{bo}$. Both the model and experimental points follow the same trend although the time interval for the model is systematically shorter than what is observed. This is caused by the overestimation of the bubble stiffness as discussed in section 5.5.1 .

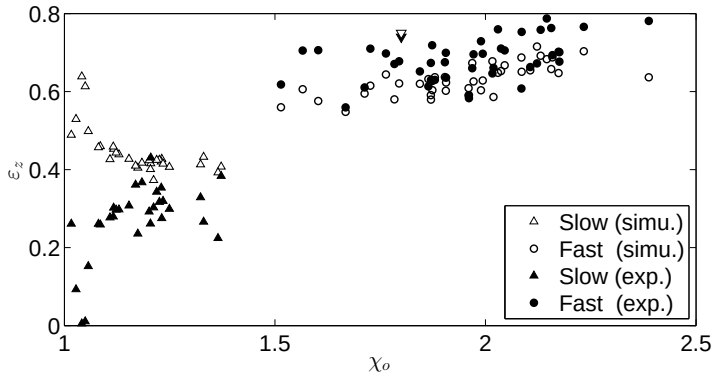

Figure 5.11 Restitution coefficient normal to the wall. (▼) and (▽) are experiments and simulation of Tsao and Koch (1997).

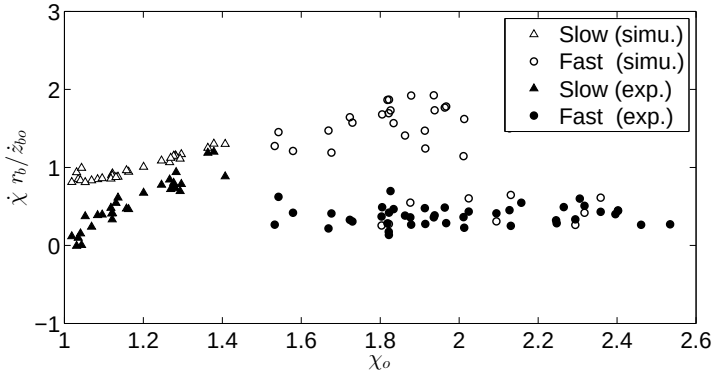

Figure 5.12 Dimensionless $\dot{\chi}_f$ at maximal ejection velocity.

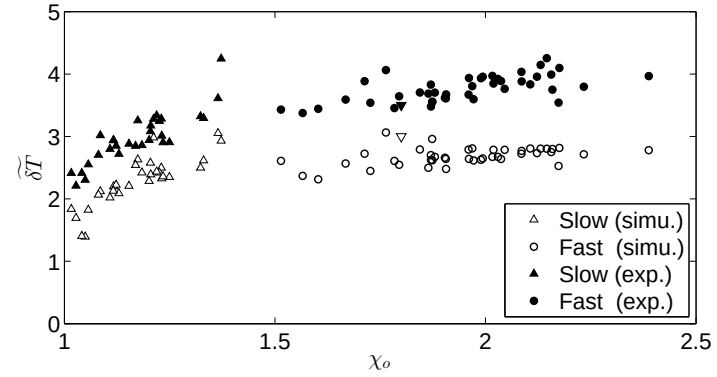

Figure 5.13 Dimensionless time interval between $t(z_b = 2r_b)$ and maximal ejection velocity. (▼) and (▽) are experiment and simulation of Tsao & Koch.

5.6 Discussion

Two causes of discrepancy can be identified from the previous sections. First, at low Reynolds number (< 400), the model underestimates the energy dissipation induced by the wall confinement. Therefore, predictions on the restitution coefficient are higher than observed. Nonetheless, for these low-velocity bubbles, the energy returned as kinetic energy is quickly dissipated and the overall behavior of the impact is verified (see Fig. 5.7(a)).

Second, some aspect of the bounce dynamic cannot be captured by the ellipsoidal bubble shape approximation. It must be understood that this shape is not an eigen vibration mode of the bubble. The eigen modes were shown to follow the shapes prescribed by the spherical harmonic functions Y_ℓ (Sommers and Foster, 2012). Note that the oscillation frequency of these vibration modes increases with ℓ.

By compelling the ellipsoidal shape to the bubble, some high ℓ-order modes are used. These high order modes might not be activated in the dynamics of real bubbles. Thus, the overall stiffness of the system is increased. Also, another consequence is that specific modes cannot be excited one-by-one. For instance, mode $\ell = 3$ is dominant during the rebound of fast bubbles. This third mode cannot be accounted for with the present model (see Fig. 5.14). This is likely to be at the origin of the collapse of the branches.

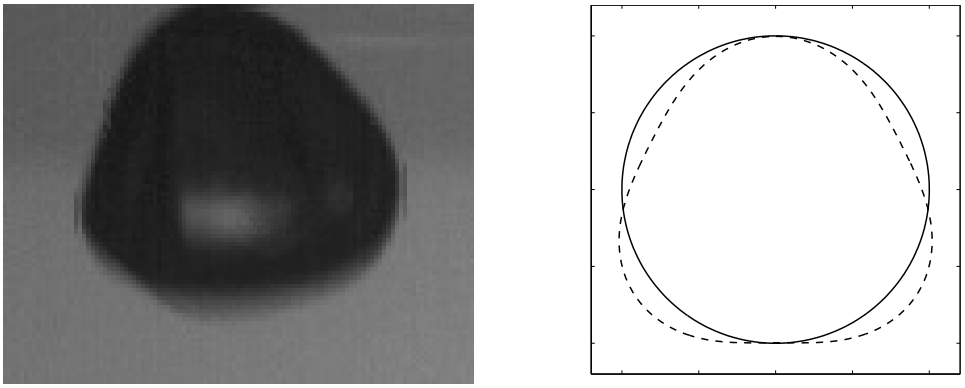

(a) Experiment. (b) (−−) Eigen mode shape ($\ell = 3$).

Figure 5.14 *Triangular shape* of bubble on rebound.

It is also important to keep in mind that the model is based on a 1D spatial coordinate (z_b). Yet most of the experimental impacts occured with bubbles having a non-zero tangential velocity to the wall. This brings an important point regarding the closure of the system with a $\chi(We)$ relation. The work by Ellingsen and Risso (2001) suggests that the aspect ratio χ is a function of the velocity magnitude and not of the rise velocity . This implies that knowing only the rise velocity is not sufficient to determine the aspect ratio. In other words,

a universal relation for $\chi(We_z)$ cannot be defined.

To overcome this difficulty, the compression coefficent C_C was introduced in section 5.4.3. This coefficient serves two purposes. First, it implicitly takes into account for the bubble category (slow or fast). Indeed, no subjective choice of category has to be made in the model. Second, the compression coefficient removes the necessity of having a $\chi(We_z)$ relation. Note that the C_C coefficient could be defined analytically through a $\chi(We)$ relation with the use of an additional DoF describing the bubble trajectory.

5.7 Conclusion

Finally, although some discrepancies exist between the model and the experiment, the overall behaviors are in agreement. The developed model offers a 2 DoF system to predict the impact dynamics of bubbles with rigid walls. It can efficiently be applied to two-phase bubbly flow simulations with a Lagragian formalism without having to solve the flow configuration at each time iteration. The next step in development would be to consider two additionnal DoF. One will represent the $\ell = 3$ mode exhibited by fast bubbles. The other will be used to describe the path trajectory.

Acknowledgments

This work was sponsored by the Natural Sciences and Engineering Research Council, Babcock & Wilcox Canada and Atomic Energy of Canada Ltd., through the BWC/AECL/NSERC research chair in fluid-structure interactions.

References

BATCHELOR, G. (2010). *An introduction to fluid dynamics*. Cambridge University Press, New York, 14^e édition.

CANOT, E., DAVOUST, L., EL HAMMOUMI, M. and LACHKAR, D. (2003). Numerical simulation of the buoyancy-driven bouncing of a 2-d bubble at a horizontal wall. *Theoretical and Computational Fluid Dynamics*, 17, 51–72.

ELLINGSEN, K. and RISSO, F. (2001). On the rise of an ellipsoidal bubble in water: oscillatory paths and liquid-induced velocity. *Journal of Fluid Mechanics*, 440, 235–268.

KLASEBOER, E., CHEVAILLIER, J.-P., MATÉ, A., MASBERNAT, O. and GOURDON, C. (2001). Model and experiments of a drop impinging on an immersed wall. *Physics of Fluids*, 13.

KOK, J. (1993). Dynamics of a pair of gas bubbles moving through liquid. i: Theory. *European journal of mechanics. B, Fluids*, 12, 515–540.

KUSHCH, V. I., SANGANI, A. S., SPELT, P. D. and KOCH, D. L. (2002). Finite-weber-number motion of bubbles through a nearly inviscid liquid. *Journal of Fluid Mechanics*, 460, 241–280.

LEGENDRE, D., DANIEL, C. and GUIRAUD, P. (2005). Experimental study of a drop bouncing on a wall in a liquid. *Physics of Fluids*, 17, 97105.

LEGENDRE, D., MAGNAUDET, J. and MOUGIN, G. (2003). Hydrodynamic interactions between two spherical bubbles rising side by side in a viscous liquid. *Journal of Fluid Mechanics*, 497, 133–166.

LEVICH, V. (1949). The motion of bubbles at high reynolds numbers. *Zh. Eksp. Teor. Fiz*, 19, 436.

MILNE-THOMSON, L. (1968). *Theorical Hydrodynamics*. Macmillan, New York, 5^e édition.

MOORE, D. W. (1965). The velocity of rise of distorted gas bubbles in a liquid of small viscosity. *Journal of Fluid Mechanics*, 23, 749–766.

MORAGA, F.J., S. C. and R.T. LAHEY, J. (2005). Modeling wall induced forces on bubbles for inclined walls. *Multiphase Science and Technology*, 17, 483–505.

PELLETIER, E., BÉGUIN, C. and ÉTIENNE, S. (2014). Experiments air bubbles impacting a rigid wall in tap water. *Physics of fluid - Submitted*.

PETERS, F. and ELS, C. (2012). An experimental study on slow and fast bubbles in tap water. *Chemical Engineering Science*, 82, 194–199.

PODVIN, B., KHOJA, S., MORAGA, F. and ATTINGER, D. (2008). Model and experimental visualizations of the interaction of a bubble with an inclined wall. *Chemical Engineering Science*, 63, 1914 – 1928.

SOMMERS, B. and FOSTER, J. (2012). Nonlinear oscillations of gas bubbles submerged in water: implications for plasma breakdown. *Journal of Physics D: Applied Physics*, 45, 415203.

TSAO, H. and KOCH, D. L. (1997). Observations of high reynolds number bubbles interacting with a rigid wall. *Physics of Fluids*, 9.

VAN WIJNGAARDEN, L. and VELDHUIS, C. (2008). On hydrodynamical properties of ellipsoidal bubbles. *Acta mechanica*, 201, 37–46.

ZENIT, R. and LEGENDRE, D. (2009). The coefficient of restitution for air bubbles colliding against solid walls in viscous liquids. *Physics of Fluids*, 21.

CHAPITRE 6

SUJETS SUPPLÉMENTAIRES

Ce dernier chapitre couvre brièvement trois autres sujets étudiés dans le cadre de cette maîtrise. Premièrement, les forces agissant sur un mur lors d'un impact. Deuxièmement, quelques observations sur l'éclatement de bulles puis finalement une remarque sur la conservation de l'énergie dans un système à masse variable.

6.1 Force d'intéraction bulle-mur

Dans cette portion du travail, une analyse expérimentale des forces transmises lors d'une collision bulle-structure sera effectuée. Il sera montré qu'une bulle induit des forces substantielles à distance sur une structure durant son approche. De plus, dans le cadre du modèle développé pour une collision bulle-mur au chapitre 5, des expressions théoriques de ces forces seront présentées.

6.1.1 Approche expérimentale

Dans le but de caractériser les forces générées par la collision d'une bulle, un banc d'essais a été construit. Celui-ci est constitué d'une colonne d'eau d'environ 30 cm de hauteur avec des trous à la base permettant l'injection de bulles d'air. L'injection est faite manuellement par un mouvement de va-et-vient. Suite à l'injection, la bulle s'élève sous l'action de la gravité jusqu'à l'obtention de sa vitesse terminale. Un dispositif de mesure de force est positionné au-dessus du site d'injection afin que la bulle ascendante le heurte.

La figure 6.1(a) présente une vue schématique de ce dispositif. Il est composé d'un cylindre carré et creux, fermé à une extrémité, flottant à la surface de l'eau. Il est tenu en position verticale par 2 groupes de 3 élastiques à tension ajustable disposés en triangle sur deux plans superposés et déphasés de 60° (non-illustrés). Le positionnement a été fait de manière à maximiser l'amplitude du pilonnement tout en minimisant l'amplitude de roulis du flotteur. En plus des élastiques, une raideur supplémentaire est apportée par la poussée d'Archimède. La raideur équivalente mesurée est d'environ 6 N/m. Hors masse ajoutée, le flotteur pèse 6 g.

Le système ainsi créé se comporte comme un oscillateur amorti. S'il y a contact entre une bulle et le flotteur, son déplacement sera indicateur des forces transmises. L'évènement de contact est filmé en lumière transmise par une caméra ultra-rapide à une fréquence de 1kHz. La source de lumière est une ampoule halogène. Trois cercles noirs sont dessinés sur le flotteur

afin de faciliter la détection de ses mouvements. La figure 6.1(b) montre une image capturée lors d'une expérience à un temps précédent l'impact. Sur cette image, le rayon équivalent de la bulle est $r_b = 0.65$mm et la largeur d'un côté du cylindre est de 12.5mm.

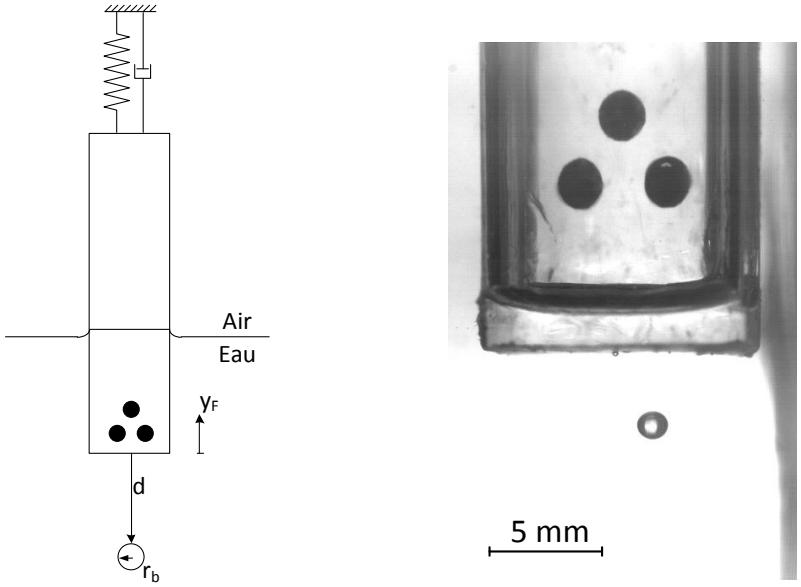

(a) Schéma du montage (b) Image capturée

Figure 6.1 Montage expérimental pour l'observation des forces d'impact.

6.1.2 Post-traitement

La position du flotteur est obtenue par un traitement numériquesur les trois cercles noirs. Le traitement va comme suit :

1. Application d'un seuillage sur les gris pour identifier les cercles ;
2. Remplissage des trous dans les formes (si nécessaire) ;
3. Localisation du centre de masse de chaque cercle ;
4. Moyenne sur les 3 positions des centres de masse ;
5. Chargement de la nouvelle image et retour à 1.

La distance bulle-flotteur est définie comme la distance entre le front avant de la bulle et la position lors du contact avec le flotteur. Le traitement automatisé est :

1. Identification sur l'image #1 d'un point sur le front avant de la bulle ;
2. Définition d'une vignette carrée (1/4 taille de la bulle) centrée sur ce point ;

3. Optimisation de la position de cette vignette sur l'image suivante ;
4. Enregistrement de la position de cette vignette et retour à 2.

6.1.3 Résultats

Trois essais ont été réalisés avec ce montage. Les caractéristiques des bulles sont présentées dans le tableau 6.1. Les résultats du post-traitement sont illustrés sur les graphiques de la figure 6.2. La colonne de gauche fait référence à la position temporelle du flotteur (Y_F) sur la durée totale de l'expérience. La colonne de droite présente ces mêmes courbes autour du moment d'impact. La distance bulle-flotteur (d) est reportée sur l'axe de droite.

Tableau 6.1 Caractéristiques des bulles

Bulle	Catégorie	Rayon
#1	Lente	0.65mm
#2	Lente	1.35mm
#3	Rapide	0.95mm

On note que le flotteur oscille déjà avant l'impact dans les trois expériences. En effet, le système est extrêmement sensible à toutes perturbations. La perturbation qui est à l'origine de l'oscillation initiale est probablement l'augmentation du niveau de l'eau suite à la création de la bulle à la base de la colonne. De plus, la position d'équilibre du flotteur diminue dans le temps pour les expériences #1 et #2. Cette baisse est causée par une légère infiltration d'eau dans le cylindre augmentant ainsi sa masse. Malgré cet état initial perturbé, l'impact reste clairement visible pour les trois situations.

Les graphiques de la colonne de droite illustrent un phénomène important : le mouvement du flotteur débute avant le contact. Dans les faits, on observe une déviation de la trajectoire initiale du flotteur lorsque la bulle est à une distance d'environ 5 r_b dans les trois expériences. Une analyse de la vitesse du flotteur indique que l'essentiel de la vitesse est transmise **avant contact**.

6.1.4 Force potentielle sur le mur

Sous l'hypothèse que la bulle est beaucoup plus petite que le flotteur, la situation peut être considérée comme une interaction bulle-mur. Cette hypothèse sera d'autant plus respectée quand la bulle sera très proche du flotteur. L'écoulement associé à cette configuration a été développé au chapitre 4. Comme première approximation, la bulle est considéré comme sphérique et non déformable (*i.e.* : $a = r_b$). Le système considéré est illustré sur la figure 6.3.

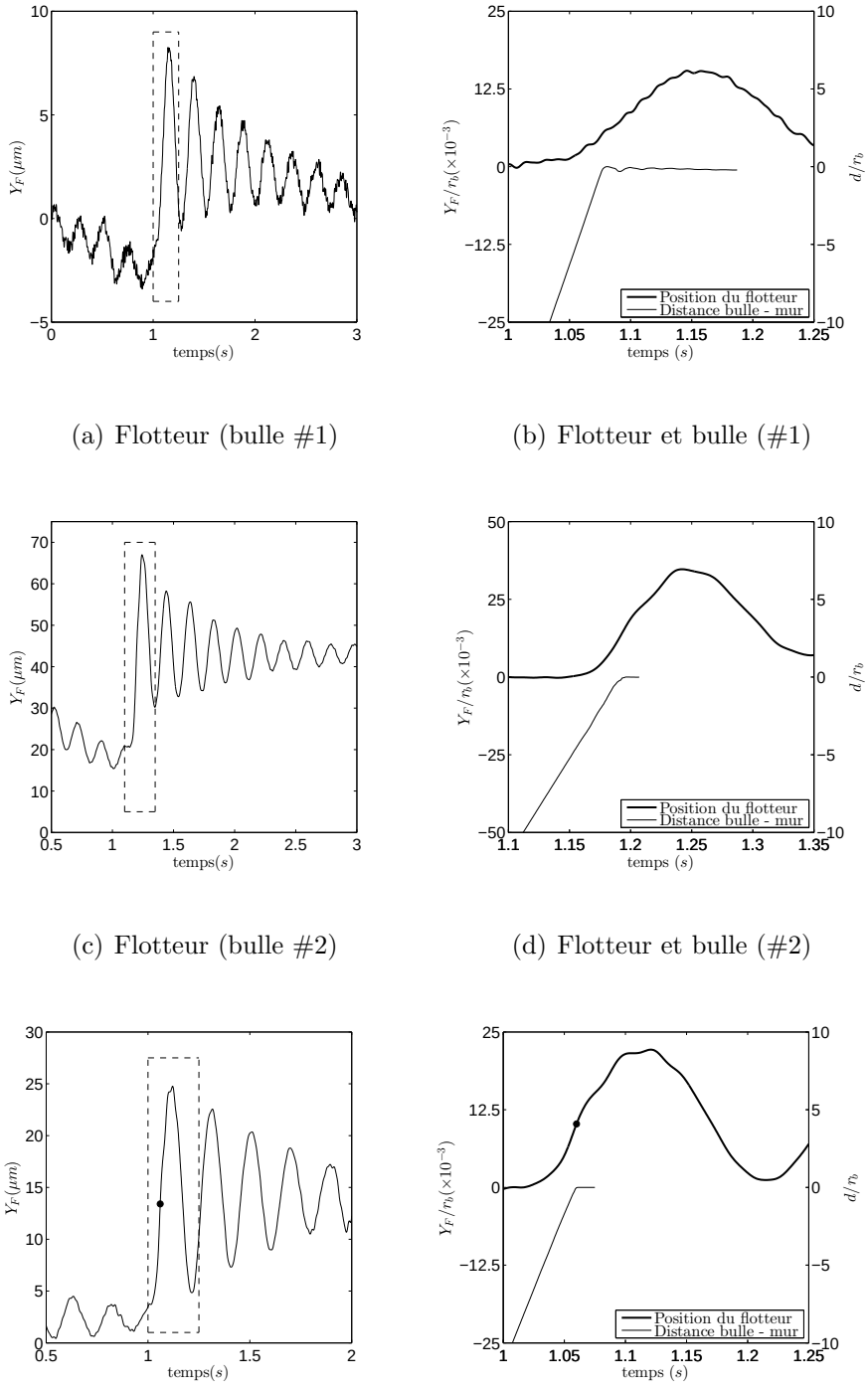

(a) Flotteur (bulle #1)

(b) Flotteur et bulle (#1)

(c) Flotteur (bulle #2)

(d) Flotteur et bulle (#2)

(e) Flotteur (bulle #3)

(f) Flotteur et bulle (#3)

Figure 6.2 Position du flotteur et de la bulle durant l'impact. Les figures de la colonne de droite sont des agrandissements des zones encadrées dans les figures de la colonne de gauche.

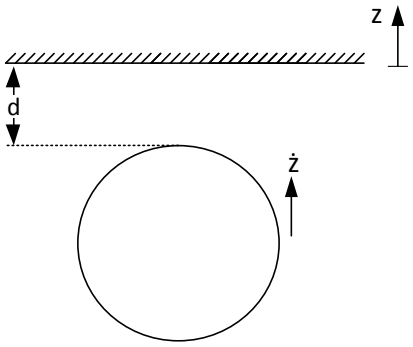

Figure 6.3 Système considéré pour le calcul des forces potentielles sur le mur

Rappelons l'équation de la pression instationnaire de Bernoulli (Eq. 6.1). Notez que le terme de convection est retiré car le mur est considéré immobile. Le terme de gravité est également omis dû à sa constance. La force subite par le mur est calculée par l'intégration de la pression (Eq. 6.1) sur sa surface. La figure 6.4 présente les profils de pression associés à chacun des trois termes : Masse ajoutée, Jet et Pression dynamique. L'intégration a été effectuée numériquement en se limitant à une surface circulaire de rayon $R_{integration}$=5r_b,10r_b et 50r_b centrée au-dessus de la bulle et ce, pour différentes distances bulle-mur (d).

$$P = -\rho_\ell \left(\underbrace{\frac{\partial \Phi}{\partial \dot{z}_b}\ddot{z}_b}_{\text{Masse ajoutée}} + \underbrace{\frac{\partial \Phi}{\partial z_b}\dot{z}_b}_{\text{Jet}} - \underbrace{\frac{1}{2}(\nabla \Phi)^2}_{\text{Pression dynamique}} \right) \tag{6.1}$$

Les résultats sont présentés dans la figure 6.5 sous la forme de coefficients de force tel que décrit par les équations 6.2, 6.3 et 6.4. z est défini positif comformément à la figure 6.3.

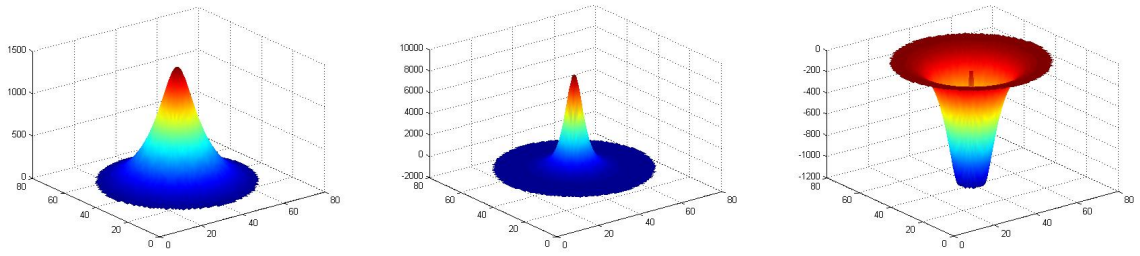

(a) Pression de masse ajoutée (b) Pression de jet (c) Pression dynamique

Figure 6.4 Forme des profils de pression sur le mur avec $R_{integration}$ = 10r_b et d=3 r_b

$$F_M = \rho_\ell V_b C_M \ddot{z} \tag{6.2}$$

$$F_J = \frac{1}{2}\rho_\ell A_b C_J \dot{z}^2 \tag{6.3}$$

$$F_{PD} = \frac{1}{2}\rho_\ell A_b C_{PD} \dot{z}^2 \tag{6.4}$$

Deux phénomènes sont observés sur ces courbes. Premièrement, lorsque d approche de zéro, les coefficients ont tendance à augmenter rapidement. Ceci est dû à l'hypothèse d'un fluide non visqueux. En effet, afin de respecter les conditions aux frontières, les vitesses dans le film entre la bulle et le mur peuvent prendre de très grandes valeurs. Or, il a été montré que lorsque $d \lesssim 0.1 r_b$, les effets visqueux dominent dans ce film (Klaseboer *et al.*, 2001). Les valeurs de ces coefficients au contact sont donc à prendre avec discernement.

Ensuite, plus $R_{integration}$ est grand, plus la période de décroissance des coefficients de masse ajoutée et de jet est grande. Ceci est également un résultat de l'hypothèse d'écoulement potentiel. Dans ce type d'écoulement, toute perturbation se propage instantanément sans dissipation au travers du fluide. Ce faisant, un point du mur se situant à plus de $50 r_b$ de la bulle peut ressentir une variation de pression non-négligeable. Dans le cas d'un fluide réel, ces variations seraient probablement dissipées par la viscosité. Il s'agit entre autres de la raison pour laquelle différents rayons d'intégration sont présentés.

De plus, la largeur du flotteur dans nos expériences est compris entre 10 et 20 r_b. Les forces qu'il subit doivent être proches de celles calculées avec ces rayons d'intégrations. Selon ces relations, une bulle s'approchant créerait une force répulsive dû à la force de jet à partir d'une distance d'environ 10 r_b. Puis, durant le contact, puisqu'elle subit une accélération négative (vers les z négatifs), une force négative de masse ajoutée devrait se rajouter.

De manière qualitative, on peut voir ce comportement sur les figures 6.2(b), 6.2(d) et 6.2(f). En effet, le flotteur accélère vers le haut durant la phase d'approche de la bulle où on voit la pente augmenter. Puis, peu après le contact, pendant une accélération de la bulle vers le bas, la vitesse du flotteur diminue.

Il est possible également d'avoir un ordre de grandeur de ces forces. Prenons l'exemple d'une bulle de 1 mm de rayon se trouvant à une distance de $d = 2r_b$ du mur. Sa vitesse d'ascension sera d'environ v =20cm/s. L'intervalle de temps avant le contact avec le mur peut être évaluée comme $\delta t = d/v$ = .01s. L'ordre de grandeur de l'accélération sera de ($\delta v/\delta t = -20 m/s^2$). En prenant les rayons d'intégration de 5 r_b, les forces peuvent être évaluées comme :

$$F_M \approx 67\mu\text{N}$$
$$F_J \approx 32\mu\text{N}$$
$$F_{PD} \approx 0\mu\text{N}$$

En réalité, la bulle ne décélère pratiquement pas avant le contact. La décélération se fait par l'entremise du mode de compression de la bulle. Donc l'essentiel de la force à distance proviendrait de la force de jet. Il est possible de comparer la grandeur de la force de jet calculée en exemple avec l'expérience #3. En effet, le rayon de la bulle donnée en exemple (r_b = 1mm) est très proche de celle mesurée à l'expérience #3 (r_b = 0.95mm).

Sous l'hypothèse que le flotteur est en équilibre avec la force de jet, on peut calculer son déplacement. Il serait d'environ de 5.3μm. On note expérimentalement un déplacement similaire (4 μm) (voir Fig. 6.2(f)). Ceci suggère que la force de jet pourrait bien être à l'origine de ces forces à distance.

6.1.5 Travaux futurs

Afin de pouvoir mener à terme ces travaux et de comparer le modèle de force aux expériences, une part expérimentale et une part théorique doivent être complétées. Premièrement, la partie expérimentale consiste à caractériser davantage le système de captation des forces. Bien que le système se comporte comme un oscillateur harmonique amorti, ses caractéristiques ne sont pas bien connues. En fait, seul $\omega = \sqrt{k/m}$ est défini tandis que k et m ne sont pas connus avec précision.

En effet, la masse réelle du flotteur est connue mais sa masse ajoutée ne l'est pas. Puisque la densité apparente du flotteur est plus faible que celle de l'eau, la contributation de la masse ajoutée risque d'être importante. De plus, la raideur du système est difficile à quantifier car elle comporte une composante dynamique. Cette composante provient de l'attachement du ménisque à la paroi du flotteur. En oscillant, l'angle du ménisque change et apporte des variations substantielles à la raideur statique.

Du point de vue théorique, un aspect est manquant pour décrire le processus de collision. Bien que l'approche pourrait être décrite par un modèle à bulle sphérique (et rigide), au moment de l'impact, la bulle se déforme. Si cette déformation n'est pas prise en compte, l'arrêt instantané de la bulle génère une accélération infinie et donc une force de masse ajoutée infinie sur le mur. Ainsi, le mode de compression de la bulle (tel que présenté dans le chapitre 5) doit être utilisé pour décrire les forces au moment de l'impact.

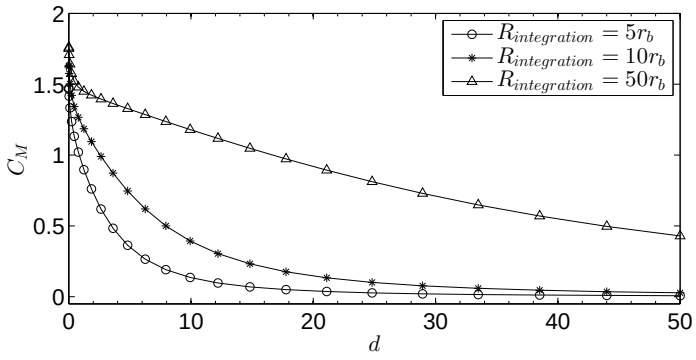

(a) Force de masse ajoutée

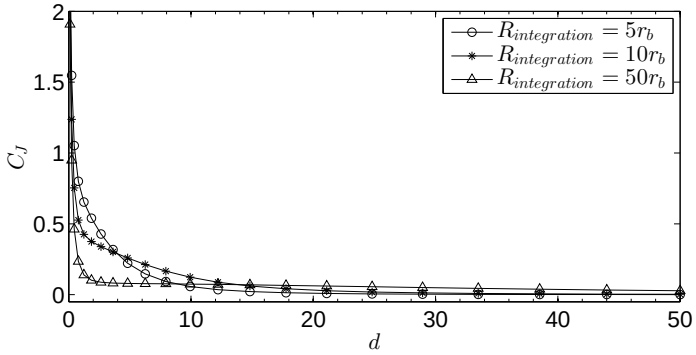

(b) Force de jet

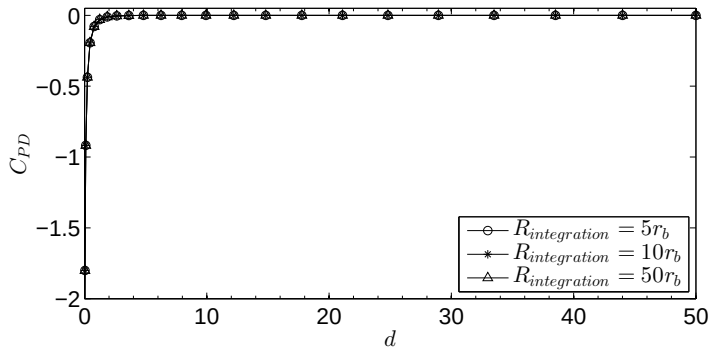

(c) Force de pression dynamique

Figure 6.5 Force à distance sur un mur pour différents rayons d'intégration

6.2 Éclatement de bulle

Malgré un nombre important d'expériences en milieu stagnant, aucun éclatement de bulle n'a été observé. Un banc d'essais à été construit afin d'observer des collisions bulle-mur avec des vitesses plus élevées en espérant observer des éclatements. La figure 6.6 illustre un schéma du montage. Il s'agit d'une section carrée au milieu de laquelle une plaque horizontale est fixée. Cette section est connectée sur une boucle d'alimentation en eau déjà existante au laboratoire. La vitesse à l'entrée peut varier entre 0 et 1m/s et la section d'entrée du fluide mesure 10cm×10cm. Tous les composants sont en plexiglas afin de permettre la visibilité. Les bulles sont générées manuellement à l'aide d'une seringue. Bien que les résultats obtenus n'ont pas été ceux attendus, différents points méritent mentions.

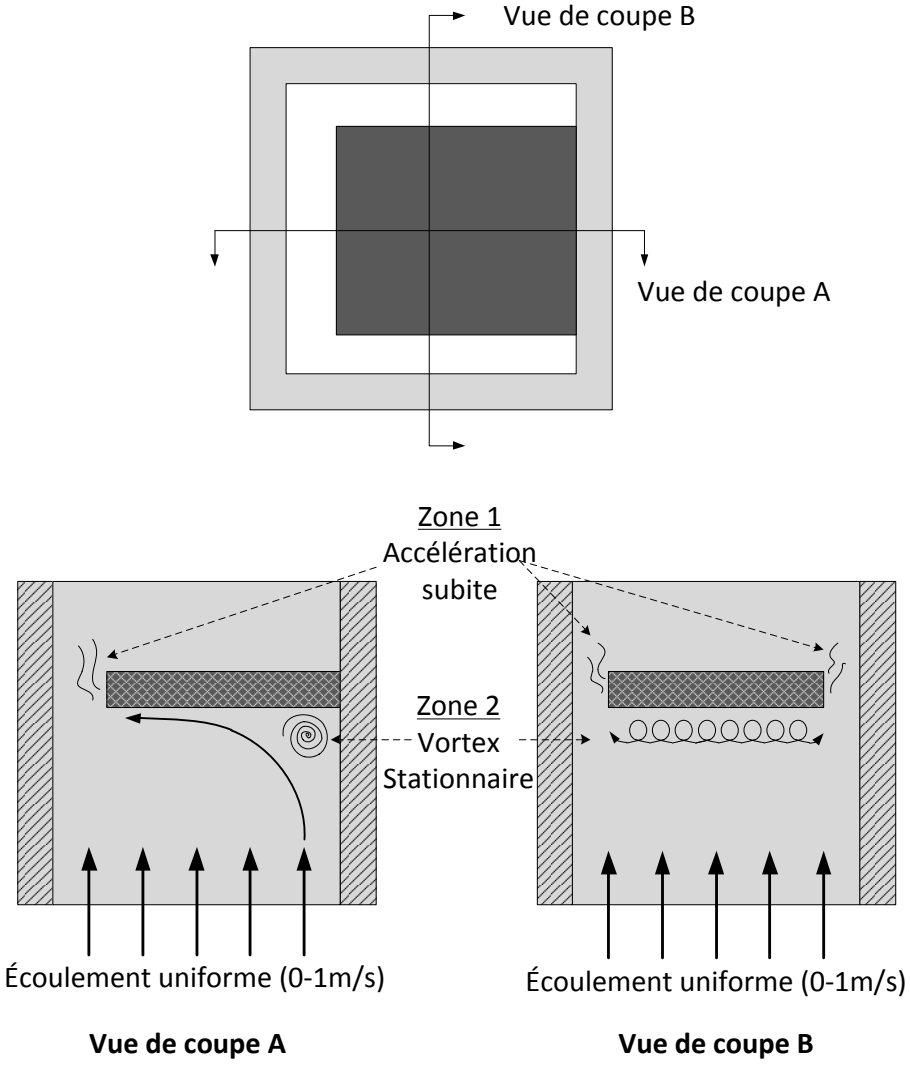

Figure 6.6 Schéma du banc d'essais pour des impacts à haute vitesse.

6.2.1 Vitesse d'approche

Il s'est avéré impossible de produire des collisions bulle-mur avec des vitesses d'approche plus élevées que la vitesse d'ascension en milieu stagnant. Ceci s'explique par la forme de l'écoulement. La figure 6.7 présente une approximation de cet écoulement tel que vu dans le plan de coupe B de la figure 6.6. Le champ de vitesse (noir) est construit par interpolation des vitesses des particules en suspension dans le fluide (rouge). Par ce champ de vitesse, il est possible de connaître la vitesse locale à tout endroit en amont de la plaque.

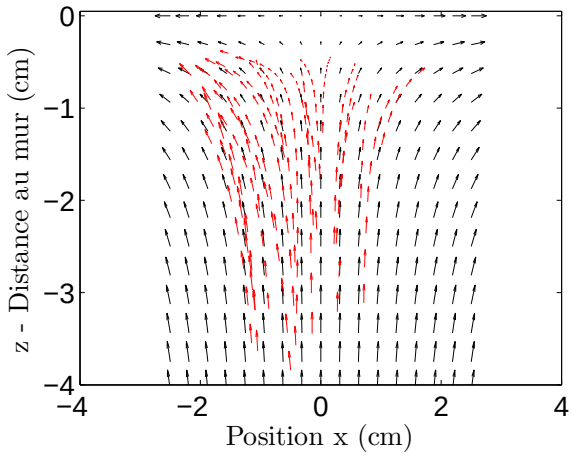

Figure 6.7 Champ de vitesse en amont de la plaque (coupe B de la figure 6.6)

Pour une bulle dans un écoulement de vitesse locale $\mathbf{w}$, la force de traînée se définie comme :

$$\mathbf{F_D} = -\frac{1}{2}\rho_\ell A_b C_D \|\mathbf{v_b} - \mathbf{w}\|(\mathbf{v_b} - \mathbf{w}) \tag{6.5}$$

Loin du mur, $\mathbf{w}$ est grand et participe à la vitesse élevée de la bulle. Or, à proximité de la plaque, la composante normale au mur de $\mathbf{w}$ est nulle. Il ne reste que la force de traînée en milieu stagnant. On observe expérimentalement que l'inertie de la bulle est négligeable par rapport au terme forçant. En effet, la vitesse de la bulle s'adapte très rapidement à la vitesse locale du fluide et n'est pas *entraînée* par son inertie. Il est donc difficile de concevoir une technique d'impact de bulle sur un mur à des vitesses élevées car la vitesse normale au mur tombe nécessairement à zéro sur sa surface.

Notez que cette conclusion est valable lorsque le taux de vide est faible. Si le taux de vide augmente, des effets de confinements et des forces inter-bulles apparaîtront. Ce type d'intéraction causerait des forces supplémentaires pouvant potentiellement créer des vitesses d'impact plus élevées.

6.2.2 Éclatement

Bien qu'aucun éclatement de bulle ne s'est produit lors d'impacts, plusieurs éclatements de bulles ont été observés. Ces évènements ont plutôt eu lieu aux endroits où il y a un fort cisaillement. Typiquement, ce sont également les endroits de forts gradients d'accélération. À l'intérieur de notre section d'essais, on peut noter deux zones d'éclatement. La première est une zone d'accélération subite (zone 1) et la deuxième comporte un vortex stationnaire (zone 2)(voir fig. 6.6).

La figure 6.8 illustre les éclatements observés. Les séquences (a) et (b) sont des éclatements dus à des vortex (vue par les deux coupes) et la séquence (c) est un éclatement par accélération subite. Dans les trois cas, une bulle avec un rayon équivalent de l'ordre du millimètre éclate en une multitude de bulles ayant des dimensions d'au moins un ordre de grandeur plus petites.

(a) Vortex Stationnaire - Vue de coupe B

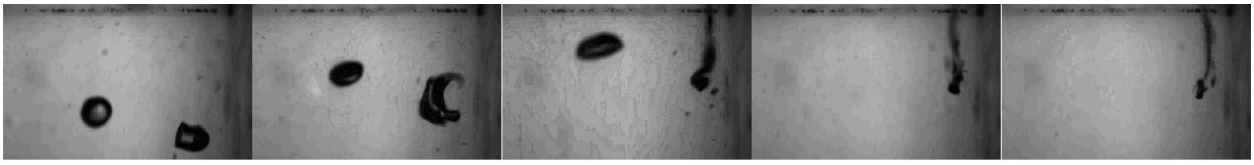

(b) Vortex Stationnaire - Vue de coupe A

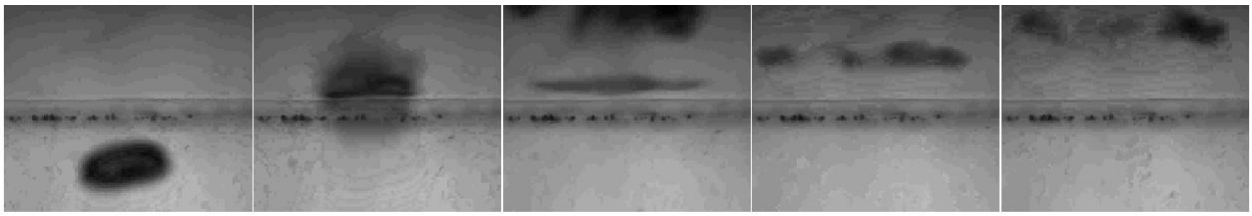

(c) Accélération subite

Figure 6.8 Éclatements observés expérimentalement

6.2.3 Discussion

Le but de cette portion de travail était de comparer le modèle développé dans au chapitre 5 avec des impacts à haute vitesse sur un mur. On en conclut que ce type d'impact ne peut se produire. Toutefois, deux modes d'éclatement de bulle ont été observés. Ces observations sont

importantes car elles mettent en lumière les mécanismes qui doivent être pris en compte afin de bien prévoir l'éclatement de bulle. Ces mécanismes devraient être inclus dans le modèle de Senez et Étienne (2011).

6.3 Notes sur la conservation de l'énergie

Finalement, cette dernière section a comme but de souligner les particularités liées à la résolution de systèmes comprenant des corps à masse variable en espace. Dans un système classique à masse constante, il est naturel d'affirmer que toutes variations de l'énergie cinétique provient du travail d'une ou de plusieurs forces externes (F_{ext}). Par contre, lorsque la masse varie dans l'espace, une force supplémentaire doit être prise en compte. C'est le cas d'une bulle approchant d'un mur ou de l'oscillation d'une bulle ellipsoïdale car $C_M = C_M(z, \chi)$

Considérons le mouvement d'une masse $m = m(x)$ selon une coordonnée x et définissons $v = \dot{x}$. En partant de la deuxième loi de newton puis en multipliant par v de chaque côté :

$$\frac{d}{dt}(mv) = \sum F_{ext} \implies v \cdot \frac{d}{dt}(mv) = \sum F_{ext} \cdot v \tag{6.6}$$

$$\implies mv\frac{dv}{dt} + v^2\frac{dm}{dt} = \sum F_{ext} \cdot v \tag{6.7}$$

On utilise la relation

$$\frac{d}{dt}\left(\frac{1}{2}mv^2\right) = \frac{1}{2}v^2\frac{dm}{dt} + mv\frac{dv}{dt} \tag{6.8}$$

Pour obtenir

$$\frac{d}{dt}\underbrace{\left(\frac{1}{2}mv^2\right)}_{E_c} = \underbrace{\sum F_{ext} \cdot v}_{W_{ext}} - \underbrace{\frac{1}{2}v^3\frac{dm}{dx}}_{W_{int}} \tag{6.9}$$

où E_c est l'énergie cinétique, W_{ext} le travail fait par les forces extérieures et W_{int} le travail fait par la force que nous avons nommé *jet*. La dérivée en chaîne a été utilisée pour obtenir $dm/dt = v \cdot dm/dx$. Notez qu'en l'absence de forces extérieurs, la variation d'énergie cinétique n'est pas nulle.

Application à la bulle oscillante

Prenons l'exemple de l'oscillation d'une bulle en compression. Aux fins de l'exercice, la dissipation visqueuse sera négligée. L'état initial de la bulle sera pris comme $a = r_b$ et $\dot{a} = \dot{a}_o$. Par analogie avec la relation (6.7), l'équation du mouvement est :

$$\rho_\ell V_b C_{Maa} \ddot{a} = F_r - \dot{a}^2 \rho_\ell V_b \frac{dC_{Maa}}{da} \tag{6.10}$$

avec, tel que défini au chapitre 5,

$$F_r = 4.482 \sigma r_b \left[(r_b/a)^{-2.324} - 1 \right] \tag{6.11}$$

On peut alors définir l'énergie cinétique (E_c) et l'énergie potentielle (E_p) comme :

$$E_c = \frac{1}{2} \rho_\ell V_b C_{Maa} \dot{a}^2 \tag{6.12}$$

$$E_p = \int_{r_b}^{a} F_r da = 4.482 \sigma r_b^2 \left[\frac{1}{3.324} \left(\frac{a}{r_b} \right)^{3.324} - \left(\frac{a}{r_b} \right) \right] \tag{6.13}$$

Le travail fait pas la force de jet s'exprime

$$W_{jet} = - \int_{r_b}^{a} \dot{a}^2 \rho_\ell V_b \left(\frac{d}{da} C_{Maa} \right) da \tag{6.14}$$

Les figures 6.9(a) et 6.9(b) présentent l'évolution énergétique du système de bulle oscillante pour deux relations de masse ajoutée. La figure 6.9(a) est un cas classique ou la masse ajoutée n'est pas variable en espace. Il n'y a donc pas de force de jet et la somme des énergies cinétique et potentielle est constante. La figure 6.9(b) est le cas de masse ajoutée variable avec $C_{Maa} = 0.2\chi^{1.17}$. Il devient évident que la somme des énergies cinétique et potentielle n'est pas constante. Le travail fait par la force de jet stabilise le bilan énergétique.

Les équations du mouvement peuvent également être obtenues à partir des équations de Lagrange. Or, un terme de force généralisée supplémentaire doit être ajouté pour prendre en compte la masse ajoutée variable (Pesce *et al.*, 2006). Dans le cas étudié ci-dessus, la bonne formulation des équations de Lagrange est :

$$\frac{\mathrm{d}}{\mathrm{d}t} \left(\frac{\partial}{\partial \dot{a}} \mathcal{L} \right) - \frac{\partial}{\partial a} \mathcal{L} = -\frac{1}{2} \rho_\ell V_b \left(\frac{\mathrm{d}}{\mathrm{d}a} C_{Maa} \right) \dot{a}^2 \tag{6.15}$$

avec la définition habituelle

$$\mathcal{L} = E_c - E_p \tag{6.16}$$

Il convient donc d'être particulièrement vigilant lorsque que l'on veut décrire de manière énergétique la dynamique d'un corps ;a masse variable en espace.

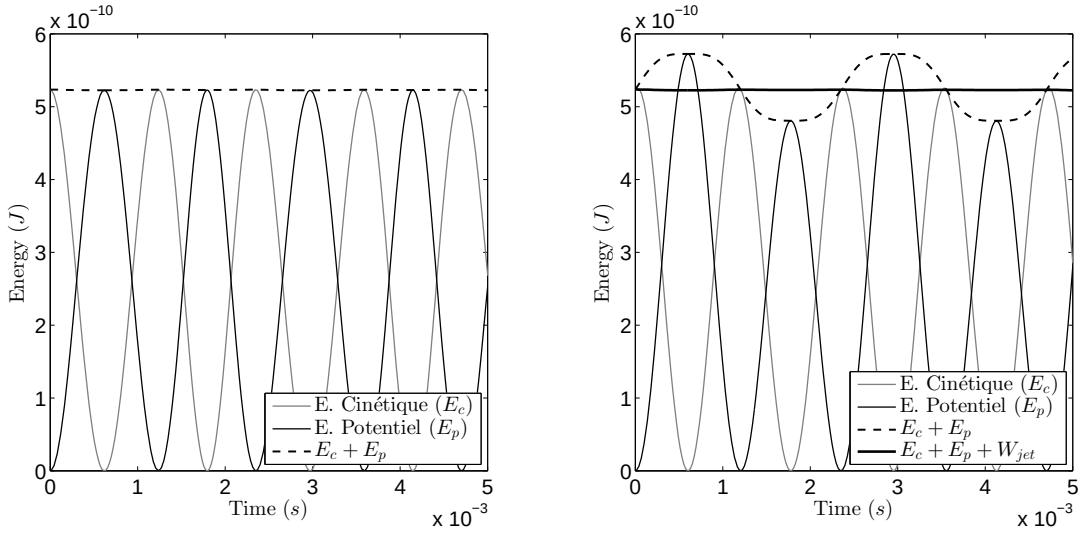

(a) $C_{Maa} = 0.2$ (b) $C_{Maa} = 0.2\chi^{1.17}$

Figure 6.9 Conservation de l'énergie pour une bulle oscillant en compression sans dissipation.

CHAPITRE 7

DISCUSSION GÉNÉRALE ET CONCLUSION

Le but de cette maîtrise était d'apporter des améliorations aux hypothèses du modèle développé par Senez et Étienne (2011). En ce sens, plusieurs nouveaux éléments sont apportés. Ce dernier chapitre regroupe l'essentiel des conclusions tirées précédemment.

7.1 Synthèse des travaux

Une approche a été développée pour résoudre l'écoulement autour d'un nuage de bulles sphériques de même dimension sous l'hypothèse d'un écoulement potentiel. À partir de cet écoulement, des expressions pour les forces de masse ajoutée ont été décrites sous deux formes : déterministe et statistique.

Dans sa forme déterministe, l'expression de la force de masse ajoutée permet de prendre en compte la géométrie exacte du nuage de bulles. On y voit trois composantes : la masse ajoutée en milieu infini, la correction due au confinement de chacune des autres bulles et les forces induites par l'accélération des autres bulles. Cette relation est utile pour les simulations Euler-Lagrange où les bulles sont suivies individuellement dans l'espace. Ce résultat est directement applicable au modèle de Senez et Étienne (2011). Cette expression est rapide à calculer et ne nécessite aucune résolution explicite de l'écoulement.

Ensuite, une étude expérimentale de collision de bulle sur un mur a été réalisée. Il a été montré que les bulles rapides et les bulles lentes peuvent présenter des tajectoires zig-zag et hélicoïdale. Également, peu importe leur trajectoire, l'élément clé pour décrire la dynamique des collisions des bulles est leur rapport d'aspect χ. Cette valeur est indicatrice que la quantité d'énergie qui pourra être redéployée dans un mouvement de rebond de la bulle. Ainsi, une bulle lente de forme sphérique aura un rebond très fortement amorti tandis qu'une bulle rapide aura un rebond vigoureux. Des relations décrivant l'état de rebond d'une bulle en fonction de ses caractéristiques d'approche sont données. Entre autres, il a été montré que des bulles lentes ont des coefficients de restitution d'environ 0.3 et les bulles rapides d'environ 0.7. Ces valeurs ainsi que les autres relations de restitution pourraient être intégrées à des simulations numériques traitant d'impact de bulle sur des structures.

Un modèle d'impact de bulle a également été créé afin de comparer avec les résultats des expériences. Dans ce modèle, les bulles sont considérées comme des ellipsoïdes de révolution partiellement déformables à volume constant et peuvent se déplacer en une seule dimension

spatiale. Les forces agissant sur la bulle ont été extraites et des régressions sont développées. Il n'est donc pas nécessaire de résoudre l'écoulement entier entre une bulle et un mur pour connaître les forces agissant sur la bulle. Bien que le modèle prédise adéquatement le coefficient de restitution, il ne peut rendre en compte toutes les subtilités observées dans les expériences. Nommons par exemple l'impossibilité du modèle de rendre compte de la forme *triangulaire* des bulles rapides lors du rebond.

L'approche utilisée dans le précédent modèle pour calculer les forces sur la bulle a également été étendue pour calculer les forces sur le mur. Il en résulte de la prédiction d'une force répulsive qui commence à agir à distance. Les calculs théoriques prédisent un effet à partir d'une distance bulle-mur d'environ 10 r_b. Un banc d'essais a été construit afin d'évaluer la force transmise lors d'un tel contact. Expérimentalement, ces forces à distance sont observées à partir d'une distance bulle-mur de 5 r_b. Bien que l'analyse quantitative n'a pu être approfondie, les premiers résultats suggèrent que les forces issues de l'écoulement potentiel pourraient être suffisantes pour prédire ces forces à distance. Ces relations pourraient également être appliquées au modèle numérique de Senez et Étienne (2011) afin de calculer les efforts sur les tubes.

Quelques observations supplémentaires ont également été faites durant cette maîtrise. Aucun éclatement de bulle n'a pu être observé suite à un contact avec une structure. Toutefois, deux autres mécanismes d'éclatement ont été identifiés : déchirement en vortex et éclatement par accélération subite. Le déchirement par vortex est un phénomène qui devrait probablement être intégré au modèle de Senez et Étienne (2011) car des zones de recirculation sont identifiées derrière les tubes et pourrait créer l'éclatement des bulles.

7.2 Améliorations futures

Beaucoup de pistes restent à être explorées, et ce, pour chacun des sujets étudiés. Dans le cas des forces de masse ajoutée à l'intérieur de nuage de bulles, la variation des dimensions des bulles pourrait être prise en compte. En effet, dans les écoulements réels, les bulles n'ont pas toutes les mêmes dimensions. La distribution est probablement fonction du taux de vide et devrait être mesurée.

Dans le contexte expérimental des collisions bulle-mur, la méthode d'injection de bulle d'air pourrait être améliorée en s'inspirant des travaux de Peters et Els (2012). Il serait ainsi possible de reproduire des impacts de bulles rapides et lentes sur une grande plage de diamètre de manière plus répétable. Également, il serait possible d'obtenir des trajectoires rectilinéaires permettant une étude plus approfondie des collisions avec un mur incliné ou bien une étude plus détaillée de la déformation des bulles lors de l'impact.

Cette étude de forme pourrait alimenter des améliorations au modèle théorique. En effet, il a été discuté que la forme ellipsoïdale au contact n'est peut-être pas optimale. Non seulement elle augmente artificiellement la raideur équivalente de la bulle, mais elle n'est pas représentative de la forme *triangulaire* de certaines bulles rapides. Davantage de mode pourraient être introduits afin de mieux décrire théoriquement la forme des bulles. Ces modes supplémentaires permettraient probablement une meilleure représentation dynamique des impacts.

Finalement, il serait également utile de pouvoir étendre le modèle théorique d'impact à des obstacles plus compliqués que des murs infinis. Ainsi, la force créée sur un flotteur pourrait être mieux prédite. Ce faisant, il faudrait également améliorer le dispositif de capture de force afin d'obtenir des résultats précis et répétables.

RÉFÉRENCES

BATCHELOR, G. (2010). *An introduction to fluid dynamics*. Cambridge University Press, New York, 14^e édition.

BIESHEUVEL, A. et SPOELSTRA, S. (1989). The added mass coefficient of a dispersion of spherical gas-bubbles in liquid. *International Journal of Multiphase Flow*, 15, 911–924.

BIESHEUVEL, A. et VAN WIJNGAARDEN, L. (1982). The motion of pairs of gas bubbles in a perfect liquid. *Journal of engineering Mathematics*, 16, 349–365.

BRENNEN, C. (2005). *Fundamentals of Multiphase Flow*. Cambridge University Press.

CAI, X. L. et WALLIS, G. B. (1994). A more general cell model for added-mass in 2-phase flow. *Chemical Engineering Science*, 49, 1631–1638.

CANOT, E., DAVOUST, L., EL HAMMOUMI, M. et LACHKAR, D. (2003). Numerical simulation of the buoyancy-driven bouncing of a 2-d bubble at a horizontal wall. *Theoretical and Computational Fluid Dynamics*, 17, 51–72.

CLIFT, ROLAND, G. J. R. et WEBER, M. E. (1978). *Bubbles, drops, and particles*. Academic press, New York.

DARMANA, D., DEEN, N., KUIPERS, J., HARTEVELD, W. et MUDDE, R. (2009). Numerical study of homogeneous bubbly flow : influence of the inlet conditions to the hydrodynamic behavior. *International Journal of Multiphase Flow*, 35, 1077–1099.

ELLINGSEN, K. et RISSO, F. (2001). On the rise of an ellipsoidal bubble in water : oscillatory paths and liquid-induced velocity. *Journal of Fluid Mechanics*, 440, 235–268.

GORMAN, D. (1976). Experimental development of design criteria to limit liquid cross-flow-induced vibration in nuclear reactor heat exchange equipment. *Nuclear Science and Engineering*, 61, 324–336.

ISHII, M. et HIBIKI, T. (2006). *Thermo-Fluid Dynamics*. Springer.

KENDOUSH, A., SULAYMON, A. et S.A.M, M. (2007). Experimental evaluation of the virtual mass of two solid spheres accelerating in fluids. *Experimental Thermal and Fluid Science*, 31, 813–823.

KLASEBOER, E., CHEVAILLIER, J.-P., MATÉ, A., MASBERNAT, O. et GOURDON, C. (2001). Model and experiments of a drop impinging on an immersed wall. *Physics of Fluids*, 13.

KOK, J. (1993a). Dynamics of a pair of gas bubbles moving through liquid. i : Theory. *European journal of mechanics. B, Fluids*, 12, 515–540.

KOK, J. (1993b). Dynamics of a pair of gas bubbles moving through liquid. i : Theory. *European journal of mechanics. B, Fluids*, 12, 515–540.

KUMARAN, V. et KOCH, D. (1993). The effect of hydrodynamic interactions on the average properties of a bidisperse suspension of high reynolds number, low weber number bubbles. *Physics of Fluids A : Fluid Dynamics*, 5, 1123.

KUSHCH, V. I., SANGANI, A. S., SPELT, P. D. et KOCH, D. L. (2002). Finite-weber-number motion of bubbles through a nearly inviscid liquid. *Journal of Fluid Mechanics*, 460, 241–280.

LAMB, H. (1932). Hydrodynamics. *Cambridge University, Cambridge*, 473.

LANCE, M. et BATAILLE, J. (1991). Turbulence in the liquid phase of a uniform bubbly air–water flow. *Journal of Fluid Mechanics*, 222, 95–118.

LEGENDRE, D., DANIEL, C. et GUIRAUD, P. (2005). Experimental study of a drop bouncing on a wall in a liquid. *Physics of Fluids*, 17, 97105.

LEGENDRE, D., MAGNAUDET, J. et MOUGIN, G. (2003). Hydrodynamic interactions between two spherical bubbles rising side by side in a viscous liquid. *Journal of Fluid Mechanics*, 497, 133–166.

LEGENDRE, D., ZENIT, R. et VELEZ-CORDERO, J. R. (2012). On the deformation of gas bubbles in liquids. *Physics of Fluids*, 24, –.

LEVICH, V. (1949). The motion of bubbles at high reynolds numbers. *Zh. Eksp. Teor. Fiz*, 19, 436.

MICHAELIDES, E. E. (2006). *Particles, bubbles & drops : their motion, heat and mass transfer*. World Scientific.

MILNE-THOMSON, L. (1968). *Theorical Hydrodynamics*. Macmillan, New York, 5^e édition.

MOKEYEV, G. (1977). Effect of particule concentration on their drag and induced mass. *Fluid Mechanics Sov. Res.*, 6, 161.

MOORE, D. (1959). The rise of a gas bubble in a viscous liquid. *Journal of Fluid Mechanics*, 6, 113–130.

MOORE, D. W. (1965). The velocity of rise of distorted gas bubbles in a liquid of small viscosity. *Journal of Fluid Mechanics*, 23, 749–766.

MORAGA, F.J., S. C. et R.T. LAHEY, J. (2005). Modeling wall induced forces on bubbles for inclined walls. *Multiphase Science and Technology*, 17, 483–505.

NIEMANN, J. et LAURIEN, E. (1991). Computing virtual mass by direct numerical simulation. *Journal of Pressure Vessel Technology*, 113, 233–253.

PELLETIER, E., BÉGUIN, C. et ÉTIENNE, S. (2014). Experiments air bubbles impacting a rigid wall in tap water. *Physics of fluid - Submitted*.

PERROT, E. (2011). *Forces d'excitation vibratoire dans un faisceau de tubes en configuration triangulaire normale soumis à un écoulement diphasique*. Mémoire de maîtrise, École Polytechnique de Montréal.

PESCE, C. P., TANNURI, E. A. et CASETTA, L. (2006). The lagrange equations for systems with mass varying explicitly with position : some applications to offshore engineering. *Journal of the Brazilian Society of Mechanical Sciences and Engineering*, 28, 496–504.

PETERS, F. et ELS, C. (2012). An experimental study on slow and fast bubbles in tap water. *Chemical Engineering Science*, 82, 194–199.

PODVIN, B., KHOJA, S., MORAGA, F. et ATTINGER, D. (2008). Model and experimental visualizations of the interaction of a bubble with an inclined wall. *Chemical Engineering Science*, 63, 1914 – 1928.

SANGANI, A. S. et DIDWANIA, A. (1993). Dynamic simulations of flows of bubbly liquids at large reynolds numbers. *Journal of Fluid Mechanics*, 250, 307–337.

SANGANI, A. S., ZHANG, D. et PROSPERETTI, A. (1991). The added mass, basset, and viscous drag coefficients in nondilute bubbly liquids undergoing small-amplitude oscillatory motion. *Physics of Fluids A : Fluid Dynamics*, 3, 2955–2970.

SENEZ, H. (2010). *Études des forces dues à la turbulence dans un écoulement diphasique transverse sur un faisceau de tubes en configuration triangulaire tournée*. Mémoire de maîtrise, École Polytechnique de Montréal.

SENEZ, H. et ÉTIENNE, S. (2011). Development of a numerical model to represet two-phase flow configurations in a tube bundle. A. P. V. . P. conference, éditeur, *ASME PVP2011*. vol. 4, 195–209.

SIMCIK, M., RUZICKA, M. et DRAHOS, J. (2008). Computing the added mass of dispersed particles. *Chemical Engineering Science*, 63, 4580–4595.

SMEREKA, P. (1993). On the motion of bubbles in a periodic box. *Journal of Fluid Mechanics*, 254, 79–112.

SOMMERS, B. et FOSTER, J. (2012). Nonlinear oscillations of gas bubbles submerged in water : implications for plasma breakdown. *Journal of Physics D : Applied Physics*, 45, 415203.

SPELT, P. et SANGANI, A. (1997). Properties and averaged equations for flows of bubbly liquids. *Applied scientific research*, 58, 337–386.

TAYLOR, T. et ACRIVOS, A. (1964). On the deformation and drag of a falling viscous drop at low reynolds number. *Journal of Fluid Mechanics*, 18, 466–476.

TOMIYAMA, A., CELATA, G., HOSOKAWA, S. et YOSHIDA, S. (2002). Terminal velocity of single bubbles in surface tension force dominant regime. *International Journal of Multiphase Flow*, 28, 1497 – 1519.

TOMIYAMA, A., MATSUOKA, T., FUKUDA, T. et SAKAGUCHI, T. (1995). Transverse migration of single bubbles in simple shear flows. *Advances in Multiphase Flow, Society of Petroleum Engineers, Inc*, 241–252.

TSAO, H. et KOCH, D. L. (1997). Observations of high reynolds number bubbles interacting with a rigid wall. *Physics of Fluids*, 9.

VAN GELDEREN, M. (1998). The shift operators and translations of spherical harmonics. *DEOS Progress Letter*, 1, 57–67.

VAN WIJNGAARDEN, L. (1976). Hydrodynamic interaction between gas bubbles in liquid. *Journal of Fluid Mechanics*, 77, 27–44.

VAN WIJNGAARDEN, L. (1991). *Bubble Deformation in Bubbly Liquid and Its Effect on the Stability of Voidage Waves*. Mathematical approaches in Hydrodynamics, SIAM, miloh t. édition.

VAN WIJNGAARDEN, L. et VELDHUIS, C. (2008). On hydrodynamical properties of ellipsoidal bubbles. *Acta mechanica*, 201, 37–46.

WALLIS, G. B. (1989). Inertial coupling in dispersed potential flow : macroscopic properties of suspensions in an inviscid fluid. *Multiphase Science Technology*, 5, 238–361.

WU, M. et GHARIB, M. (2002). Experimental studies on the shape and path of small air bubbles rising in clean water. *Physics of Fluids*, 14, L49.

ZENIT, R. et LEGENDRE, D. (2009). The coefficient of restitution for air bubbles colliding against solid walls in viscous liquids. *Physics of Fluids*, 21.

ZHANG, C. (2007). *Correlation between vibration excitation forces and the dynamic characteristics of two-phase flow in a rotated triangular tube bundle*. Thèse de doctorat, École Polytechnique de Montréal.

ZUBER, N. (1964). On the dispersed two-phase flow in the laminar flow regime. *Chemical Engineering Science*, 19, 897–903.

ZUBER, N. et HENCH, J. (1962). Steady-state and transcient void fraction of bubbling systems and their operating limits, part 1. steady state operation. *General Electric Report 62GL100*.